Quantifying the influence of climate change on the urban heat island of Hamburg using different downscaling methods

Dissertation
zur Erlangung des Doktorgrades der Naturwissenschaften im
Department Geowissenschaften der Universität Hamburg

vorgelegt von

Peter Hoffmann

aus

Jena

Hamburg

2012

Als Dissertation angenommen vom Fachbereich Geowissenschaften der Universität Hamburg

Auf Grund der Gutachten von Prof. Dr. K. Heinke Schlünzen
und Prof. Dr. Felix Ament

Hamburg, den 21.06.2012

Prof. Dr. Jürgen Oßenbrügge
Leiter des Fachbereichs Geowissenschaften

Abstract

In the present study, the influence of climate change on the urban heat island (UHI) of Hamburg is investigated. Two different methods to downscale regional climate projections with respect to the Hamburg's UHI are developed. First, a statistical model for the UHI of Hamburg is constructed using observations from the German Meteorological Service (Deutscher Wetterdienst (DWD)). This statistical model explains up to 42% of the UHI variance. By applying it to regional climate projections from REMO and CLM, which were driven with the A1B SRES emission scenario runs from ECHAM5/MPIOM, future changes in the UHI intensity are investigated. The results differ between both RCMs. Except for April and December (which show a decrease) REMO results show no significant changes to monthly average UHI intensity at the end of the 21st century, while analyses of CLM results show significant decreases from November through April and significant increases in July and August. The frequency distribution of the summer UHI shows no significant changes for REMO and in only one realization of CLM can a significant increase in moderate and strong UHI days be found for the end of the 21st century.

The second downscaling method is based on the concept of statistical-dynamical downscaling (SDD). As a part of the developed SDD method relevant weather situations for the UHI are determined. For this purpose an objective weather pattern classification (WPC) is constructed by applying a *k*-means based clustering technique to 700 hPa fields (geopotential height, relative humidity, relative vorticity, and thickness) from the ERA40 reanalysis dataset. Changes in the weather pattern (WP) frequencies in a future climate are obtained by applying different RCM results to the WPs. Both REMO and CLM show significant changes the WP-frequencies, especially by the end of the 21st century. Since the constructed WPC does not explain enough of the UHI variance to identify relevant days, it is combined with the statistical UHI model. The resulting relevant days are simulated with the mesoscale numerical model METRAS. In a two-step nesting a resolution of 1 km is reached, forced by ECMWF (European Center for Medium Range Weather Forecasts) analyses data. The UHI patterns obtained for each of the relevant days are then statistically recombined to compute the average pattern for days with a strong UHI (statistically modeled UHI $\geq$ 3 K). The statistically recombined UHI pattern for the present climate is quite well represented when compared with the available observations. The maximum UHI intensity of 1.2 K is found in the downtown and harbor area of Hamburg.

For the future UHI the SDD method is applied to results from A1B projections conducted with REMO and CLM as well as one A2 projection conducted with the high-resolution global model CCAM. Again, the results differ between the models. The pattern of the strong UHI remains unchanged for REMO while both CLM and CCAM show increases of approximately 0.13 K (some 10% of the simulated maximum UHI intensity) at the end of the century. The changes in CLM and CCAM are associated with a significant increase in strong UHI days.

Zusammenfassung

In dieser Arbeit wird der Einfluss des globalen Klimawandels auf die Hamburger Wärmeinsel (UHI) untersucht. Hierfür werden zwei Verfahren entwickelt, welche Klimaprognosen in Hinblick auf die Hamburger UHI verfeinern. Zuerst wird ein statistisches Modell für die Hamburger UHI erstellt, das auf Beobachtungsdaten des Deutschen Wetterdienstes (DWD) basiert und bis zu 42% der UHI-Varianz erklärt. Um die zukünftige Entwicklung der UHI zu untersuchen, wird das Modell auf regionale Klimaprognosen der regionalen Klimamodelle (RCM) REMO und CLM, welche beide von den ECHAM5/MPIOM Projektionen des A1B SRES Emissionsszenario angetrieben wurden, angewendet. Die Ergebnisse für die zukünftige UHI der beiden RCM unterscheiden sich. Außer für die Monate April und Dezember, die eine Abnahme der UHI zeigen, ändern sich die Monatsmittel der UHI nicht signifikant basierend auf REMO Ergebnissen. CLM Ergebnisse zeigen hingegen signifikante Abnahmen von November bis April sowie signifikante Zunahmen für Juli und August zum Ende des 21. Jahrhunderts. Die Verteilungsfunktion der täglichen UHI im Sommer weist keine signifikanten Änderungen in den REMO Ergebnissen auf. CLM zeigt eine signifikante Zunahme von Tagen mit moderater und starker UHI Ende des 21. Jahrhunderts zeigt.

Das zweite Verfeinerungsverfahren basiert auf dem Konzept der statistisch-dynamischen Verfeinerung (SDD). Der statistische Teil des SDD Verfahrens basiert auf der Bestimmung von Wettersituationen, welche für die UHI relevant sind. Hierfür wird eine objektive Wetterlagenklassifikation (WPC) erstellt. Die Wetterlagen werden mit Hilfe eines *k*-means-basierten Clusterungsverfahrens ermittelt. Als Eingabefelder für die WPC dienen 700 hPa Felder (geopotentielle Höhe, relative Feuchte, relative Vorticity und Schichtdicke) des ERA40 Reanalyse Datensatz. Um die zukünftigen Änderungen der Wetterlagen zu untersuchen, werden die Wetterlagen in den RCM Ergebnissen bestimmt. Die Häufigkeiten einzelner Wetterlagen ändern sich, vor allem Ende des 21. Jahrhunderts, sowohl für REMO als auch für CLM. Zur Bestimmung der für die UHI relevanten Tage erklärt die erstellte WPC einen zu geringen Teil der UHI Varianz. Aus diesem Grund wird die WPC mit dem statistischen UHI Modell kombiniert. In zwei Nestungsschritten werden die so erhaltenen relevanten Tage mit Hilfe des mesoskaligen numerischen Modells METRAS simuliert. Als Antriebsdaten dienen die Analysen des Europäischen Zentrums für mittelfristige Wettervorhersage (ECMWF). Für jeden simulierten Tag wird das UHI Muster bestimmt und anschließend mittels statistischer Rekombination gemittelt, um das mittlere Muster der starken UHI (statistisch modellierte UHI $\geq$ 3 K) zu berechnen. Verglichen mit

verfügbaren Beobachtungsdatensätzen wird das Muster der UHI basierend auf dem SDD Verfahren gut wiedergegeben. Die maximale UHI Intensität (ca. 1.2 K) befindet sich in der Innenstadt sowie in den Hafengebieten.

Um die zukünftige UHI zu untersuchen, wird das SDD Verfahren auf die A1B Projektionen von REMO und CLM sowie auf die A2 Projektionen des hochaufgelösten Globalmodells CCAM angewendet. Auch bei dieser Verfeinerungsmethode unterscheiden sich die Ergebnisse der verschiedenen Modelle. Das Muster der starken UHI bleibt unverändert, während die auf CLM und CCAM basierenden Ergebnisse für Ende des 21. Jahrhunderts eine Erhöhung von ca. 0.13 K in einigen Teilen Hamburgs zeigen (ca. 10% der simulierten maximalen UHI Intensität). In beiden Modellen ist diese Erhöhung verbunden mit einer signifikanten Zunahme von Tagen mit starker UHI.

Contents

1 Introduction

Cities influence both the global climate and the local climate. They are large emitters of greenhouse gases, which are largely responsible for recent global climate change (IPCC, 2007). Due to their modified surfaces, as well as energy emissions they also develop their own unique local climate (e.g. Oke, 1987). Although climate change and urban climate have been investigated quite extensively, relatively few studies examine the impact of climate change on urban climate. The impact of climate change on the urban heat island (UHI) is of particular interest. The UHI refers to the higher temperatures within urban areas compared to their rural surroundings (Arnfield, 2003). The magnitude of these temperature differences (up to 10 K; Yow, 2007) can be much larger than the expected temperature change due to climate change. Based on long-term observation for Prague (Beranova and Huth, 2005) and for London (Wilby et al., 2011) slight increases in UHI intensity were found, which were attributed to the changed climate. Changes in the maximum UHI intensity due to future climate change has been analyzed for London (Wilby, 2003; 2008) and New Jersey (Rosenzweig et al., 2005) using the output of global climate models (GCM). For London an increase for the UHI is expected, while the investigations for New Jersey indicate an unchanged UHI.

These studies focused on a single UHI measure. However, also changes in the structure of the UHI due to climate change could occur. Such changes are crucial to know planned climate change adaptation measures, as is done within the framework of KLIMZUG-NORD for Hamburg. For example, a temperature increase in certain parts of a city could be mitigated by planning adaptation measures (e.g. green roofs or parks) that reduce temperatures. To investigate the future UHI of a city like Hamburg future climate projections from GCMs as well as from regional climate models (RCM) are still too coarse to resolve such urban climate effects. The most detailed projections for Germany have been conducted with the RCM REMO and a resolution of 10 km (Jacob et al., 2008). Numerical studies on the UHI demonstrate that only high resolution simulations (at least 1 km) show model results that reproduce the UHI (e.g. Bohnenstengel et al., 2011; Wu et al., 2011; Grawe et al., 2012 submitted). Thus, regional climate projections have to be further downscaled. However, dynamical downscaling of the RCM results using high-resolution mesoscale numerical models is still too computationally expensive. Due to the low spatial coverage of high-quality observations within cities also statistical downscaling techniques (e.g. Wilby et al., 2009) are not feasible to downscale the UHI pattern. One downscaling method that reduces computational expense and still involves numerical simulations with a high-resolution model is the so-called statistical-dynamical downscaling (SDD) (Frey-Buness et al., 1995). Only relevant weather situations for the variable of interest are simulated with a high-resolution numerical model, which reduces the number of simulation days by a large factor. Afterwards, these results are statistically recombined to yield the climatological field of the variable. Früh et al. (2011a,b) developed a SDD method to investigate the urban heat load of Frankfurt am Main. Idealized situations that are varying in the initial temperature, relative humidity and wind speed are numerically simulated with a numerical model. Using a cuboid method the results of these simulations are statistically recombined. However, only two wind directions were considered. This might lead to an unrealistic UHI pattern because wind direction is important for the advection of the UHI (e.g. Gedzelman et al., 2003). In addition, the effect of cloud cover was neglected, which might lead to an overestimation of the simulated temperature differences.

The objective of this study is to investigate the influence of climate change on the UHI effect by developing and applying a more advanced statistical-dynamical downscaling technique to determine the UHI in the present and future climate. A weather pattern (WP) based selection of relevant UHI situations is combined with high-resolution simulations using the mesocale model METRAS (Schlünzen, 1990; Schlünzen et al., 2012a,b). The downscaling method is developed and assessed through analyzing the UHI of Hamburg, which was first investigated by Reidat (1971). The analysis of temperature observations within Hamburg, which were available for the period 1931-1960, revealed that at the downtown station Hamburg-St. Pauli temperatures were up to 1 K higher than at the airport station: Hamburg-Fuhlsbüttel. In light of current climate change, studies on the urban climate of Hamburg have been conducted in recent years. Hoffmann (2009) and Schlünzen et al. (2010) analyzed temperature and precipitation data to investigate the influence of Hamburg on both variables. Results showed that Hamburg develops an UHI and has an impact on the downwind precipitation. Annual averages of temperatures are up to 1 K higher in the city compared with the rural surroundings. Monthly average minimum temperatures are up to 3 K higher. Since only a few long-term observing stations are available within the urban area of Hamburg, Bechtel and Schmidt (2011) used floristic mapping data to construct a proxy dataset for temperature. Results show that temperatures are higher in downtown Hamburg (as well as in the harbor areas) than in the rural surroundings. Furthermore, remote sensing data are used to determine local climate zones (Bechtel and Daneke, 2011). These climate zones can be used to determine the UHI potential of certain parts of the city (Daneke et al., 2011).

A brief overview over existing downscaling techniques is given in Chapter 2. In Chapter 3 a statistical model for Hamburg's UHI is developed and applied to regional climate projections from two different RCMs in order to obtain a first guess about the future behavior of the UHI. Chapter 4 deals with a WPC specifically constructed for Hamburg's UHI to identify relevant weather situations for the UHI. The WPC is based on ERA40 reanalysis data and applied to RCM results to test the capability of RCMs to simulate the WPs and to see if changes in the WP frequency might influence the future UHI. The developed SDD method, which combines the methods given in Chapter 3 and 4 to downscale Hamburg's UHI, is described and applied in Chapter 5. In Chapter 6 the main findings are discussed and an outlook for future studies is given.

Chapter 3 has already been published in the International Journal of Climatology (Hoffmann et al., 2011). Chapter 4 has been submitted to the Journal of Applied Meteorology and Climatology (Hoffmann and Schlünzen, 2012). It is currently in review. Both publications are modified to be consistent with other parts of the thesis (e.g. coloring the figures, changing British English into American English).

2 Downscaling methods

The concept of downscaling can be described as the attempt to obtain high-resolution weather or climate information from either sparsely available observations or relatively coarse-resolution models (Rummukainen, 2010). Downscaling techniques can be subdivided into three main types: statistical (Section 2.1), dynamical (Section 2.2), and statistical-dynamical downscaling (Section 2.3). In the following they are briefly described. In addition, the requirements for the downscaling method to be developed in this study are given (Section 2.4).

2.1 Statistical downscaling

Statistical downscaling methods are based on the assumption that relationships exist between large-scale meteorological variables and smaller scale variables (Wilby et al., 2009). One of the simplest methods would be to modify GCM temperatures to the actual orography through height corrections. However, statistical models such as regression-based models are constructed, where observations of the small scale variable (predictand) are related to different large scale variables (predictor). Another approach is to use weather pattern-based (WP-based) downscaling methods, where the relationship between large-scale atmospheric patterns and local variables is exploited. For this approach it is assumed that large-scale patterns are well simulated by GCMs. For Germany the WP-based model WETTREG (Spekat et al., 2007) has been developed and applied to downscale climate projections from ECHAM5. Using simpler approach of resampling observed weather situations and prescribing only the temperature trend of the GCM, the statistical model STAR (Orlowsky et al., 2008) was also used to downscale ECHAM5 simulations for Germany. The third statistical downscaling approach is to downscale climate projections with help of a stochastic weather generator (e.g. Wilks, 1999).

Statistical downscaling has been applied to the downscaling of precipitation (Maraun et al., 2010), wind speed (e.g. Salameh et al., 2009; Curry et al., 2011; van der Kamp et al., 2011) and temperature (e.g. Spekat et al., 2007; Huth, 2002; Goyal et al., 2011). Furthermore, also derived variables such as the UHI (Wilby, 2003; 2008), air quality (Wilby, 2008) or biometeorological measures (Muthers et al., 2010) have been downscaled. The advantage of statistical downscaling is the reduced computing time. Therefore, it provides results quickly, and it is applicable to a large ensemble of climate change projections. However, a constant statistical relationship has to be assumed and high-quality long-term observations are needed (Wilby et al., 2009). The latter is a limiting factor, especially in urban climate studies. In addition, if more than one variable were statistically downscaled, the physical relationship would not always be preserved.

2.2 Dynamical downscaling

The concept of dynamical downscaling was first introduced in numerical weather prediction (e.g. Davies, 1976) and was later adapted to climate modeling (e.g. Dickinson et al., 1989; Giorgi, 1990). So-called local area models (LAM), which have a finer resolution than coarse global circulation (climate) models (GCM), are forced with the results from a coarser model. LAMs are able to simulate processes on a smaller horizontal scale than GCMs could, whereas GCMs can describe the global circulation adequately Several methods exist to transfer information from the coarser model to the finer one. In many studies the LAMs are forced at the lateral boundaries (e.g. Jacob et al., 2008; Hollweg et al., 2008; Giorgi et al., 2012) using the nudging technique introduced by Davies (1976). In addition, spectral nudging techniques are applied (e.g. Waldron et al., 1996; von Storch et al., 2000) to ensure that the larger-scale circulation in a high-resolution sub-domain does not differ substantially from the circulation of the coarser model results. Also, global models with a flexible grid are applied to weather forecasting (e.g. Coutier and Geleyn, 1988; Côté et al., 1998) and regional climate studies (Thatcher and McGregor, 2009). The latter are spectrally nudged within a GCM or only forced by the SST output of GCMs coupled with ocean models (Katzfey et al., 2009). To achieve high-resolution results, more nesting steps are needed (e.g. Jacob et al., 2008).

The great advantage of dynamical downscaling is the physical consistency of the downscaling results. Nevertheless, the computational effort to conduct long-term transient projections on a horizontal resolution of ~1 km, as it is needed for urban climate studies, is still too large. Knote et al. (2011) simulated two 10-year periods on a 1.3 km grid using the RCM CLM. However, for most climate applications at least a 30-year period is needed. Until such high-resolution long-term simulations are computationally affordable, the application of alternative methods is needed to investigate the future urban climate.

2.3 Statistical-dynamical downscaling

To combine the advantages of dynamical (physical consistency between meteorological variables) and statistical (reduced computing time) downscaling, a hybrid method was introduced the so-called statistical-dynamical downscaling (SDD) (Frey-Buness et al., 1995). Here it is assumed that characteristic weather patterns (WP) for small scale variables exist and that the climatology of these variables is mainly determined by the frequency of their respective WPs. These WPs can then be simulated by a high-resolution numerical model. The climatology of the small-scale variable is determined by the frequency of WPs. Some studies suggest that the changes within WP also have to be considered (Boé et al., 2006; Najac et al., 2011).

By simulating only a small number of situations with a high-resolution model, the computational effort is in an acceptable range. Within climate change studies SDD methods have been applied to downscale wind (Pinto et al., 2010; Najac et al., 2011), temperature (Fuentes and Heimann, 2000; Boé et al., 2006), precipitation (Boé et al., 2006; Huebener and Kerschgens, 2007a,b), and also ocean forcing (Cassou et al., 2011). Früh et al. (2011a,b) applied a simplified SDD method to downscale regional climate projections for the urban climate of Frankfurt am Main. They investigated the changes in urban heat load in Frankfurt am Main using idealized numerical simulations in combination with regional climate model results. This study showed that SDD methods are in general applicable for urban climate studies.

2.4 Requirements for a downscaling technique that can be used to determine UHI in present and future climate

Prior to the development of a SDD technique for the UHI, the specific requirements for the present study are stated that should be fulfilled by the method:

- The method should be applicable to results from different climate models and climate models of different resolution. The main reason is that climate change signals based on an ensemble of single climate models are believed to be more reliable than results from a single model. Uncertainties due to climate models deficiencies are reduced by using an ensemble of model results (e.g. van der Linden and Mitchell, 2009).
- The method needed should be applicable to observations, because the pattern of Hamburg's UHI is not well known even for the present climate.

- The final resolution of the results should be 1 km or less. Most of the recent numerical studies on the UHI (e.g. Bohnenstengel et al., 2011; Wu et al., 2011; Grawe et al., 2012 submitted) are conducted at this resolution. For higher resolutions the assumptions of Reynolds averaged models become more uncertain and large-eddy simulations might have to be conducted (Schlünzen et al., 2011).
- The computational effort should be as small as possible. The results from this study will be used for climate adaptation planning. Quantifying the impact of different adaptation measures on the urban climate might involve conducting the downscaling procedure several times with different adaptation measures included.

3 Statistical model for the urban heat island and its application to a climate change scenario

3.1 Preface

This Chapter has been published as: "Statistical model for the urban heat island and its application to a climate change scenario, Peter Hoffmann, Oliver Krueger, K. Heinke Schlünzen, *International Journal of Climatology*, doi: 10.1002/joc.2348. Copyright © 2011 the Royal Meteorological Society, first published by John & Wiley Sons Ltd." For the thesis the text has been modified to be consistent with other parts of the thesis (e.g. colored figures, American spelling) and by leaving out the Abstract and moving references to the end of the thesis.

3.2 Introduction

The changing climate due to greenhouse gas emissions (IPCC, 2007) leads to a need for adaption strategies especially for large cities. In addition, cities exhibit not only the impact of global and regional climate change but additionally create their own urban climate. They alter the properties of the atmospheric boundary layer including turbulence (e.g. Kastner-Klein and Rotach, 2004), temperature (Arnfield, 2003) and moisture field (e.g. Mayer et al., 2003; Kuttler et al., 2007; Liu et al., 2009). Furthermore, urban areas can impact precipitation patterns (e.g. Shepherd, 2005; Schlünzen et al., 2010). The most known phenomenon is the urban heat island (UHI) which refers to the higher air temperatures in urban areas compared to the surrounding rural areas (Oke, 1987). The main causes of the UHI are the higher heat capacity of urban surfaces, the trapping of radiation in street canyons, the reduced vertical exchange due to a reduced wind speed, and anthropogenic heat release (Yow, 2007). The UHI intensity varies with the morphology and the size of the city (Oke, 1973; Sakakibara and Matsui, 2005) and with meteorological conditions (Arnfield, 2003). It decreases with higher wind speeds, cloud cover and relative humidity (e.g. Morris et al., 2001; Kim and Baik, 2002; 2004; Schlünzen et al., 2010). The UHI does not only vary in space but also in time. Both a diurnal and an annual cycle were found for most of the cities. The strongest UHI intensity occurs 2 to 3 hours after sunset on a calm and cloudless day. In the morning hours even an urban cool island can develop (Oke, 1987). The annual cycle of the UHI depends on the climate zone the city is located.

Cities in moderate climate exhibit a maximum UHI in the warm season and a minimum UHI in winter (Arnfield, 2003).

The question we want to answer in this study is, whether a change of the meteorological variables due to climate change results in a change of the UHI of Hamburg. Schlünzen et al. (2010) have shown that Hamburg, situated in Northern Germany in a marine climate has indeed an UHI with monthly averaged urban-rural differences in minimum temperatures between 2.5 K and 2.9 K in the summer months. Thus before developing mitigation and adaption measures it should be known, if the UHI will change in a future climate. One way to determine the future UHI is to analyze temperature trends of rural and urban stations. Using this method Beranova and Huth (2005) found an increase in Prague's UHI. They linked this increase to more frequent unstable conditions due to higher temperatures near the ground that are caused by climate change. Rosenzweig et al. (2005) investigated changes in UHI for New Jersey. They analyzed wind speed and cloud cover for different global climate models (GCM) to have an estimate for the future UHI. They conclude that the UHI may remain unchanged since wind speed seems to decline and cloud cover seems to increase in the area of New Jersey. Londons UHI has been examined by Wilby (2003). He used a statistical model to identify trends in London's UHI and GCM data as input for the statistical model. He found that the nocturnal UHI intensity and the frequency of strong UHI events (> 4 K) would increase significantly in the future. In a more recent study Wilby (2008) used data from different GCMs driven with the SRES emission scenario A2. Both the UHI intensity and the frequency of strong UHI events increase in the 2050's between May and October. For the other months the changes are small. These results are not valid universally, as climate change differs regionally and so does the UHI. The development of regional climate models gives the opportunity to obtain more differentiated information about regional climate change. However, as current RCMs resolutions are still too coarse to simulate urban climate, results obtained have to be further downscaled. Dynamical downscaling cannot be applied here, as RCMs with a high resolution require large amounts of computing capacity. A method that demands less computing time and that has been applied successfully to urban climate before (Wilby, 2003; 2008) is statistical downscaling. It uses the relationship between certain large-scale variables and the variable of interest.

In this study a regression based statistical model for the UHI of Hamburg is constructed using meteorological observations. This model is then used to investigate the future UHI by applying it to the results of two realizations of the A1B SRES emission scenario (Nakicenovic et al., 2000) performed with the RCMs REMO and

CLM. The observational data and the UHI are described in Section 3.3.1. Section 3.3.2 deals with the ERA40 reanalysis data. A brief description of both RCMs is given in Section 3.3.3. The statistical model is described in Section 3.4. Results of the model using the RCMs as input are presented in Section 3.5. Concluding remarks are given in Section 3.6.

3.3 Data

To investigate both the present and the future UHI of Hamburg observations from the German Meteorological Service (DWD), ERA40 and results from RCMs are used.

3.3.1 Observations

One problem that needs to be tackled when investigating the urban climate of Hamburg is the absence of a dense long-term station network inside the city. For that reason, only data from 1985 to 1999 are analyzed. For this period data from six climate stations and one synoptic station operated by the DWD are available. The locations of the stations are given in Figure 3.1. Climate stations provide daily values for temperature, precipitation and cloud cover. Data from station Hamburg-Fuhlsbüttel (FU) at the Hamburg Airport, which is both a synoptic station and a climate station, contain hourly values for temperature, pressure, precipitation, wind speed and direction, cloud cover, and humidity (specific and relative). The only station located downtown is Hamburg-St. Pauli (SP). It is surrounded by medium sized buildings (up to 6 stories). The station is located a few hundred meters from the river Elbe. The population density of the district is about 10700 inhabitants per square kilometer. SP serves in the following as the urban reference station for the calculation of the UHI.

The two available rural stations are Grambek (GR) and Ahrensburg-Wulsdorf (AH). Station GR is located next to a small village with about 400 inhabitants. Station AH is located next to the political border of the state of Hamburg and is surrounded by grain fields. Instead of using data from only one rural reference station (GR) as in Hoffmann et al. (2009) and Schlünzen et al. (2010) both GR and AH are included in the calculation making the results more robust. Hamburg’s UHI is then defined as:

$$\Delta T_{u-r} = T_{\min,SP} - \frac{(T_{\min,GR} + T_{\min,AH})}{2} \qquad (3.1)$$

$T_{\min,SP}$, $T_{\min,GR}$ and $T_{\min,AH}$ are the daily minimum temperatures at the station SP, GR and AH respectively. Using this formula an average ΔT_{u-r} of 2 K can be found for Hamburg which is about 0.3 K smaller than Hoffmann et al. (2009) got with only GR as reference station.

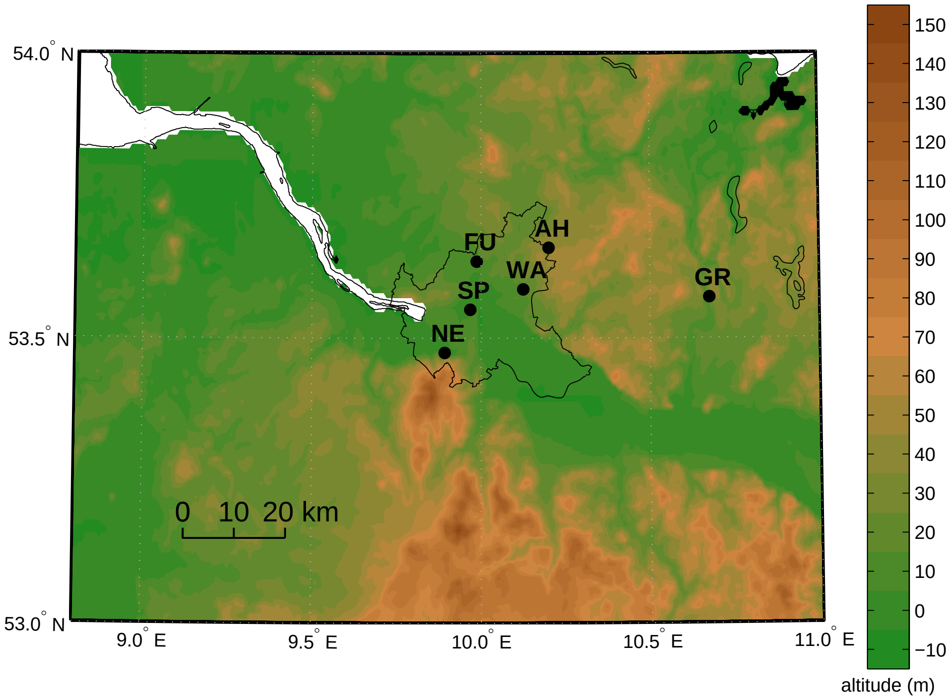

Figure 3.1: *Map of the metropolitan area of Hamburg with positions of the measurement sites and political borders of Hamburg. Sites are AH (Ahrensburg-Wulsdorf), FU (Hamburg-Fuhlsbüttel), GR (Grambek), NE (Hamburg-Neuwiedenthal), SP (Hamburg-St. Pauli) and WA (Hamburg-Wandsbek).*

The annual cycle of ΔT_{u-r} is given in Figure 3.2. As found by Schlünzen et al. (2010) a clear maximum in the warm season with average monthly values up to 2.7 K is visible. Only the magnitude of the monthly averaged ΔT_{u-r} are slightly lower. This can be explained by the higher minimum temperatures at AH compared to GR. As can be expected ΔT_{u-r} is also highly variable which is illustrated by the 25th and 75th percentile. The values range from a minimum of -4 K to a maximum of 10.5 K. The 75th percentile shows typical summer UHI values between 3.5 K and 4 K.

The meteorological variables that are needed to derive the statistical model are taken from the station FU except cloud cover. For this variable two additional stations are available, Hamburg-Neuwiedenthal (NE) and Hamburg-Wandsbek (WA). Cloud cover is averaged over all stations. To get daily values of wind speed the hourly measurements at FU are averaged daily.

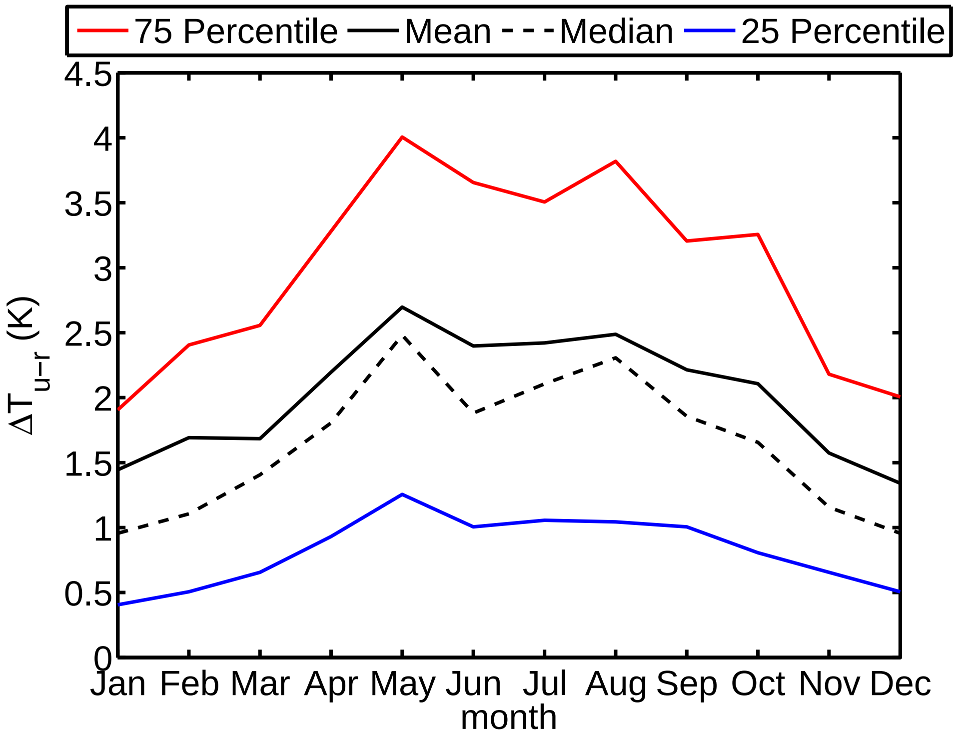

Figure 3.2: *Annual cycle of different statistics of UHI for the period 1985-1999.*

3.3.2 ERA40 reanalysis

Continuous meteorological observations are not available for several decades for the region of Hamburg especially for wind speed. For climate analysis, at least a 30 year period has to be considered. To overcome the drawback of the temporal constraint the ERA40 reanalysis dataset produced at the European Centre for Medium-Range Weather Forecasts (ECMWF) (Uppala et al., 2005) is used as well. With the help of the data assimilation system and the global forecast model a best possible estimate of the past atmospheric state was constructed. The gridded dataset starts in September 1957 and ends in August 2002. The horizontal resolution of the dataset is 1.125° (~125 km). Due to the coarse resolution only data of one grid box closest to Hamburg is used (Figure 3.3). As input for the statistical model the variables 10 m wind speed, 2 m relative humidity and the total cloud cover are used. Relative humidity is derived diagnostically with the Magnus-formula (Hupfer and Kuttler, 2006). Cloud cover is converted into octas. All variables were available every 6 hours and are therefore daily averaged to correspond to the observations by the DWD.

Due to the way they are obtained observations and reanalysis data differ. The DWD observations are from point measurements while reanalysis data, as described above, are the result of an assimilation process involving a numerical model with a coarse resolution using information from more than just one observational data source. Thus, they are representative on different spatial scales. Comparing the ERA40 data with DWD observations in the period from 1985 to 1999 the mean and the standard deviation of the corresponding variables differ slightly. The correlation is low only for cloud cover (r = 0.74). For wind speed (r = 0.88) and relative humidity (r = 0.92) both datasets correlate well.

3.3.3 Regional climate models

The future UHI is analyzed with the help of results from the RCMs REgional MOdel (REMO, Jacob and Podzun, 1997; Jacob, 2001; Semmler et al., 2005) and Climate Local Model (CLM, Steppeler et al., 2003; Böhm et al., 2006) that are used to drive the statistical model. Both models are driven with the coupled global climate model ECHAM5/MPIOM (Roeckner et al., 2003, Jungclaus et al., 2006), which was developed at the Max-Planck-Institute for Meteorology (MPI-M) in Hamburg. In the present study results from the first two SRES A1B emission scenario runs are used. The assumption of this scenario is a rapid growth of global population, economy, and CO_2 emissions with a peak in CO_2 emissions in the middle of the century and a decline afterwards. It additionally assumes a balanced use of technologies for the energy supply. Short description of the RCMs and the used data is given in Section 3.3.3.1 and 3.3.3.2 respectively.

An evaluation of results of the two RCMs for present climate is not made in this study. More specifically the meteorological variables of REMO and CLM are not bias corrected. A bias correction is beyond the scope of this study and needs to be done elsewhere. Therefore, only the relative changes of the modeled ΔT_{u-r} will be considered in the analyses.

3.3.3.1 REMO

REMO is a hydrostatic numerical model based on the Europa-Modell (EM; Majewski, 1991) from DWD. It was developed at the Max-Planck-Institute for

Meteorology in Hamburg. The physical parameterizations were taken from the GCM ECHAM4 (Roeckner et al., 1996). An extended description is given in Jacob (2001) and Jacob et al. (2001). REMO solves the prognostic equations for temperature, *u* and *v* component of the wind, surface pressure, mixing ratio of water vapor and of cloud water. The model runs for Germany are produced in two nesting steps (Jacob et al., 2008). A coarse version of REMO is forced by ECHAM5 output at the lateral boundaries. This version covers the European continent in a resolution of 0.44° (~50 km). A version with a finer resolution of 0.088° (~10 km) covering Germany and parts of Switzerland and Austria is nudged within the results of the first step. The horizontal grid used for both runs is a regular grid with a rotated pole.

Since relative humidity is not available as an output variable it is diagnostically derived using the Magnus-formula (Hupfer and Kuttler, 2006). Cloud cover is converted from area fraction into octas to make them comparable to the observations. In addition, the diagnostic 10 m wind speed is used. Climate change signals from numerical models are not representative grid-point-wise. Only results averaged over at least 9 grid points should be analyzed. The locations of the grid points used for the averaging procedure are given in Figure 3.3a. Wind speed and relative humidity are averaged over the 9 grid boxes indicated by the grey boxes. In addition to the grey boxes the surrounding black grid boxes are used for averaging cloud cover since the cloud cover observations are averages over a larger area.

3.3.3.2 CLM

In contrast to REMO, CLM is a non-hydrostatic numerical model. It is the climate version of the Lokal-Modell (LM) from the DWD. A short model description is given by Böhm et al. (2006). The dynamics and physics of the model are described in detail by Steppeler et al. (2003). CLM solves the prognostic equations for temperature, horizontal and vertical wind components, pressure perturbations, specific humidity and cloud water content. Hollweg et al. (2008) describe the model runs for the IPCC scenarios in detail. The model version used for these runs is CLM 2.4.11, with a resolution of 0.165° (~18 km) on a rotated grid. The model is directly nudged within ECHAM5 and covers Europe.

For the statistical analyses the results from REMO the variables are averaged over several grid boxes. Figure 3.3b shows the location of these grid boxes. Because of the lower resolution of CLM the 9 grid boxes cover Hamburg completely. Thus, all variables are averaged over the same grid boxes.

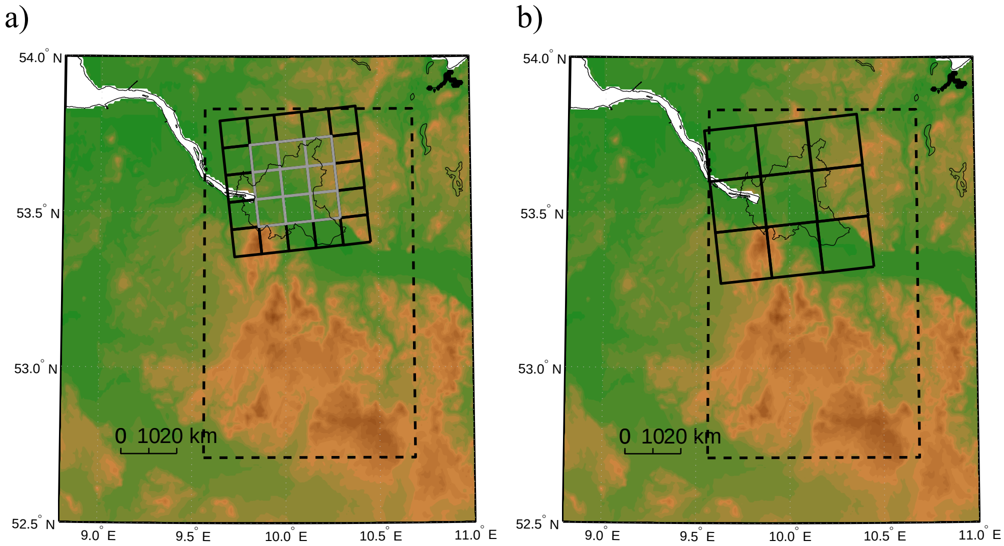

Figure 3.3: *(a) Grid boxes from REMO used for the statistical model. Wind speed and relative humidity are taken from boxes with thick lines. (b) Grid boxes from CLM used for the statistical model. All variables are taken from these grid boxes. The box with dashed lines indicates the ERA40 grid box used in this study.*

3.4 Statistical model

In this study a regression based statistical model similar to those from Wilby et al. (2002) is constructed. The predictand is the UHI intensity ΔT_{u-r} (Eq. 3.2). To find appropriate predictors a simple linear regression between UHI and the meteorological variables X is computed (Eq. 3.2). The statistical significance of the regression is calculated by means of a two-sided t-test. In addition, the explained variance R^2 is calculated to estimate the strength of the relationship.

$$\Delta T_{u-r} = aX + b \tag{3.2}$$

To develop the statistical model five variables were chosen based on early findings and physical relevance. Wind speed has been shown to be considerably influence the UHI with large wind speeds reducing the UHI (e.g. Schlünzen et al., 2010). Cloud cover was found to have a similar impact with higher cloud cover reducing the UHI (e.g. Morris et al., 2001; Kim and Baik, 2002; 2004). Relative humidity seems to have also an impact on the UHI as it was found by Kim and Baik (2002; 2004). To have another measure for humidity water vapor pressure is chosen. The UHI is found to be well developed under anticyclonic conditions (e.g. Tumanov et al., 1999; Morris and Simmonds, 2000; Bejaran and Camilloni, 2003). To take this into account air pressure is selected as a potential model variable as well (Moreno-Gracia, 1994). Figure 3.4 shows the scatterplots of ΔT_{u-r} for the different variables, and Table 3.1 the corresponding results from the linear regression. All regressions, except for water vapor pressure, are significant ($\alpha = 0.05$). The strongest relationship exists between ΔT_{u-r} and cloud cover from the previous day ($R^2 = 24.4\%$). Clouds absorb and emit longwave radiation, which reduces diurnal temperature variation (Oke, 1987). In addition, they reduce the incoming shortwave radiation and therefore the amount of heat stored in urban materials (Hupfer and Kuttler, 2006; Kawai and Kanda, 2010). The letter explains the stronger relationship to the previous day observations than to the corresponding day (not shown). The strength of the relationship to wind speed and to relative humidity is lower. The explained variance of both is almost identical ($R^2 = 17.1\%$).

The negative correlation between ΔT_{u-r} and wind speed can be explained by the increase of the temperature advection with higher wind speeds (e.g. Morris et al., 2001). Schlünzen et al. (2010) found that the dependency of the Hamburg UHI on wind speed is best described by the inverse square root. However, the differences of the explained variance between the different functions were small in their study. In addition, they used the difference between the daily mean temperatures at FU and GR, while we use SP and an average rural temperature. The regression based on the inverse square root or on the power function reveals for the relationship between ΔT_{u-r} and wind speed smaller R^2 (not shown). Thus, in the present analysis the linear regression seems to fit best.

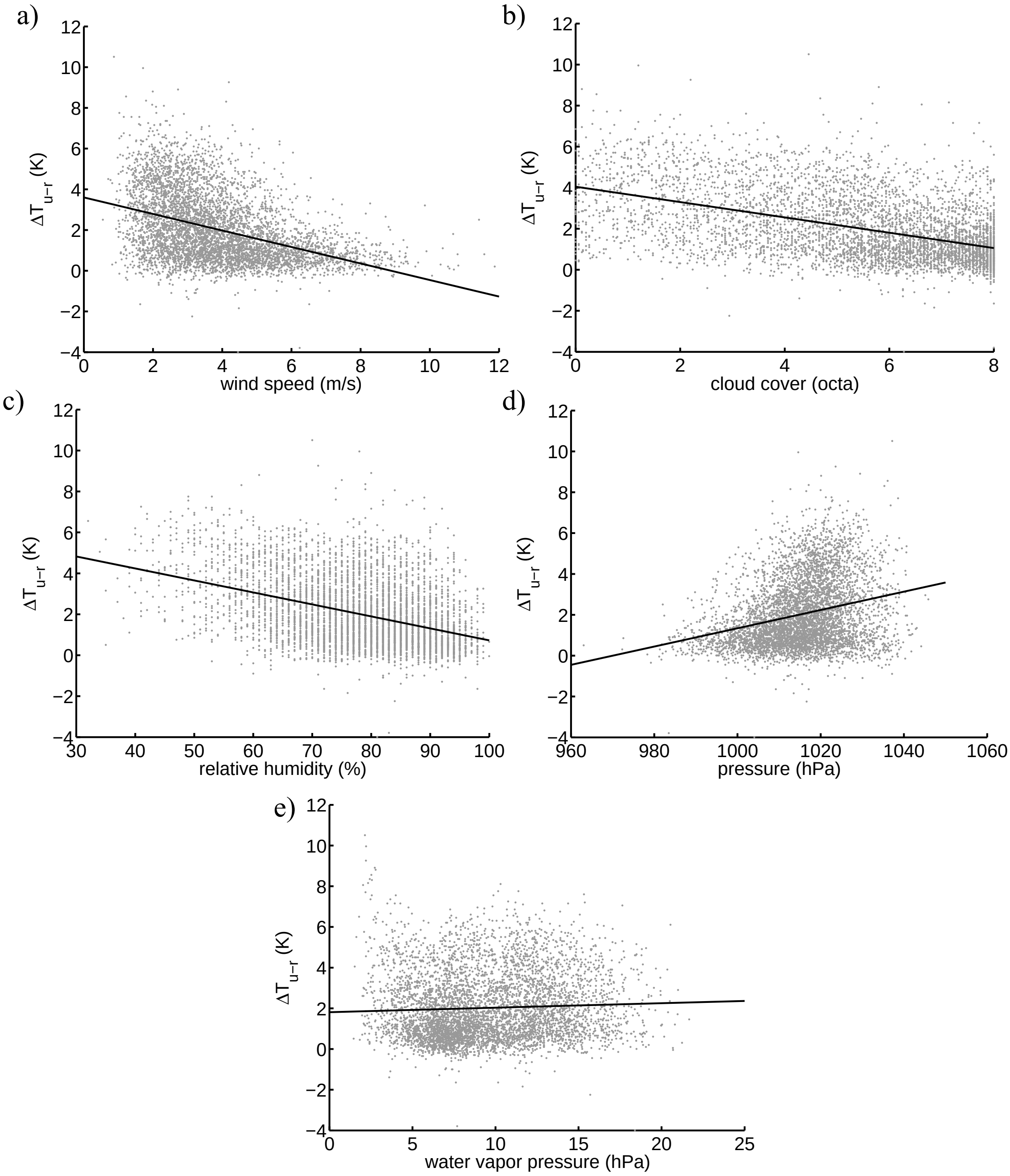

Figure 3.4: *Scatter diagrams of UHI and (a) daily mean wind speeds at FU, (b) area averaged daily mean cloud cover from previous day, (c) daily mean relative humidity at FU, (d) daily mean surface pressure at FU, (e) daily mean water vapor pressure at FU. Data for 1985-1999. Lines indicate the linear regression (parameters see Table 3.1).*

An explanation for the negative correlation between ΔT_{u-r} and relative humidity could be the release of latent heat due to condensation. The higher the relative humidity the more probable the air reaches saturation. The heat released by condensation warms the air. As rural surfaces tend to cool faster at night than urban surfaces the condensation process starts earlier in rural areas. The result is a reduced urban-rural temperature difference results. High values of relative humidity can also lead to the development of nocturnal fog that reduces the radiative loss directly at the ground. Air pressure only explains 7.6% of the ΔT_{u-r} -variance and is thus less relevant for UHI development. The same is true for water vapor pressure (R^2 = 0.2 %).

Table 3.1: *Results from the linear regression between UHI (K) and different meteorological variables for period 1985 to 1999 using Eq. (3.2).*

Variable	***a***	***b***	***R²***
wind speed (m/s)	-0.41	3.6	17.1
cloud cover of previous day (octa)	-0.37	4	24.4
relative humidity (%)	-0.058	6.58	17.1
air pressure (hPa)	-0.045	-43.46	7.6
water vapor pressure (hPa)	0.022	1.81	0.2

The results of the linear regression show that the variables wind speed *FF*, cloud cover *CC*, and relative humidity *RH* should be used for the linear model (Eq. 3.3).

$$\Delta T_{u-r} = a\,FF + b\,CC + c\,RH + d \tag{3.3}$$

The residuals of the model computed with the method of ordinary least squares (OLS) are significantly ($\alpha = 0.05$) autocorrelated. Autocorrelated residuals tend to influence the parameter estimation, which can be avoided by making use of the generalized least squares (GLS) method (Cochrane, 1949). In our case the residuals are modeled through an AR(1) process. Furthermore, robust model results are obtained by repeatedly (150 times) deriving the model leaving out 500 consecutive observations each time (Krueger and von Storch, 2011). The final model parameters are given in Table 3.2. The explained variance of the model is $R^2 = 42\%$ which is slightly higher than the model by Wilby (2008).

The unexplained variance is modeled by adding an extra term ε to Eq. (3.3) as it was also done by Wilby et al. (2002). ε however, is computed by resampling the model residuals (1000 times) instead of fitting a theoretical probability distribution function to the residuals. This avoids the problem of determining the appropriate distribution function. The resampling is done with a pseudo random number generator. The final model equation is then:

$$\Delta T_{u-r} = a\,FF + b\,CC + c\,RH + d + \varepsilon \tag{3.4}$$

The frequency distributions of the modeled and observed ΔT_{u-r} are given in Figure 3.5. Both distributions are similar to the distributions of London's UHI found by Wilby (2003). The observed distribution shown in Figure 3.5 seems to be typical for a city in a moderate climate. The similarities of the modeled observation based UHI can be partially explained by similar methods and variables used to derive and to apply the statistical model. The skewed distribution of ΔT_{u-r} is not captured by the statistical model. The modeled distribution is close to a normal distribution and cannot simulate the peak at around 0.5 K. It overestimates ΔT_{u-r} values below -0.5 K as well as between 2.5 K and 3.5 K. A good agreement can be found for ΔT_{u-r} around 4 K and above 6 K.

Table 3.2: *Model parameters for Eq. (3.3) and Eq. (3.4) computed with GLS method. The mean and the 95% confidence interval are determined from an ensemble of derived parameters (for details see text).*

Parameter	Mean	2.5 Percentile	97.5 Percentile
a (K/m²)	-0.354	-0.360	-0.346
b (K/octa)	-0.185	-0.193	-0.179
c (K/%)	-0.039	-0.038	-0.041
d (K)	7.73	7.63	7.84

Figure 3.5 also shows the distribution of the model ΔT_{u-r} with ERA40 data as input. It reveals that the shape stays nearly the same as when directly using observations but the whole distribution is shifted towards lower ΔT_{u-r}. The prime reason for this result is the higher wind speeds in ERA40 data compared to the observations at FU. Comparing the monthly means of both modeled and observed ΔT_{u-r} reveals that the annual cycle can be simulated quite well (Figure 3.6), primarily the summer months. In October ΔT_{u-r} is underestimated by about 0.2 K based on the observations in comparison to the observed UHI. Using the ERA40 data in the statistical model gives smaller values then the model driven with observations. For March to August the range of the statistically modeled UHI is close to the observed one. A larger underestimation is found from September to February. Since UHI is most relevant for the summer months this is not a severe drawback of our analyses.

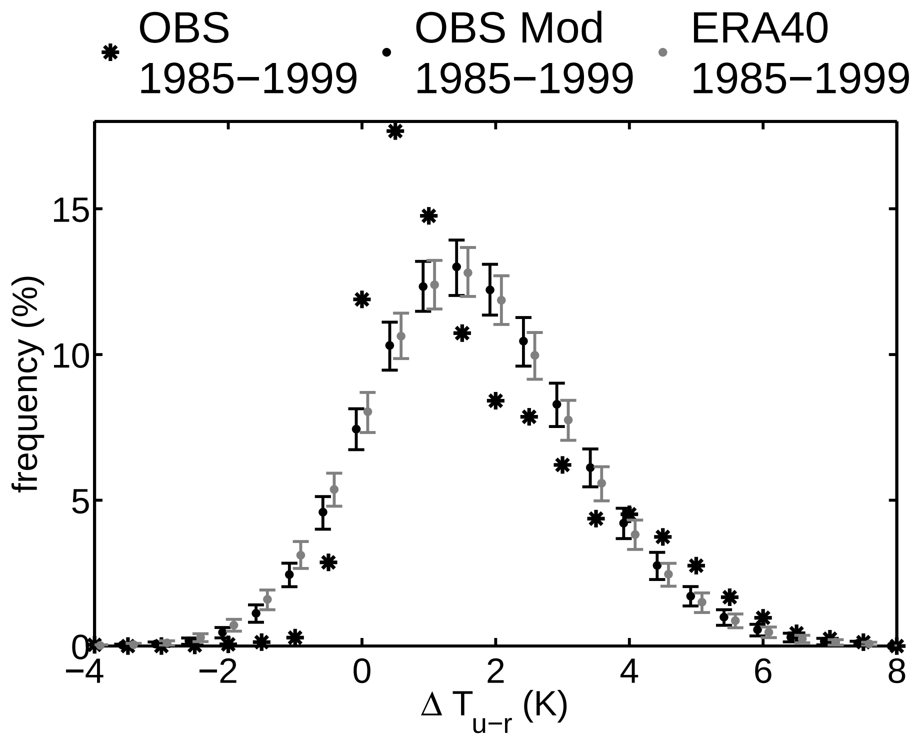

Figure 3.5: *Frequency distribution of observed (black asterisks) and modeled (points with error bars) UHI intensity using measurements (black) and ERA40 (grey) data for the period 1985-1999. Error bars indicate the 95% confidence intervals due to unexplained variance.*

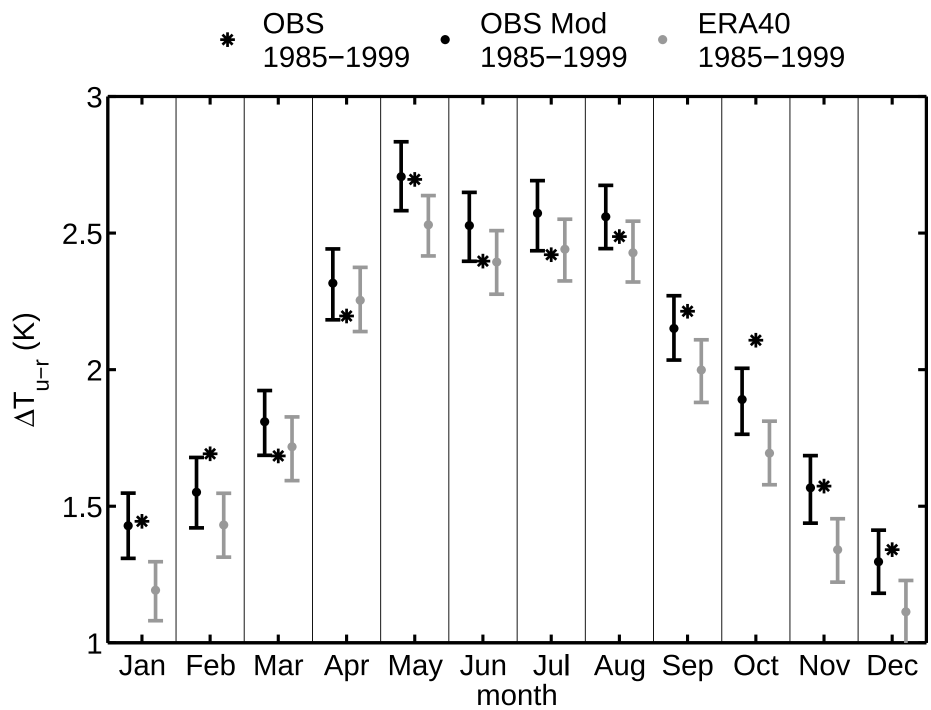

Figure 3.6: *Annual cycle of observed (black asterisks) and modeled (points with error bars) UHI intensity using measurements and ERA40 data for the period 1985-1999. Error bars indicate the 95% confidence intervals due to unexplained variance.*

3.5 Urban heat island in the future climate

To determine changes of the statistically modeled UHI for the 30-year periods 2036-2065 and 2071-2100, UHI results are compared with the results for the control period 1971-2000. We assume that the statistical relationship between predictand and predictor derived from the observed data in period 1985-1999 holds for the present climate control period (1971-2000) and does not change in the future climate. This assumption might not be valid because Hamburg will change in size, energy consumption, and other characteristics in the future that affect the UHI. However, the focus of this study is to analyze the possible change of the UHI due to a change in meteorological conditions.

Table 3.3 shows the averaged modeled ΔT_{u-r} for the different periods. The results for the control period (1971-2000) show a strong underestimation of ΔT_{u-r} when CLM is used as input. The mean ΔT_{u-r} with REMO-input is very close to the results with ERA40-input and slightly smaller than the results with observations as input. The underestimation of CLM is caused by an overestimation of the relative humidity and cloud cover, which was also found in other studies (Hollweg et al., 2008; Jaeger et al., 2008). Wind speeds that are higher compared to the observed values are the reason for the underestimation of the UHI with REMO and ERA40 results (not shown). The wind speed overestimation was also found by Walter et al. (2006) for REMO and Barstad et al. (2009) for ERA40 for other regions.

Table 3.3: *Averaged modeled UHI intensities in Kelvin for different periods.*

	OBS Mod	ERA40	CLM 1	CLM 2	REMO 1	REMO 2
1971-2000	2.02 (1985-1999)	1.87	1.27	1.31	1.92	1.90
2036-2065	-	-	1.24	1.22	1.89	1.90
2071-2100	-	-	1.23	1.22	1.89	1.87

For both RCMs the changes of the mean of ΔT_{u-r} between the three periods are less than 0.1 K, which is smaller than the accuracy of the data. The reason for the small changes is that the means of all three variables used for the statistical model do not differ substantially between the periods. This indicates that the current annual mean UHI will not change due to changes in meteorological conditions.

Figure 3.7 shows the annual cycle of the modeled ΔT_{u-r} for the control period and the scenarios for both RCMs and the two realizations. The annual cycle simulated with REMO is weaker and slightly shifted compared to the ERA40 annual cycle (Figure 3.7a). The values for October to December are overestimated. However, it should be kept in mind that for the 15 years (1985-1999) period the ERA40 driven model gave lower values for these months compared to the observations (Figure 3.6). The lower values in February, May and the summer months cannot be addressed to the deficits of ERA40 but are due to higher wind speeds in REMO. Regarding the scenarios only the April changes are significant for both the realizations and both the periods. The magnitude of the decrease varies from 0.1 K to 0.2 K between the realizations for the period 2036-2065. For the period 2071-2100 both realizations show a decrease of about 0.2 K. The other month that shows a clear signal in both realizations is December with a significant decrease of 0.1 K for the last period. However, this change is again close to the accuracy of the data. All the other months show either no significant change or only significant changes in one realization. These findings show again, that the meteorological conditions which are important for Hamburg’s UHI do not differ much in the scenario simulations of REMO.

The large underestimation of ΔT_{u-r} simulated with CLM is obvious in the annual cycle (Figure 3.7b). All the monthly means are underestimated and the magnitude of the cycle is smaller. Different from the REMO results, the means change significantly for the majority of the months. May is the only month with no significant changes. September show an increase in the first realization and a decrease in the second one for the end of the century. Hence, no conclusion can be drawn for this month. A significant increase can be found for July and August, which ranges from 0.1 K to 0.4 K and is different for different realizations. In the rest of the year (November-April) changes of ΔT_{u-r} are negative. The strongest decrease for the first future period with about 0.2 K in both realizations occurs in March. In the second period all winter months, March, and April show strong decreases ranging between 0.2 K and 0.3 K. Together with the increase in July and August the amplitude of the annual cycle of ΔT_{u-r} modeled with CLM increases.

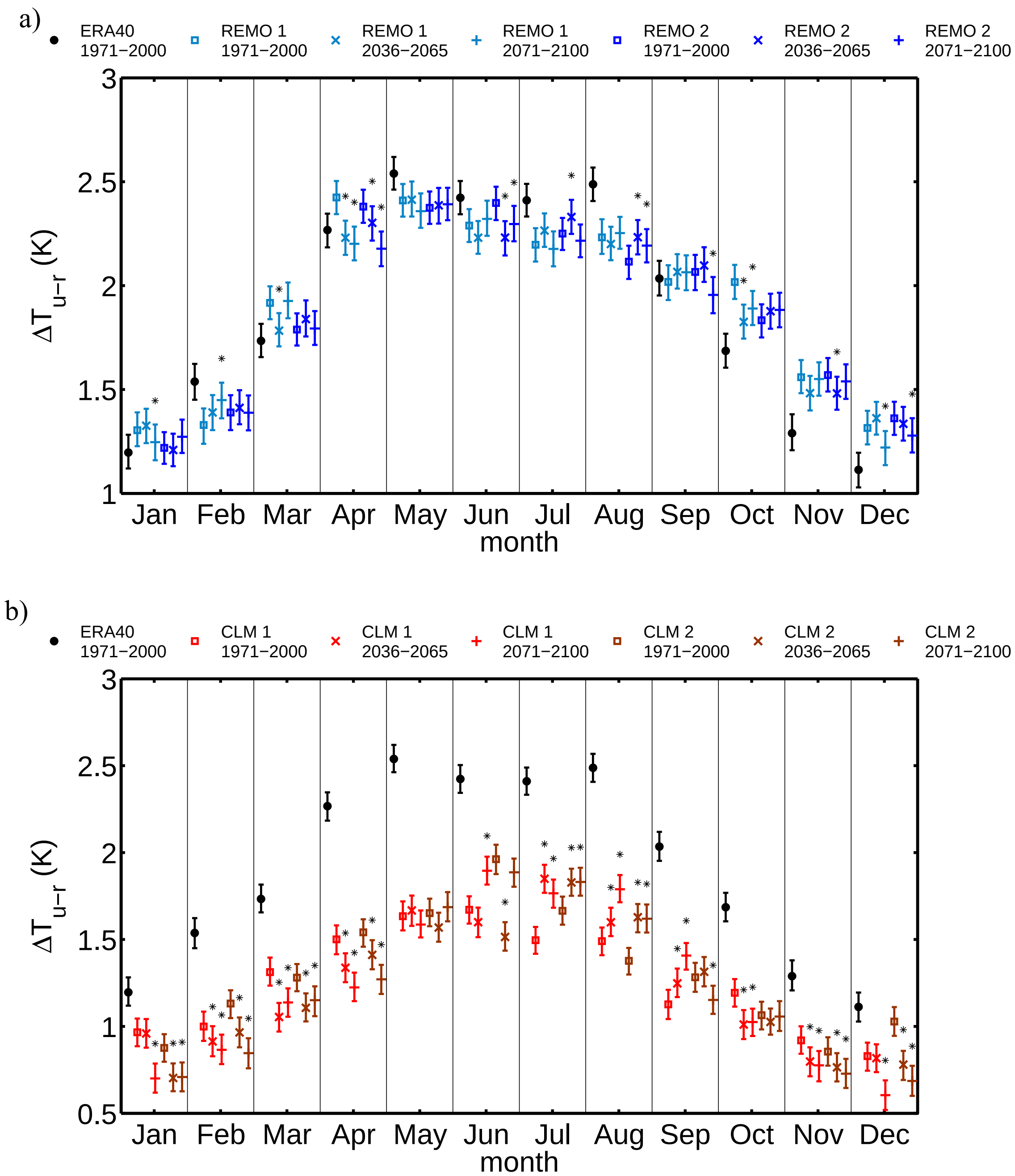

Figure 3.7: *Annual cycle of the modeled UHI intensity using ERA40 data and two realizations of (a) REMO and (b) CLM for different time periods. Error bars indicate the 95th confidence intervals due to the unexplained variance. The black asterisks mark significant (α = 0.05) changes between the corresponding period and the control period (1971-2000).*

To investigate changes in the frequency of certain modeled UHI events in the summer months July to August the results are grouped into four intensity classes. The first class represents days with a negative UHI (< 0 K), the second days with a weak UHI (0-2 K), the third days with a moderate UHI (2-4 K) and the fourth days with strong UHI (> 4 K). Figure 3.8a reveals that only the frequency of negative UHI days is well captured using REMO as input. Weak UHI occur too often while moderate and strong UHI days are underrepresented. In the future no changes in the distribution can be found.

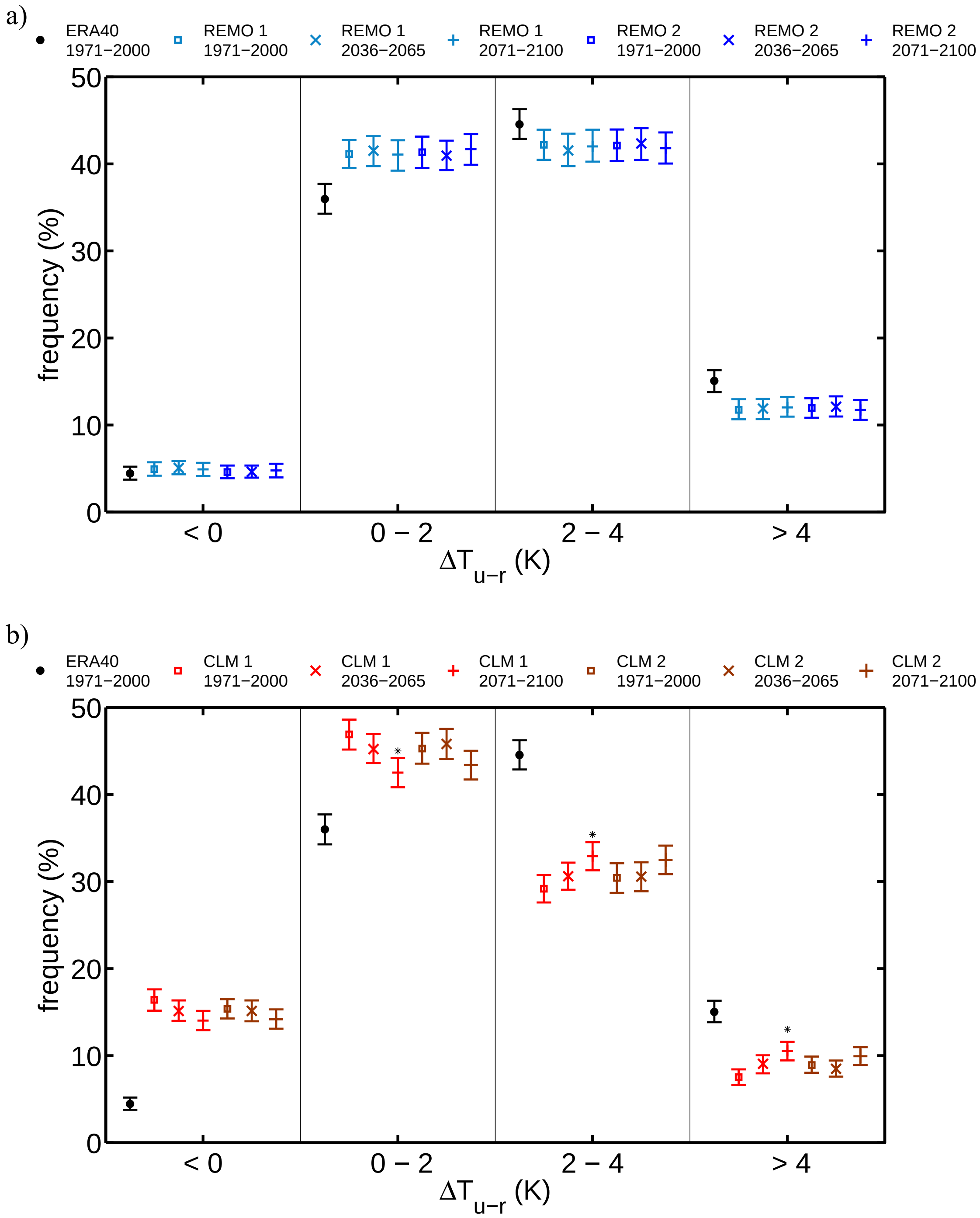

Figure 3.8: *Relative frequency of different modeled UHI intensities in summer (JJA) using ERA40 data and the two realizations of (a) REMO and (b) CLM for different time periods. Error bars indicate the 95% confidence intervals due to the unexplained variance. The black asterisks mark significant ($\alpha = 0.05$) changes between the corresponding period and the control period (1971-2000).*

The frequency of the four intensity classes using CLM as input for the model is shown in Figure 3.8b. The whole distribution of ΔT_{u-r} is shifted towards weaker UHI days. This results in an overestimation of negative and weak UHI days and an underestimation of moderate UHI days and strong UHI days in both realizations. The results of the scenario runs show that the distribution changes significantly ($\alpha = 0.05$) only in the first realization for the end of the century. The significance is tested using a two-sided *t*-Test. The frequency of weak UHI decreases significantly while moderate and strong UHI days become significantly more frequent. The tendencies are similar in the second realization for the end of the century but in this case not significant.

3.6 Conclusions

This study is the first using the results from the two RCMs REMO and CLM to obtain information about future urban climate through statistical downscaling. For that purpose a statistical model for the UHI of Hamburg was constructed using operational observations from the DWD (1985-1999). It is shown that UHI linearly depends on wind speed, previous day's cloud cover and relative humidity (all coefficients negative). The explained variance of the model is comparable with other statistical models for the UHI in other cities (e.g. Kim and Baik, 2004; Wilby, 2008). Applying this model to REMO and CLM output reveals that for CLM the mean UHI intensity is underestimated of about -0.7 K compared to results of ERA40. REMO results correspond well with the results of with ERA40 when comparing the period mean. For the monthly means however differences exist. The causes for the underestimation are primarily the unrealistic high cloud cover and relative humidity simulated by CLM. Therefore, regional climate model results should be bias-corrected in future studies to analyze changes in absolute values. Keeping this limitation in mind relative changes can be considered. For the future urban heat island the statistical model was applied to the SRES A1B emission scenario runs from REMO and CLM. The periods of interest were 2036-2065 and 2071-2100. The availability of two realizations of the A1B scenarios made it possible to check for the robustness of the changes.

The two RCMs show different signals for the future UHI. The results from REMO suggest that the average UHI will not change in the future. Regarding the annual cycle only two months (April and December) showed a significant decrease for both realizations. Additionally, the frequency of different UHI intensities does not change in the A1B scenario. According to the analysis of the future UHI using CLM the UHI intensity will change significantly. The annual cycle of the UHI will strengthen since July and August exhibit an increase, while the UHI decreases for the other months. Averaged over the whole year the UHI decreases slightly.

It should be stated that the method presented in this study does not take the atmospheric stability into account. Therefore, the possible effect of more unstable conditions in the future climate due to higher temperatures is not included in the model. In future studies this shortcoming could be solved using atmospheric profiles from sounding data or measuring towers such as the Wettermast in Hamburg. However, it is not clear whether the RCMs are able to represent the profiles well enough for an analysis.

Due to a lack of a dense observational network the information about the spatial properties of the UHI in Hamburg are limited. Other downscaling methods such as statistical-dynamical downscaling should be applied to obtain this information. With the help of the statistical model presented here, the days can be determined for which the UHI is most pronounced. These can be simulated with a mesoscale model that includes an urban parameterization such as done by Grawe et al. (2010) for London.

4 Weather pattern classification to represent the UHI in present and future climate

4.1 Preface

This Chapter has been submitted to Journal of Applied Meteorology as: "Hoffmann P, Schlünzen KH. 2012. Weather patterns and their relation to the urban heat island in present and future climate." For the thesis the text has been modified to be consistent with other parts of the thesis (e.g. colored figures) and by leaving out the Abstract and moving references to the end of the thesis.

4.2 Introduction

Circulation and weather pattern classification (WPC) has been widely used to identify relationships between atmospheric circulation and small scale meteorological elements such as heavy precipitation (e.g. Kaspar and Müller, 2010; Lupikasza; 2010), tornadoes (Bissolli et al., 2007), air quality (e.g. Demuzere and van Lipzig, 2010; Demuzere et al., 2010), and urban climate (e.g. Morris and Simmonds 2000; Mihalakakou et al. 2002; Kassomenos and Katsoulis, 2006). Also non-meteorological relationships such as between atmospheric circulation and human health have been investigated (Kyselý et al., 2010). Since a strength of climate models is to simulate large-scale atmospheric circulation, WPCs are applied in climate change research (Philipp et al., 2007; Demuzere et al., 2009; Jacobeit, 2010; Sheridan and Lee, 2010; Spekat et al., 2010). In particular, WPCs are used to statistically (e.g. Kreienkamp et al., 2010; 2011; Sauter and Venand, 2011) and to statistically-dynamically (e.g. Fuentes and Heimann, 2000; Boé et al., 2006; Pinto et al., 2010) downscale general circulation model (GCM) results.

In addition to the wide variety of applications, there is a comparably large set of methods used to classify weather patterns (WPs). The most commonly used method is cluster analysis, especially the non-hierarchical *k*-means method (Huth et al., 2008). Also the artificial neural network based method of Self-Organized Maps has been applied to WPC (e.g. Reusch, 2010). Several intercomparison studies show that although no optimal method exists, however, the *k*-means-based methods usually perform well (e.g. Beck and Philipp, 2010; Cahynová and Huth, 2010; Huth, 2010). As stated by Huth et al. (2008), the circulation patterns should be regarded as purpose-made. Therefore, each target parameter requires the construction of its own optimal classification.

In this study, we construct a WPC computed with a *k*-means-based method for the target parameter urban heat island (UHI). Hamburg (Germany) is used as an example to develop and apply the method. The UHI refers in the present paper to the higher nocturnal temperatures in urban compared to rural areas. It is caused by the higher heat capacity of urban surfaces, the trapping of radiation in street canyons, the reduced vertical exchange due to a reduced wind speed, and the anthropogenic heat release (Yow, 2007). The intensity of the UHI depends on the morphology and size of the urban area (Oke, 1973; Sakakibara and Matsui, 2005; Steeneveld et al., 2011) as well as on the meteorological situation (Arnfield, 2003). It is inversely related to wind speed, cloud cover, and relative humidity (e.g. Morris et al., 2001; Schlünzen et al., 2010; Hoffmann et al., 2011). There are also several studies investigating the dependency of the UHI intensity on the WP (e.g. Morris and Simmonds, 2000; Mihalakakou et al., 2002; Berjarán and Camilloni, 2003; Kassomenos and Katsoulis, 2006; Alonso et al., 2007). They showed that the UHI is well pronounced under anticyclonic conditions, which are mostly associated with weak pressure gradients and dry cloud-free conditions. Cyclonic WPs were found to suppress UHI development and sometimes lead to negative UHI intensities (Kassomenos and Katsoulis, 2006).

The UHI of Hamburg was first described by Reidat (1971). He found that in the period from 1931-1960 the temperatures at the downtown station Hamburg-St. Pauli (shortened SP) were up to 1 K higher than at the Airport Hamburg-Fuhlsbüttel (shortened FU) (Figure 4.1). Schlünzen et al. (2010) analyzed more recent data (1988-1997) from six stations in and around Hamburg. They received higher differences, resulting in 1.5 K higher minimum temperatures at SP compared to FU in the summer average. Besides SP and FU only a few other meteorological stations exist within the urbanized area of the state of Hamburg, some of which are no longer operational. To get detailed spatial information on the UHI, Bechtel and Schmidt (2011) used floristic mapping data with a horizontal resolution of 1 km in combination with the so-called Ellenberg indicator for temperature and the evaluated measured temperatures of Schlünzen et al. (2010). Their much more detailed temperature pattern clearly correlates with urbanization density and additionally shows the nighttime warming effects of the frequent rivers, lakes and canals in the city.

Hoffmann et al. (2011) constructed a linear model for the UHI of Hamburg and applied it to results of the regional climate models (RCM) REMO and CLM. Results show that the annual mean UHI intensity will not change in a future climate, but a decrease is found for April. Looking only at CLM results a decrease might also occur in some other months, while July and August might have an increased UHI. Only in summer months does a slight increase occur. However, since the statistical model explains only approximately 40% of the UHI variance, there are clearly additional contributing factors not considered in the statistical model. Therefore, WPs and a high-resolution dynamic simulation of the WPs could add more information.

In this paper the methodology of WPC is employed as a first step to determine UHI in a high-resolution using a mesoscale model. This statistical-dynamical downscaling approach needs forcing data at the outermost grid; therefore the WPC needs to be applicable for analyses data. Furthermore, it needs to be applicable to models of different resolution, including GCMs as well as RCMs. The climate models results are needed for a reliable estimation of the changes in WP and thus of the future UHI. In the following section, the observation and model data are described. Section 4.4 deals with the *k*-means-based clustering methods used for this study. In Section 4.5, the WPC, which is optimized for the UHI, is constructed. The resulting WPs are analyzed in current and future climate conditions in Section 4.6. Conclusions are drawn in Section 4.7.

4.3 Data

4.3.1 Routine observations

For the calculation of the UHI, routine observations carried out by the German Meteorological Service (Deutscher Wetterdienst (DWD)) are used. The locations of the measurement sites are given in Figure 4.1. All sites are climate stations which measure daily values for temperature (average, minimum, maximum), relative humidity, cloud cover, air pressure, precipitation, etc.. The site Hamburg-Fuhlsbüttel (FU) located at the Hamburg Airport is also a climate reference station as well as a synoptic station. Therefore, hourly values of the wind speed and wind direction are available at this site. This station is used to analyze the characteristics of the derived WPs. Since the WPs are determined daily (Section 4.5), wind speed is averaged for each day.

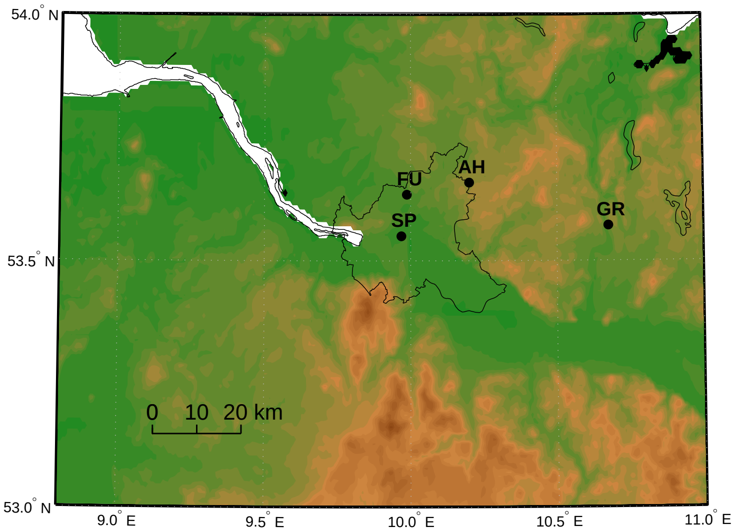

Figure 4.1: *Map of the metropolitan area of Hamburg with positions of the measurement sites AH (Ahrensburg-Wulsdorf), FU (Hamburg-Fuhlsbüttel), GR (Grambek), SP (Hamburg-St. Pauli) and political borders of the State of Hamburg.*

According to the study of Hoffmann et al. (2011), the UHI is defined as the difference of the daily minimum temperature at the urban site Hamburg-St. Pauli (SP) and average values of the daily minimum temperatures at the rural sites Grambek (GR) and Ahrensburg (AH):

$$\Delta T_{u-r} = T_{\min,SP} - \frac{(T_{\min,GR} + T_{\min,AH})}{2} \tag{4.1}$$

The site SP is located in downtown Hamburg and next to buildings, with up to 6 stories, and the Elbe River. Using available data from the period 1985–1999, ΔT_{u-r} shows an annual cycle with a maximum in the warm season of up to 2.7 K (monthly averaged) and an annual averaged value of 2.0 K (Hoffmann et al. 2011).

4.3.2 ERA40 re-analysis data

ERA40 re-analysis (Uppala et al., 2005) present a re-construction of the best possible estimate of past atmospheric states with the help of a data assimilation system and a global forecast model. The gridded dataset starts in September 1957 and ends in August 2002. In this study, only the full years from 1958 to 2001 are considered. The horizontal resolution of the dataset is 1.125° (~125 km). For the classification of WPs, variables at the 700 hPa pressure level are used. This level is chosen firstly to avoid problems due to topography in both ERA40 and in the RCMs, as well as to be as close to the surface as possible. 700 hPa values have been used in different studies investigating WPs (e.g. Huth, 1996; Christiansen, 2007); Sheridan and Lee (2010) stated that this level is reproduced reliably in GCM and reanalysis data.

Since it is unknown a priori which variables and which combination of variables should be used for the WPC, combinations of different variables are tested for their suitability: geopotential height (*GP*), 1000 hPa to 700 hPa thickness (*TH*), relative humidity (*RH*), and relative vorticity (*VO*). The GP is chosen to get information about the strength and the direction of the large-scale flow. As mentioned earlier, wind speed is an important factor for the development of an UHI. *GP* is always used for the WPC. As a measure for humidity, also important for UHI development, *RH* is chosen. Additionally, cloud cover is linked to *RH*. To gain information on the vertical movement of air masses which is needed to determine the potential for cloud formation, *VO* is chosen. This is an alternative to the vertical wind, which is not chosen since its values are very sensitive to the model employed. Positive VO values are mostly associated with upward vertical motion and vice versa. As several studies have shown, temperature seems to have only a small influence on the UHI. Nevertheless, temperature is an important variable for describing an air mass. As a robust measure for the temperature, the thickness (*TH*) between 1000 hPa and 700 hPa is employed. For the clustering, all fields are bilinearly interpolated on a 2.5° x 2.5° regular grid. This is done to partially remove small scale features and, therefore, the atmospheric noise that can hinder the identification of large-scale patterns using cluster analyses.

4.3.3 REMO

REMO is a hydrostatic RCM developed at the Max-Planck-Institute for Meteorology. The dynamical core is based on the Europa-Modell (Majewski, 1991) from the DWD whereas the physical parameterizations were taken from the GCM ECHAM4 (Roeckner et al., 2003). A detailed description of the model can be found in Jacob (2001) and Jacob et al. (2001). In REMO the prognostic equations for temperature, the horizontal wind components, surface pressure, mixing ratio of water and cloud water are solved on a rotated grid. The climate simulations used in this study are forced with the ECHAM5-MPIOM (Roeckner et al., 2003, Jungclaus et al., 2006) A1B scenario simulations. The REMO simulations are intended to represent the regional climate for Germany at a final resolution of about 0.088° (~10 km) using two-step nesting (Jacob et al. 2008). Since the classification domains (Section 4.5.1) are larger than the highest-resolved model domain, the results of the coarser resolved domain with a resolution of about 0.44° (~50 km) on a rotated grid are used. An ensemble of three realizations of the A1B scenario simulations is available. This gives the opportunity to account, to some extent, for the climate variability (Schoetter et al., 2012).

GP, *TH* and *RH* are directly available in the model output. *VO* has to be calculated from the *u*- and *v*-components of the wind by using the definition of the vertical component of the vorticity vector:

$$VO = \frac{\partial v}{\partial x} - \frac{\partial u}{\partial y} \tag{4.2}$$

All variables are bilinearly interpolated to the 2.5° x 2.5° regular grid to match the grid used for the WPC.

4.3.4 CLM

CLM is a non-hydrostatic RCM based on the Lokal-Model (LM) from the DWD. The model is described by Böhm et al. (2006) and detailed information about the dynamics and physics are given by Steppeler et al. (2003). The prognostic variables of the model are: temperature, horizontal and vertical wind components, pressure perturbations, specific humidity and cloud water content. A detailed description of the IPCC simulations used in this study is given by Hollweg et al. (2008). As with the REMO simulations, the same ECHAM5 A1B scenario simulations are used as a forcing at the lateral boundaries. However, instead of nesting the model twice, CLM is directly nested into the ECHAM5 results. The model domain covers nearly the same area as the 50 km results from REMO but on a finer horizontal resolution of 0.165° (~18 km). Only downscaled simulations of the first two realizations of the A1B Scenario simulations are available. Again, the variables *GP*, *TH* and *RH* are directly available, and *VO* is calculated using Eq. (4.2).

4.4 Clustering Methods

The aim of WPC is to find patterns of meteorological fields which are similar within each cluster and dissimilar between different clusters (Huth et al. 2008). In the framework of COST733, several studies have been conducted which focused on comparison of different WPC methods (e.g. Huth 2010; Beck and Philipp 2010; Cahynová and Huth 2010). The results show that there is no single best method. However, *k*-means-based methods rank high in these studies. In addition, with the *k*-

means method, one can apply the same distance measures to both the clustering and the assignment of data from different models to the resulting WPs.

The results of the *k*-means methods are highly dependent on the choice of the initial conditions. Several studies have sought to overcome this disadvantage, such as through the extended *k*-means method (e.g. Enke and Spekat, 1997; Philipp et al., 2007). Three different methods, *k*-means, dkmeans and SANDRA, are tested here to achieve the best results. The computation of the clustering is done with the classification software developed during the COST733 action (Philipp et al., 2010). In the following the three clustering methods are briefly described.

4.4.1 k-means

The *k*-means method is a non-hierarchical cluster algorithm, which groups objects into mutually exclusive clusters. The number of clusters *k* has to be prescribed for this method. The similarity measure is the squared Euclidian distance *SED* between two data objects (vectors including fields of one or more variables) $\boldsymbol{x}_1$ and $\boldsymbol{x}_2$:

$$SED = \left\| \mathbf{x}_1 - \mathbf{x}_2 \right\|^2 \tag{4.3}$$

This measure is then used to define the so called within-cluster sum of squares *WSS*:

$$WSS = \sum_{i=1}^{k} \sum_{x \in C_i} \left\| \mathbf{x} - \mathbf{z}_i \right\|^2 \tag{4.4}$$

where x denotes all data objects belonging to the cluster C_i; $\mathbf{z}_i$ is the ith corresponding cluster centroids (CC) and k is the number of clusters. Since several variables are used in this study, the data objects of each variable are normalized by subtracting their corresponding temporal-spatial mean and dividing it by their standard deviation afterwards.

The *k*-means algorithm tries to determine the minimum of the WSS in an iterative process. The first step is the so-called starting partition where *k* CCs are chosen. The *SED* is computed for each combination of CC and data objects. All data objects are then assigned their nearest CC to form the cluster. The data objects belonging to each cluster are averaged to yield the new CC. Thereafter, the *SED* for all objects and the new CC are computed and the objects are reassigned to their nearest CC. This iterative process of reassignment and calculation of *SED* stops when no data point needs to be reassigned to another CC. To achieve some independence of the staring partition, the *k*-means algorithm is repeated 1000 times using different starting partitions. The quality of a classification result is reflected by the explained cluster variance (*ECV*). The *ECV* is based on the ratio of the *WSS* and the total sum of squares (*TSS*):

$$ECV = 1 - \frac{WSS}{TSS} \tag{4.5}$$

The *ECV* ranges from 0 to the optimal value of 1. Therefore, the result with the highest *ECV* is chosen as the final classification result.

4.4.2 dkmeans

A crucial point using *k*-means clustering is the starting partition. The so-called dkmeans method (Enke and Spekat, 1997, Philipp et al., 2010) uses the most dissimilar data objects as a starting partition. These objects are indentified by an iterative algorithm. In contrast to the *k*-means method, the Euclidian distance *ED* is used as a similarity measure:

$$ED = \sqrt{\left\| \mathbf{x}_1 - \mathbf{x}_2 \right\|^2} \tag{4.6}$$

Again, all objects are normalized before the *ED* is calculated. After the most dissimilar CCs are found, all the remaining objects are assigned to their most similar CC to form a cluster. As with the *k*-means method, the new CCs are calculated and all objects are reassigned to their most similar CC. The iterative process of reassigning the data objects and calculating the new CCs stops if no object needs to be reassigned during an iteration step.

4.4.3 SANDRA

The conventional *k*-means clustering algorithm tends to reach local minima of the sum of squares *WSS* too often. This problem can be avoided by using the simulated annealing and diversified randomization method (SANDRA) developed by Philipp et al. (2007). Diversified randomization means that the clustering is done several times with randomized starting partitioning of the data, and during the clustering the ordering of the data objects and the cluster numbers are randomized. Simulated annealing allows data objects to be assigned to a 'wrong' cluster during the iteration process, meaning that the object is not necessarily assigned to its closest CC. At first, this causes the *WSS* to increase. However, this process can prevent misidentification of a local minimum as the global minimum. In practice, each data object can be moved into a 'wrong' cluster if the acceptance probability P is larger than a random number between 0 and 1. P is given by:

$$P = \exp\left(\frac{ED_{old} - ED_{new}}{T}\right) \tag{4.7}$$

where ED_{old} is the Euclidian distance between the data object to the old cluster, ED_{new} is the Euclidian distance to the potentially new cluster, and T is a control parameter which is reduced after each iteration step by a constant factor CO:

$$T_{i+1} = CO \cdot T_i \tag{4.8}$$

CO is the so-called cooling rate, which is set to 0.999 in this study. The initial T is empirically chosen in a way that 99% of the objects are moved during the first iteration step. The clustering process is finished when no reassignment is possible and no 'wrong' reassignment has appeared in an iteration step. As it is done for *k*-means and dkmeans, all data objects are normalized to assure comparability between the different variables used for the WPC.

4.5 Optimal method for weather pattern classification based on ERA40 data

In addition to the clustering method, the choice of the number of weather patterns, the classification domain, and the meteorological variables used for the classification are important to achieve the optimal WPC. Both the domain and classification variables should be chosen based on the target parameter: in this case the UHI. To quantify the quality of the performance of the classification, the explained variance of the UHI is calculated. The optimal clustering method and the optimal cluster number for the classification can be determined by statistical measures. In the following the two domains, the statistical measures and the results of the classification are presented.

4.5.1 Domain

Several studies show that the size of the domain is important in order to achieve optimal results with the WPC (e.g. D'onofrio et al., 2010; Demuzere et al., 2010; Beck, 2011). In the cited studies small domains gave the best results. To verify this finding, two domains of different size are tested for use in the classification (Figure 4.2). The larger of the two domains covers Central Europe, including the Alps and parts of Scandinavia and Great Britain. The smaller domain covers Germany, the Benelux countries, southern Scandinavia and parts of France, Poland and the Czech Republic. It has a size of about 1700 km in North-South direction and between 1200 and 1700 km in East-West direction. Smaller domains than this would likely be too small to sufficiently resolve synoptic-scale features such as high pressure systems. The decision, which domain yields better results, is based on the target parameter.

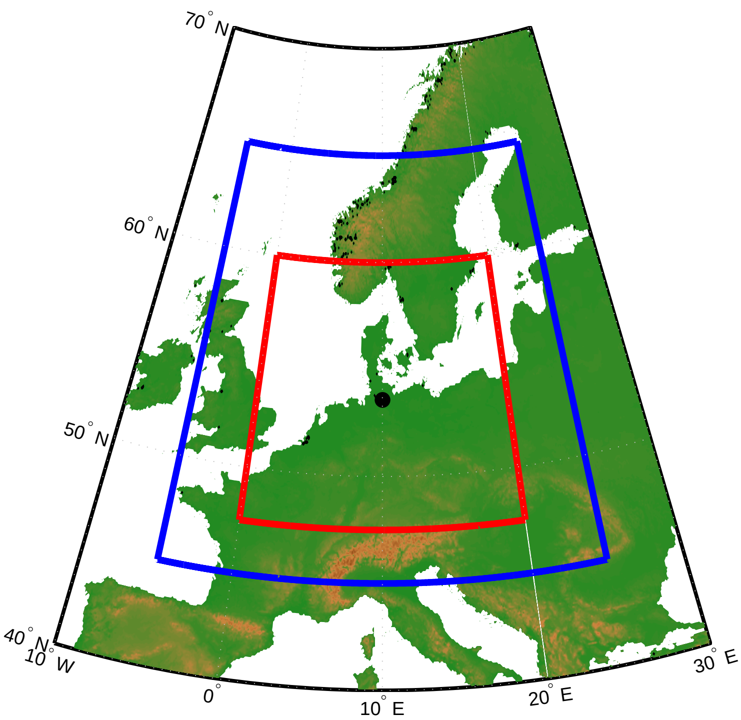

Figure 4.2: *Map of Europe. The red box indicates the small classification domain and the blue box the large classification domain. The position of Hamburg is indicated by the black dot.*

4.5.2 Statistical measures to determine the optimal cluster number

The existence of distinct WPs has been debated (e.g. Philipp et al., 2007; Stephenson et al., 2004) and the problem of identifying the optimal number of WPs also remains unresolved (e.g. Philipp et al., 2007; Fereday et al., 2008; Huth et al., 2008). Several statistical measures currently exist for the estimation of optimal cluster numbers. Some are more suitable for WPCs than others. For instance, Philipp et al. (2007) apply a method based on the Petit test introduced by Gerstengarbe and Werner (1997) that gives no satisfactory results in the present application (not shown). Instead four other measures are applied to get an optimal cluster number.

DVIndex introduced by Shen et al. (2005) is based on the assumption that for optimally clustered data, the clusters are compact and well separated from each other. With increasing cluster number the intra-cluster compactness increases while the inter-cluster separation decreases. The sum of both should be at a minimum to achieve the optimal cluster number. Hence, the *DVIndex* is defined as:

$$DVIndex(k) = IntraRatio(k) + \gamma \cdot InterRatio(k) \tag{4.9}$$

As a measure of compactness, the average sum of distances between the CCs and N data objects is used (Eq. 4.10). *Intra* is normalized by its own maximum (Eq. 4.11), calculated from the *Intra* values received for cluster numbers k=2 to a pre-defined upper limit $k = K$ (Eq. 4.12).

$$Intra(k) = \frac{1}{N} WSS(k) \tag{4.10}$$

$$IntraRatio(k) = \frac{Intra(k)}{MaxIntra} \tag{4.11}$$

$$MaxIntra(k) = \max_{k=2,\ldots,K} (Intra(k)) \tag{4.12}$$

The separateness is expressed as the ratio of the maximum and the minimum *SED* between the CCs, multiplied by the sum of the inverse distances between the CCs (Eq. 4.13).

$$Inter(k) = \frac{Max_{i,j}\left(\left\|\mathbf{z}_i - \mathbf{z}_j\right\|^2\right)}{Min_{j\neq i}\left(\left\|\mathbf{z}_i - \mathbf{z}_j\right\|^2\right)} \cdot \sum_{i=1}^{k} \left(\frac{1}{\sum_{i=1}^{k}\left(\left\|\mathbf{z}_i - \mathbf{z}_j\right\|^2\right)} \right) \tag{4.13}$$

To be consistent with the calculation of the compactness, *Inter* is normalized by its maximum (Eq. 4.14), determined by calculating *Inter* for cluster numbers from $k = 2$ to $k = K$ (Eq. 4.15).

$$InterRatio(k) = \frac{Inter(k)}{MaxInter} \tag{4.14}$$

$$MaxInter(k) = \max_{k=2,\ldots,K}(Inter(k)) \tag{4.15}$$

The factor γ in Eq. (4.9) is a tuning parameter to account for the noise in the data ($0 < \gamma < 1$) or to give the compactness more relevance ($\gamma > 1$). For $\gamma = 1$, the assumption is made that no noise exists in the data. This is not the case for atmospheric data and especially WPs. Therefore, γ should be smaller than 1 when applying it to weather pattern classification. After testing the *DVIndex* across a spectrum of γ values, a value of 0.5 was found to produce appropriate results for this implementation.

The second measure used in this study is the *Validity* index (Eq. 4.16) introduced by Ray and Turi (2000). The basic idea is similar to that of the *DVIndex*. However, the *Validity* Index is defined as the ratio of the intra-cluster difference *Intra* (Eq. 4.11) and the minimum *SED* between the CCs:

$$Validity(k) = \frac{Intra(k)}{\min_{i \neq j}\left(\left\|\mathbf{z}_i - \mathbf{z}_j\right\|^2\right)} \tag{4.16}$$

For the optimal cluster number the Validity index should be minimal, which corresponds to compact and well separated clusters.

In addition to the two measures introduced before, two simple measures are applied as well. They are used, if the other ones do not give a well-defined answer for the optimal cluster number. Both measures focus on the similarity of the nearest clusters, which should be as different as possible. One measure is the minimum *SED* (Eq. 4.17), and the other is the maximum of the spatial correlation between the CCs (Eq. 4.18).

$$Min_{SED} = \min_{i \neq j}\left(\left\|\mathbf{z}_i - \mathbf{z}_j\right\|^2\right) \tag{4.17}$$

$$Max_{Corr} = \max_{i \neq j}\left(\frac{\mathrm{cov}(\mathbf{z}_i, \mathbf{z}_j)}{\mathrm{var}(\mathbf{z}_i) \cdot \mathrm{var}(\mathbf{z}_j)}\right) \tag{4.18}$$

Min_{SED} should have a local maximum for the optimal cluster number and Max_{Corr} a local minimum.

4.5.3 Classification results

To avoid seasonality and still have enough days available to derive clusters, the ERA40-data are divided into the four seasons: MAM, JJA, SON and DJF. As a first step the classification is done for all possible combinations of methods, domains, seasons and classification variables using cluster numbers from $k = 6$ to $k = 15$. Results of similar studies show that the optimal number lies in this range (e.g. Enke and Spekat, 1997; Boé and Terray, 2008; Philipp et al., 2007; Fereday et al., 2008). In addition, classifications with small cluster numbers might be considered as circulation or weather regimes and not WPs (Huth et al., 2008; Cassou et al., 2011).

Using the classification dkmeans, some clusters only consist of 1 or 2 days. One explanation could be outliers in the ERA40-data, which form their own clusters, because all other data objects are assigned to the remaining clusters. This is possible with the dkmeans method because it finds the most dissimilar data objects, which could be the outlier of the dataset in some cases.

Following Philipp et al. (2007), the explained cluster variance *ECV* (Eq. 4.5) is calculated for each of these classifications to decide which clustering method performs best. The *ECV* is averaged over the results of each of the three clustering methods. First, only classifications results where dkmeans produces no single member cluster are used for the comparison. The *ECV* does not dramatically differ between the methods. However, as expected, the most sophisticated method, SANDRA, performs best ($ECV = 0.51$). The k-means ($ECV = 0.49$) and dkmeans ($ECV = 0.48$) perform almost equally well, with a slightly higher mean *ECV* for the k-means method. Thereafter, classification tests are restricted to the top two performing methods, SANDRA and k-means, for the set of cluster numbers 6-15. Again, SANDRA ($ECV = 0.51$) performs better than the k-means ($ECV = 0.49$) method. The differences seem marginal; however every improvement in the ECV improves the detectability of the WPs in data from different models. Hence, SANDRA is selected for use as the WPC method.

The optimal domain is determined by calculating the explained variance R^2 (Eq. 4.19) of the UHI for classification results from SANDRA for all combinations of domain, seasons and classification variables, using cluster numbers from 6 to 15.

$$R^2 = \left(\frac{\mathrm{cov}(\Delta T_{u-r}, (\Delta T_{u-r})_{WP})}{\mathrm{var}(\Delta T_{u-r}) \cdot \mathrm{var}((\Delta T_{u-r})_{WP})} \right)^2 \cdot 100\% \tag{4.19}$$

ΔT_{u-r} is the time series of the observed UHI intensity (Eq. 4.1) and $(\Delta T_{u-r})_{WP}$ is the time series of the averaged ΔT_{u-r} values for the corresponding WPs. Averaging the results over all seasons, classification variables and cluster numbers reveals that the smaller domain ($R^2 = 15\%$) explains slightly more variance than the large domain ($R^2 = 14\%$). Following this result the smaller domain is chosen for the final WPC.

The optimal variables are determined using R^2 as well. Figure 4.3 shows the R^2 values averaged for the different combinations of classification variables. The differences are small. However, just using the geopotential height yields the lowest R^2 and the combination of all 4 variables the highest. Hence, the final WPC uses all variables.

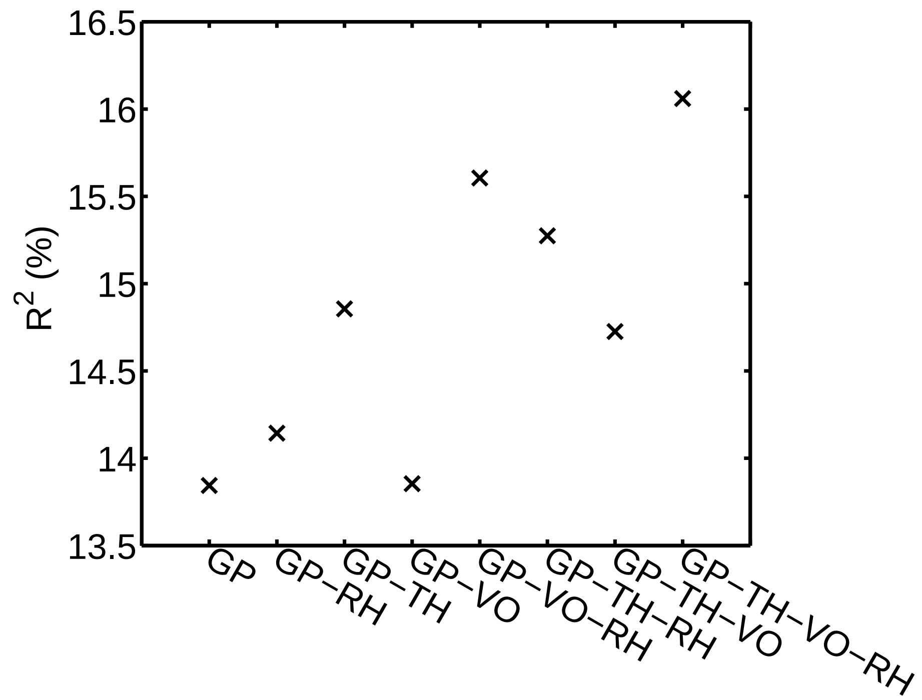

Figure 4.3: *Averaged explained variance R² (Eq. 4.20) of the UHI for the weather pattern classification SANDRA with different combinations of variables using the small domain (Figure 4.2). Data for 1985-1999.*

After choosing the method, the domain, and the classification variables, only the number of the cluster k remains to be determined. To compute the statistical measures introduced in Section 4.5.2, the classification is done for cluster numbers $k = 2$ to $k = 24$. For a better comparison all measures except for the Max_{Corr} are normalized by subtracting their minimum and than dividing by their range, so that for all measures the upper limit is 1 and the lower limit is 0. The resulting values for the different seasons are given in Figure 4.4. It is apparent that the curves for the *Validity* index and the *DVIndex* are similar, which can be expected, since both are both based on a similar idea. Except for SON, the optimal cluster number following *Validity* index and *DVIndex* would be 4 and 5. Also Max_{Corr} and Min_{SED} would support these numbers.

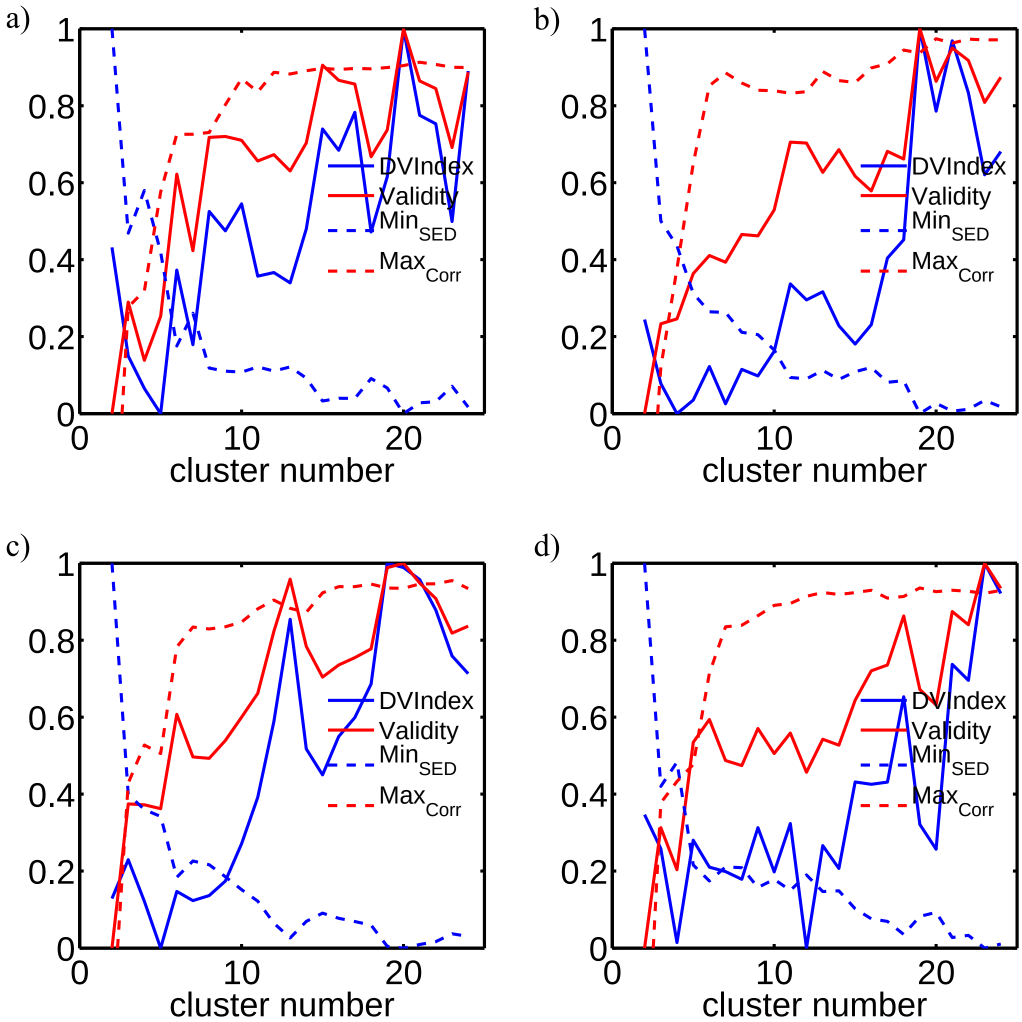

Figure 4.4: *Normalized statistical measures for the determination of the optimal cluster number for (a) DJF, (b) MAM, (c) JJA, and (d) SON.*

However, we decided for a cluster number of 6 or larger, since classifications with lower cluster numbers indicate more weather regimes than WPs. Applying this restriction, 3 of the 4 measures indicate 7 as an optimal number for k for DJF, only Max_{Corr} doesn't show a clear relative minimum for that number (Figure 4.4a). Nevertheless, the value of Max_{Corr} is still small and stays almost constant between 6 and 8 clusters. Therefore, 7 can be supported as the optimal cluster number. For MAM it is more difficult to find the optimal k since the minimum of the *Validity* index is not as well defined (Figure 4.4b). The *DVIndex* shows a minimum for $k = 7$, for which the *Validity* index also shows a weak minimum. In contrast, Max_{Corr} reaches a local maximum for this cluster number. Figure 4.4c shows that for JJA neither the *DVIndex* nor *Validity* indices show a clear minimum for cluster numbers greater than 5. The minimum of both, *Validity* index ($k = 8$) and *DVIndex* ($k = 7$) is not well defined. The *Validity* index for $k = 7$ is only slightly larger. Using Min_{SED} and Max_{Corr} does not help in this case, Min_{SED} would support $k = 7$ and Max_{Corr} $k = 8$. In the end, we chose 7 as the number of WPs for JJA because Min_{SED} is more important than Max_{Corr} since the *SED* is used as a similarity measure for SANDRA and not the correlation. Contrary to the other seasons, the *DVIndex* has an absolute minimum for 12 clusters during SON (Figure 4.4d). The *Validity* index as well as Min_{SED} also support this number. Thus, we chose 12 for the clustering of this season: The results are summarized in Table 4.1.

Table 4.1: *Specifications for the weather pattern classification derived to describe the UHI of Hamburg.*

Classification method	Data	Domain	Variables	Number of clusters			
				DJF	MAM	JJA	SON
SANDRA (Philipp et al., 2007)	ERA40 re-analysis from 1958-2001	0-20° E; 47.5-60° N (2.5° x 2.5° grid)	*GP*, *TH*, *VO*, *RH*, details in Section 4.3.2	7	7	7	12

In the following, only the summer season JJA is analyzed since this time of the year is the season with the largest ΔT_{u-r} (Schlünzen et al., 2010; Hoffmann et al., 2011) and most relevant for planning adaptation measures in case the UHI increases. The cluster centroids and the frequency of the WPs for JJA are given in Figure 4.5. SANDRA, as a *k*-means based method, produces almost equally sized clusters with WP frequencies from 11% to 16%. A short description of the WP characteristics is giving in the following:

WP1 – weak West-East gradient with ridge to the West and northerly flow, dry air masses South-West of the domain

WP2 – trough over the North Sea with strong gradients and southwesterly flow, moist air masses over the whole domain

WP3 – anticyclonic conditions with very weak gradients, warm and dry air masses advected from Southwest

WP4 – zonal flow and temperature conditions with strong gradients to the North, advection of dry air masses from West

WP5 – trough over Eastern Scandinavia, advection of cold air masses from Northwest, relatively dry air over the domain

WP6 – weak East-West gradient with ridge to the East, advection of warm air masses from Southeast

WP7 – trough over Scandinavia, advection of cold air masses from Northwest similar to WP5, moist air masses over the whole domain

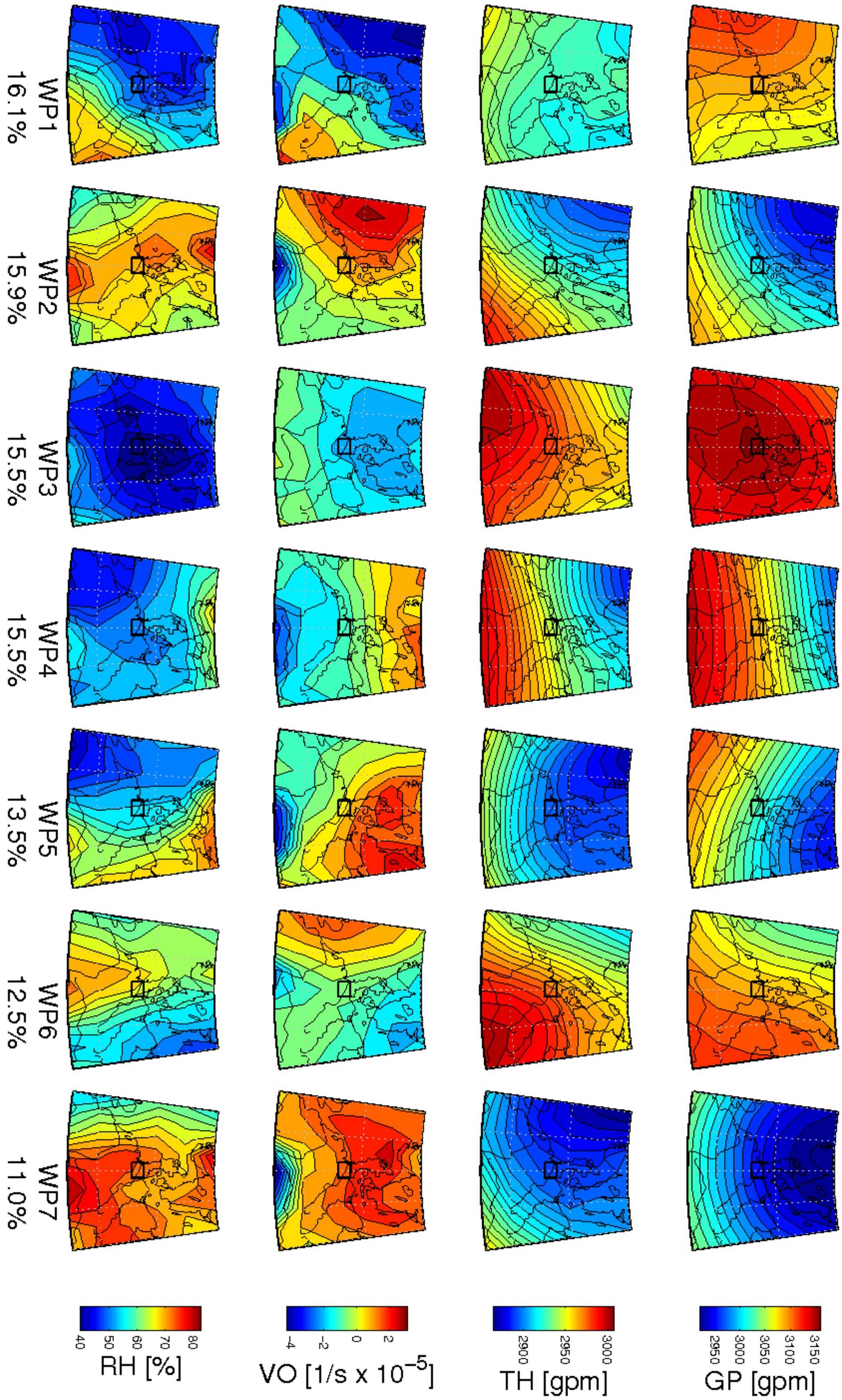

Figure 4.5: *Cluster centers of each variable (relative humidity RH, vorticity VO, 1000 hPa-700 hPa thickness TH, Geopotential height of 700 hPa level GP) and the frequency for all weather patterns in JJA obtained by ERA40-data for the period 1958-2001.*

Based on duration analyses, WP1 is a transition WP, since in 90% of the occurrence WP1 last only 1 day. WP3 is the most persistent WP, with 13% of its occurrences exceeding 5 days in length, followed by WP7 with 10%.

The meteorological conditions in Hamburg associated with the different WPs are shown in Figure 4.6. With exception of ΔT_{u-r}, all variables are taken from the DWD station FU (Figure 4.1). The corresponding explained variances are shown for the different variables as well. About 18.6% of the ΔT_{u-r} variance can be explained by the WPs. This is comparable with the dependency of the UHI on wind speed alone as described by Hoffmann et al. (2011). WP3, and to some extent, WP1, WP4 and WP6 are associated with a strong UHI, while for days with WP5 and WP7 only low intensities were derived from the measurements. WP3 reflects the meteorological situation described in the literature (e.g. Kassomenos and Katsoulis, 2006) that is generally assumed to be most favorable for the development of a strong UHI. WP3 is associated with the lowest values for wind speed, cloud cover, relative humidity, and precipitation and with the highest temperatures for all WPs. The conditions for WP1 and WP6 are not as favorable for the UHI as WP3. However, they both have the tendency to smaller values of wind speed, cloud cover and relative humidity. In contrast, WP5 and WP7 are associated with high values for these 3 variables, which inhibit the development of an intense UHI.

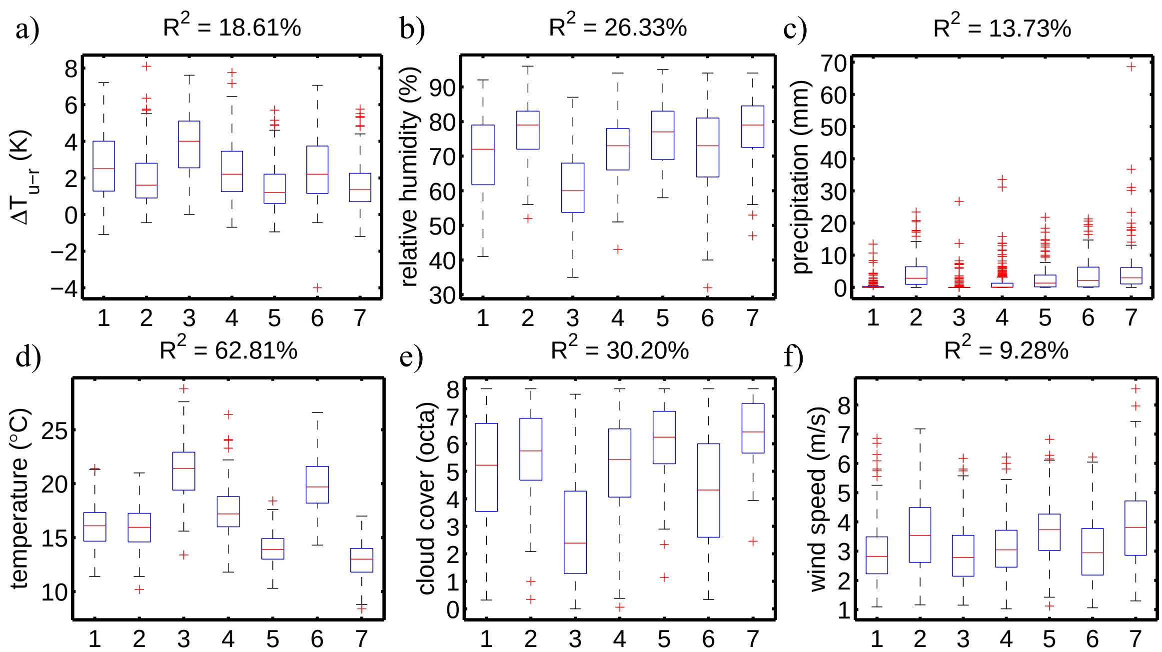

Figure 4.6: *Boxplots and explained variance R^2 for the a) urban heat island as defined in Eq. (4.1), b) daily averaged relative humidity, c) daily precipitation, d) daily averaged temperature, e) daily averaged cloud cover and d) wind speed for the WP and season JJA. Except for the urban heat island all variables are obtained from observations at Hamburg-Fuhlsbüttel. Data for the period 1985-1999.*

4.6 Weather patterns and UHI based on regional climate model results for present and future climate

To analyze possible changes of the WPs and the UHI in the future, the RCM data are assigned to the WPs constructed in Section 4.5 (Table 4.1). As done for the classification, the *SED* (Eq. 4.3) is used as a similarity measure. A day is assigned to a WP if the *SED* is smallest compared to the corresponding ERA40-CC. To compute the *SED* the different variables of the RCM data have to be normalized. There are several ways to normalize RCM data. Following one method, the differences from their own mean can be normalized using their own standard deviation. However, if the RCM standard deviation differs substantially between ERA40 and the RCM, the features of the pattern could change which could then lead to false assignments. For instance, a weak low pressure system would be assigned to a strong low pressure pattern, if the standard deviation of the RCM is in general smaller than standard deviation of ERA40. To partly counteract this possibility, the data are normalized by the standard deviation of the corresponding ERA40 data (1971-2000) and subtracted by the mean of the RCM.

4.6.1 Present Climate

The frequencies of the ERA40 and the assigned RCM WPs are shown in Figure 4.7 for the same time period (1971-2000). The uncertainty due to climate variability is obtained by bootstrap re-sampling (Efron and Tibshirani, 1993) of the annual values of the frequency for JJA ($N = 10000$). The 95% confidence intervals indicated by the error bars in Figure 4.7 show that the climate variability of the WP is large. Therefore, the frequencies of RCM WPs and the ERA40 WPs only rarely differ significantly. WP1 is significantly underestimated by the first realization of REMO and WP4 by the second realization of REMO. Of interest is that for these two WPs the first realization of REMO and the other two realizations differ substantially, while the inter-realization difference for all other WPs is small. Both WPs are more or less associated with anticyclonic flow. However, the location of the ridge is shifted. This slight shift in the position of the high pressure systems causes the differences in the frequency. In addition, the presented confidence intervals represent only the high frequency climate variability and not the low frequency variability, which was observed for several circulation types by Philipp et al. (2007). In contrast to REMO, the two realizations of CLM do not differ significantly compared to the ERA40 WPs as well as among each other.

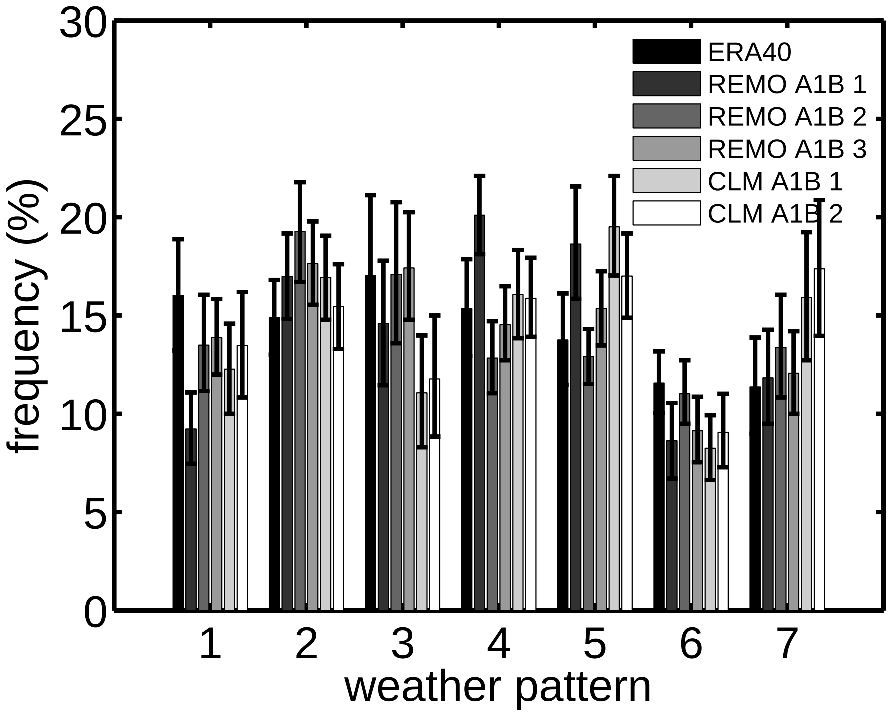

Figure 4.7: *Frequency of weather patterns in ERA40 and the different simulations from the RCMs for JJA in present climate (1971-2000). The error bars indicate the 95% confident intervals calculated with bootstrap re-sampling.*

4.6.2 Future Climate

For the determination of WPs in the future climate, it is assumed that no new WPs will occur in the future. This might not be valid since some studies predict new WPs in the future climate (e.g. Kreienkamp et al., 2010, Belleflamme et al., 2011). However, in the study of Belleflamme et al. (2011), the new WPs had only higher geopotential height compared to the old WPs, but the patterns were similar to the existing WPs. Therefore, we conclude that the patterns might not change, only the level of the geopotential height, and that this has to be investigated for every individual classification.

The change of frequency of the WPs, ΔWP, is calculated for two future time periods, namely 2036-2065 and 2071-2100 using:

$$\Delta WP = \frac{f(WP)_f - f(WP)_c}{f(WP)_c} \cdot 100\% \tag{4.20}$$

$f(WP)_c$ and $f(WP)_f$ are the absolute frequencies of the WPs in the current and in the future climate, respectively. For this calculation, the three realizations of REMO and the two realizations of CLM are combined. The realizations are each equally probable projections of the future climate. Confidence intervals of the changes are again determined using bootstrap re-sampling ($N = 10000$).

The frequency changes ΔWP for the two periods are shown in Figure 4.8. For the mid-century period (2036-2065) only the decrease of WP2, associated with weak to moderate values of ΔT_{u-r}, and the increase of WP7, associated with weak values of ΔT_{u-r}, are statistically significant in REMO. The pattern of the frequency changes is, to some extent, similar for both RCMs. For instance, both RCMs show a non-significant decrease of WP1, and a non-significant increase of WP3. The changes for the end of the century are larger for some WPs, especially for WP4 and WP5. The absolute frequency of WP4 significantly increases by 40% (REMO) and 17% (CLM), while the absolute frequency of WP6 significantly decreases by 26% (REMO) and 20% (CLM). To a smaller extent, the ERA40 WPs show similar tendencies conducting a linear trend analysis for the period 1958-2001 (not shown). WP3, which is associated with high ΔT_{u-r} values, does not show any significant changes in the frequency, which could mean that the conditions for strong UHI days will not change based on the WPs.

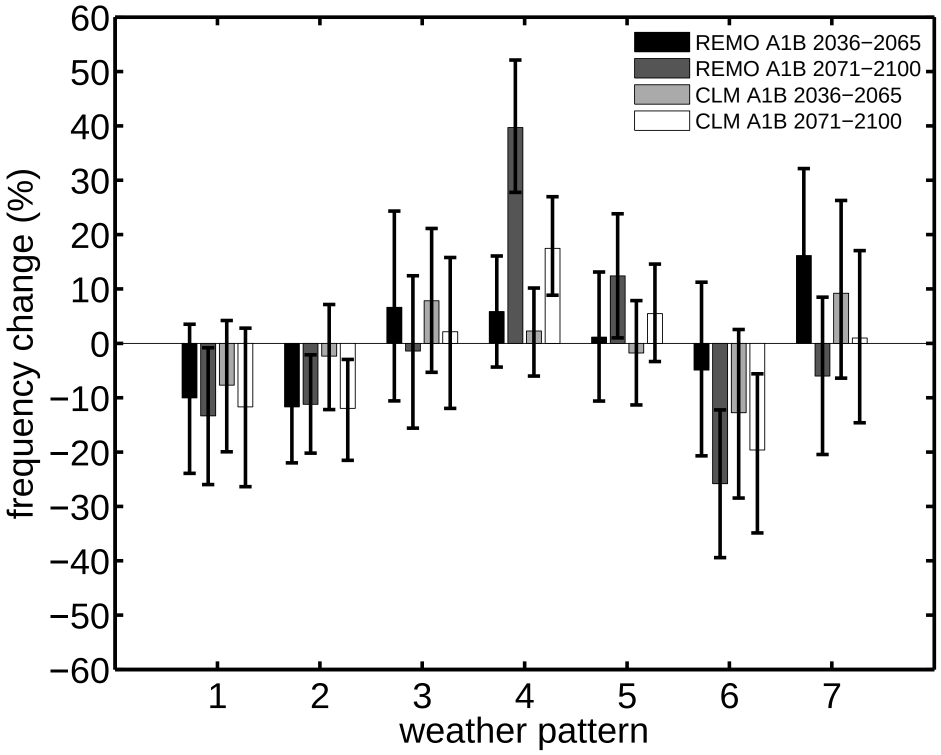

Figure 4.8: *Frequency changes of weather patterns* ΔWP (Eq. 4.20) *in JJA for 2036-2065 and 2071-2100 compared to 1971-2000. The three realizations of REMO and the two realizations of CLM are per RCM combined. The error bars indicate the 95% confident intervals calculated with bootstrap re-sampling.*

The changes in the future UHI due to the WP frequency changes are quantified using a simple regression analyses. For each WP the mean UHI is calculated. The mean and the difference of WP-based ΔT_{u-r} values for the different 30-year periods and both models are given in Table 4.2. Even though the frequencies of the WPs changes, the mean ΔT_{u-r} based on WP changes only slightly for both periods. This means the frequency of the WPs changes in such a way that the mean UHI will not change in the future. This result confirms the findings of the statistical model derived by Hoffmann et al (2011).

Table 4.2: *ΔT_{u-r} in present and future climate based on the weather pattern classification for JJA.*

Model	1971-2000	2036-2065		2071-2100	
	ΔT_{u-r}	ΔT_{u-r}	difference	ΔT_{u-r}	difference
REMO	2.36	2.37	0.01	2.38	0.02
CLM	2.41	2.42	0.01	2.40	-0.01

4.7 Conclusions

In this study a WPC was constructed to investigate the future changes in the UHI focusing on Hamburg (Germany). The clustering method, domain and variables are derived using statistical measures. The clustering method is determined based on how well it can group the atmospheric variables used in the classification. This approach is especially important when also applied to assign RCM data to WPs. If the WPs are not well separated, the detection of the WPs in RCMs becomes difficult.

As in previous studies (e.g. Huth, 2010), the SANDRA method performs better than the *k*-means method and the dkmeans method. However, the differences in *ECV* are not very large and the WP-means look very similar (not shown). The domain and classification variables were chosen to best represent this study’s target parameter, the UHI of Hamburg.

For *k*-means-based methods, the number of clusters *k* has to be set prior to the clustering. Statistical measures are calculated to find the optimal *k*. As in many studies the optimal cluster number was found to be in the range of 4-5. However, as pointed out by Huth et al. (2008), low numbers of clusters can be regarded more as weather regimes than WPs. The analysis focuses on the summer, since this is the relevant season for climate change adaptation when UHI is concerned. Using the summer WPC, only 18.9% of the UHI variance is explained. This is comparable with the UHI variance explained by wind speed alone (Hoffmann et al., 2011). However, it should be kept in mind that this was achieved using only 7 WPs. With a higher number of WPs the explained variance would be higher, but the detection of WPs in RCM would be more difficult and might lead to less robust results.

The next steps should be an analysis similar to Mihalakakou et al. (2002). It could be tested if the combination of the WPC and local variables, used by Hoffmann et al. (2011), for the statistical model of Hamburg's UHI explains more UHI variance than just using the statistical model or just using the WPC approach.

The assignment of RCM data to the ERA40 WPs showed that despite the large variability of the WPs, there are significant biases in the WP frequencies for the current climate. Since these biases are different for the different realizations of the RCM projections they could be caused by long-term variability. Long-term variability is also a problem when evaluating future changes of the WP's frequencies. By combining the realizations, the robustness of the signals improves, because they partially account for long-term variability. In addition, the changes are, to some extent, consistent between the periods and also between the models. The consistency between the models can be explained partially by the use of the ECHAM5 as the driving model. Hence, in future studies an ensemble of GCM-RCM combinations should be analyzed.

The largest changes occur for the zonal WP (WP4) associated with a large pressure gradient and advection of dry air masses (17-40% increase at the end of the century) and WP6 (20-26% decrease at the end of the century) associated with a ridge east of the domain and advection of warm air masses from the south-east. WP3, which is associated with strong UHI intensities, shows no significant changes in both periods. These findings are, at first glance, contrary to the results from trend analyses of observed circulation types, which have found an increase of anticyclonic and a decrease of cyclonic conditions over Europe in summer (e.g. Kyselý and Huth, 2006; Kostopolou and Jones, 2007; Guentchev and Winkler, 2010). However, most of these studies focus on large domains, which cover areas larger than continental Europe. Using a smaller domain, centered over Belgium, Demuzere et al. (2009) showed that the westerly WP increased in the ECHAM5 A1B scenario simulation. However, they did not analyze the summer season because of too large biases in the WP frequencies in that season.

To investigate how the mean UHI will change due to changes in the WP frequencies, a simple regression analysis was conducted. Results show that the mean summer UHI will not change because increases and decreases of WPs with different associated UHI intensities will compensate each other. In this study only the changes of UHI of Hamburg (station St. Pauli) due to changes in the WP's frequency are considered. However, within-cluster changes of the WPs could be also responsible for a change in the target parameter (e.g. Fuentes and Heinmann, 2000). The within-cluster changes could be investigated by combining a WP and local variables from ERA40 or from the RCMs. Another important point for further studies is to investigate the possible occurrence of new WPs in a future climate. There are indications that rare weather situations might become more important in the future and new distinct WPs may form (Kreienkamp et al., 2010). In the present study no additional WP were assumed.

5 Statistical-dynamical downscaling for the urban heat island

5.1 Introduction

The horizontal resolution of current regional climate projections is in the range of 10-25 km. For Germany, the highest horizontal resolution of current climate projections is about 10 km (Jacob et al., 2008). To resolve small-scale urban climate effects such as the urban heat island (UHI) or the urban impact on precipitation (Schlünzen et al., 2010), a finer resolution is needed. For the development of climate adaptation strategies for urban areas, characterizing the UHI is important because its magnitude (up to 10 K; Yow, 2007) can be much higher than the projected temperature changes due to climate change (2-3 K for Northern Germany at the end of the 21st century; Daschkeit, 2011). Hence, regional climate projections have to be further downscaled. Downscaling techniques can be subclassified into three main types: statistical, dynamical and statistical-dynamical downscaling. For statistical downscaling a statistical relationship between large-scale variables from a coarser model and the small scale variable needs to be established (Wilby and Wigley, 1997). Statistical downscaling has been successfully applied to investigate changes in the UHI intensity (Wilby, 2003; 2008; Hoffmann et al., 2011; Chapter 3 of this thesis). Using this technique, the spatial pattern of the UHI can hardly be obtained, in particular if there are only few observational sites available. This is a major drawback when planning climate adaptation measures for cities because spatial information is needed to plan specific adaptation and mitigation measures. Also the impact of such measures on the urban climate can hardly be quantified when using statistical downscaling techniques only. To dynamically downscale a current regional climate projection to a horizontal grid of about 1 km for a 30-year period, still too much computing time is needed. To overcome these disadvantages, statistical-dynamical downscaling (SDD) can be applied (Frey-Buness et al., 1995). The SDD method makes use of the ability of climate models to simulate the large-scale circulation better than small-scale processes and assumes that representative weather patterns (WP) for certain meteorological variables exist. High-resolution numerical model simulations are then to be performed for each WP. To achieve the climatological average of the meteorological variables of interest, the simulation results are statistically recombined using the frequency of the WPs. The change of this variable is then determined by the change in the frequency of these WPs.

SDD methods have been applied to variables such as temperature (Fuentes and Heimann, 2000), precipitation (Huebener and Kerschgens, 2007a,b), and wind speed (Pinto et al., 2010; Najac et al., 2011). For urban climate, a simple SDD method has been successfully applied by Früh et al. (2011a,b). The statistical part of their method is not based on WPs but on prescribed combinations of temperature, wind speed and relative humidity. These combinations are used as initial conditions to conduct idealized simulations with a mesoscale model. The simulation results are statistically recombined using the so-called cuboid method to downscale RCM results with respect to urban heat load in the Frankfurt am Main area. Due to the simple treatment of the flow conditions (only two wind directions) the temperature pattern might be unrealistic because the advection of the UHI is not considered correctly. Therefore, another, more accurate, method to identify relevant situations for the UHI has to be established.

Apart from the study of Früh et al. (2011a,b), numerical studies of the UHI usually focus on the simulation of idealized meteorological conditions (e.g. Atkinson, 2003) or on the simulation of days with anticyclonic conditions (e.g. Bohnenstengel et al., 2011; Flagg, 2010, Grawe et al., 2012 submitted). However, these are events seldom for most cities. It is also questionable whether only the maximum UHI is of interest, because it might occur at days where the UHI is less important. Hoffmann and Schlünzen (2012; Chapter 4 of this thesis) showed that high UHI values also occur for WPs other than those considered in previous studies. Hence, simulating only one day might not show a realistic UHI pattern. On the contrary, a weak UHI is usually unimportant for the development of mitigation measures to reduce heat stress because it is advectively driven. The simulation of these situations, therefore, only increases the amount of computing time. Thus, weather situations that are resulting in large UHI values have to be determined. For Hamburg's UHI, which was investigated by Schlünzen et al. (2010) using observations within the city, Hoffmann and Schlünzen (2012; Chapter 4 of this thesis) constructed a weather pattern classification (WPC) and obtained 7 WPs for the summer months. However, these WPs only account for a small part of the UHI variance. Hence, further information is needed to subdivide the WPs according to the strength of the UHI. The Najac et al. (2011) SDD method, which is used for the downscaling of wind speed, employes subdivided WPs according to the strength of the flow field to achieve accurate wind speed distributions. As comparable measure for the downscaling of the UHI the statistical model developed for Hamburg's UHI (Hoffmann et al., 2011; Chapter 3 of this thesis) is used. This statistical model is based on near ground observations of relative humidity, cloud cover and wind speed. The relevant days can then be determined by combining the WPC and the statistical model. These days are simulated with a mesoscale model. In the present study, the non-hydrostatic mesoscale model METRAS (Schlünzen, 1990; Lüpkes and Schlünzen, 1996) is employed with a highest resolution of 1 km.

The dynamical part of a SDD method can be conducted in two ways. The numerical simulations with a high-resolution model could be forced with RCM data directly (Fuentes and Heimann, 2000). Following this method, biases in the RCM are passed on to the high-resolution model. A bias correction is not possible because a three-dimensional observational dataset would have to be used to preserve the physical relationships between the atmospheric variables. These need to be fulfilled if the data are used to force a higher resolving model. The alternative approach is to detect the respective situations in the present climate and simulate these situations by forcing the model with observational data. Pinto et al. (2010) and Najac et al. (2011) used reanalysis data for this purpose. Due to the coarse resolution of these datasets (~115 km), several downscaling steps have to be conducted, thus increasing the computational effort. To avoid this, higher resolution (~25 km) analysis data (ECMWF, 2009; 2010) from the European Center for Medium-Range Forecast (ECMWF) can be used. A disadvantage is that these data are created using different model versions and are only available for recent years. However, they are assumed to be closer to reality than reanalysis data because they employ all the remote sensing data available.

When simulating the UHI with a numerical model the surface characteristics of urban areas have to be characterized and their effects parameterized (Schlünzen et al., 2011). Sophisticated urban canopy layer parameterizations such as the town energy budget (TEB; Masson, 2000) or the building energy parameterization (BEP; Martilli et al., 2002) need information about the city structure such as street width and directions or building heights. These data were not available for this study. Nevertheless, due to the availability of high-resolution land-use datasets new surface cover classes are developed for METRAS (Flagg et al., 2011). These new classes allow for a more detailed treatment of urban surfaces (e.g. separation of buildings and backyards) and are used to perform the 1km simulations for this study.

The aim of this chapter is to construct and apply a WPC based SDD method to downscale regional climate projections to a final resolution of 1 km using Hamburg's UHI as a test case. In the following the SDD method will be described in detail (Section 5.2). The setup of the dynamical simulations will be presented in Section 5.3. In Section 5.4 these simulations will be evaluated with observational data. The results of the downscaling methods for current and future climate will be presented in Section 5.5. Concluding remarks are given in Section 5.6.

5.2 Methodology

The statistical-dynamical downscaling method is described in Section 5.2.1. Section 5.2.2 deals with the regional climate model data used for the downscaling.

5.2.1 Statistical-dynamical downscaling method

The SDD method applied in this study is schematically presented in Figure 5.1. The objective weather pattern classification is described in detail in Chapter 4 of this thesis. For each season weather patterns (WP) were determined that represent the variability of the UHI of Hamburg. The WPs are constructed by clustering 700 hPa fields from the ERA40-reanalysis (Uppala et al., 2005) with the *k*-means-based SANDRA method (Philipp et al., 2007). The UHI variance explained by the WPs is, however, not large enough to just simulate the days which are closest to cluster centers. This is mainly due to the low number of WPs. Usually, the number of WPs used for SDD methods is higher, e.g. 22 as used by Fuentes and Heimann (2000) or 55 as used by Pinto et al. (2010). However, a larger number of WPs would result in a large uncertainty when determining them in results of different RCMs, since the WPs are not well enough separated from each other. Therefore, an approach similar to Najac et al. (2011) is followed. They simulated several days within one WP, which in there case were based on 850 hPa *u*- and *v*- wind components. The WPs were subdivided according to the strength of the 850 hPa wind field. Instead of taking the strength of a certain classification variable, an estimate for the strength of the UHI within each WP is used in this study. Since this estimate has to be calculated for both the current and the future climate, the observed UHI cannot be used. Instead a statistical model for the UHI, similar to that used in Hoffmann et al. (2011; Chapter 3 of this thesis), is constructed. Using multiple linear regression (Eq. 5.1), the UHI is described as a linear function of wind speed *FF*, cloud cover *CC*, and relative humidity *RH*.

$$\Delta T_{u-r} = a\,FF + b\,CC + c\,RH + d \qquad (5.1)$$

ΔT_{u-r} denotes Hamburg's UHI, described as the difference of the daily minimum temperature measured at the urban German Meteorological Service (DWD) station Hamburg-St. Pauli and the average of the minimum temperatures observed at the rural DWD stations Grambek (GR) and Ahrensburg (AH). Since most stations used in Hoffmann et al. (2011; Chapter 3 of this thesis) did not perform continuous measurements during the period of 1971-2010, data for the model variables (*FF*, *CC*, *RH*) are taken from the DWD climate reference station Hamburg-Fuhlsbüttel (FU).

The statistical model parameters *a*, *b*, *c*, and *d* are computed for each WP separately. Therefore, different statistical relationships among the WPs are allowed. This combination of the WPC and statistical model explains about 50% of the UHI variance with a root mean square error of about 1.2 K.

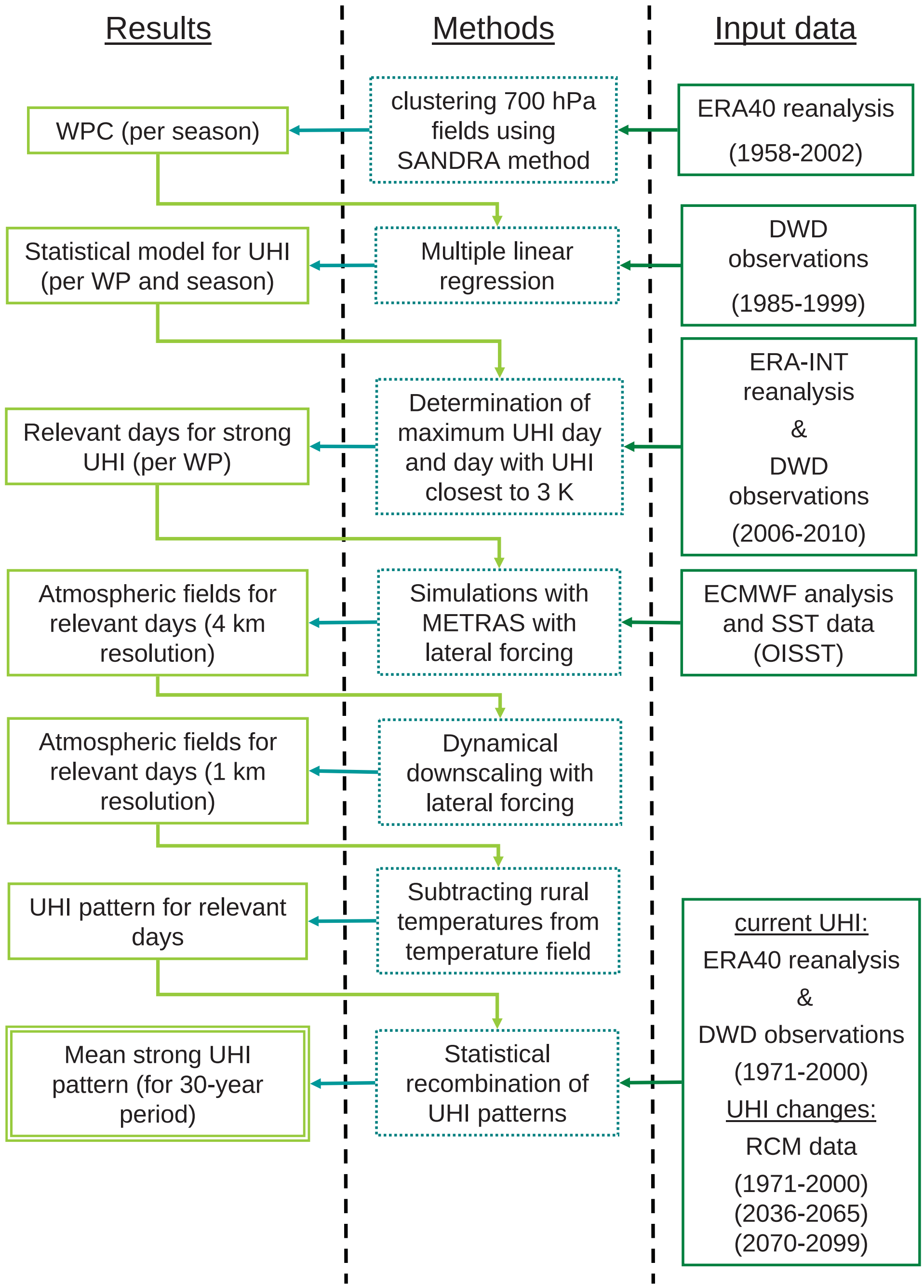

Figure 5.1: *Schematic diagram of the statistical-dynamical downscaling method for Hamburg's UHI. Results are indicated by light green boxes, methods by turquoise boxes, and the input data by dark green boxes.*

By combining the WPC with the statistically modeled ΔT_{u-r} the relevant days for the UHI can be determined. Before doing this the term "relevant day" has to be defined. Since only days with a strong UHI are of interest for planning climate adaptation measures, simulation of weak UHI days would only lead to an unnecessary increase in computational costs. Therefore, a threshold UHI intensity $(\Delta T_{u-r})_{Thres}$ is introduced. All days with $\Delta T_{u-r} \geq (\Delta T_{u-r})_{Thres}$ are then considered as strong UHI days. In this study, $(\Delta T_{u-r})_{Thres} = 3$ K is chosen. This means that the result of the SDD method shall lead to an average strong UHI pattern instead of an average UHI pattern. The relevant days, which should be simulated for each WP are the day with ΔT_{u-r} closest to $(\Delta T_{u-r})_{Thres}$ and the day with the maximum ΔT_{u-r}.

Using this definition, the relevant days in the period from 1985-1999 were determined using the ERA40 reanalysis. However, to downscale from a horizontal resolution of ~115 km down to 1 km at least a 4 step nesting is needed (e.g. 48 km, 12 km, 4 km, and 1 km) when using a refinement factor of 4. The numerical model METRAS is not designed for horizontal resolutions larger than ~20 km (Schlünzen et al., 2012a). Therefore, an intermediate model would be needed to simulate the outer domain (Huebener and Kerschgens, 2007a,b). To avoid this step high resolution analysis fields from the ECMWF are used as forcing. The ECMWF data and the forcing technique are explained in detail in Section 5.3.3 and Section 5.3.4, respectively. The analysis data are available on a resolution of ~25 km starting in 2006, leaving the period 2006-2010 to determine the relevant days. During that period, neither observations of the UHI nor ERA40 based WP data are available. To extend the ERA40 based WP time series, the WPs are determined for the ERA-Interim (ERA-INT) dataset (Dee et al., 2011). ERA-INT is an improved and frequently updated atmospheric reanalysis dataset starting in 1989. An investigation of the WP time series of both datasets for the overlapping period 1989-2001 showed that they are identical for more than 99% of the days. The values for the ΔT_{u-r} values are calculated with the statistical model (Eq. 5.1). The selected relevant days and their corresponding simulation names are listed in Table 5.1. For WP7 both $(\Delta T_{u-r})_{Thres}$ and $(\Delta T_{u-r})_{\max}$ are equal resulting in only one simulation for this WP. Except for WP1, WP3, and WP6 the difference between $(\Delta T_{u-r})_{Thres}$ and $(\Delta T_{u-r})_{\max}$ is lower than the *RMSE* (1.2 K) of the WPC/statistical model combination.

The determined days are then simulated with METRAS using a two step nesting (4 km and 1 km). The simulations are conducted for 71 hours in total. They start for 7 p.m. local sun time (LST) on the first day and end 6 p.m. LST on the fourth day. The night of interest is the night from day 3 to day 4. The long spin-up time is chosen so that an UHI can develop, which is only weakly affected by the initial conditions. Warming and cooling processes of the soil and the near ground air temperatures can be simulated more independently of the initial conditions. Details about the model and the simulations are given in Section 5.3.

To calculate the average UHI, the simulation results obtained with METRAS 1 km, have to be recombined statistically. As a first step, the UHI has to be determined in the numerical results. Following Hoffmann et al. (2011; Chapter 3 of this thesis) and Hoffmann and Schlünzen (2012; Chapter 4 of this thesis), the UHI is determined by subtracting the averaged temperatures of the rural DWD stations Grambek and Ahrensburg from the total temperature field. In the model, the grid points closest to the rural stations are used. Instead of using the minimum temperatures, averaged nighttime temperatures are used.

Table 5.1: *List of relevant days and their corresponding statistically modeled UHI values* ΔT_{u-r}. *The number within the simulation names denotes the WP number, while the ending denotes maximum UHI day (M) or the day with an UHI closest to the threshold UHI (T).*

Simulation name	**Date**	ΔT_{u-r} **(K)**
WP1M	17-Jun-2007	4.6
WP1T	22-Jun-2009	3.0
WP2M	09-Jul-2007	3.3
WP2T	19-Aug-2007	3.0
WP3M	05-Jul-2006	5.7
WP3T	01-Jul-2009	3.0
WP4M	01-Aug-2009	4.0
WP4T	18-Jul-2009	3.0
WP5M	17-Aug-2008	4.1
WP5T	18-Jun-2008	3.0
WP6M	11-Jun-2007	5.2
WP6T	17-Jul-2009	3.1
WP7M	06-Jun-2009	3.2

The UHI pattern of each simulation contributes to the averaged strong UHI with a specific weight. This weight is based on the frequency of occurrence of the corresponding WP. Furthermore, the actual UHI is calculated by using the statistical model (Eq. 5.1) for a given day. The numerical model results for maximum UHI $(\Delta T_{u-r})_{\max}$ and the threshold UHI $(\Delta T_{u-r})_{Thres}$ within each WP are linearly interpolated to receive the pattern corresponding UHI. This means that the UHI pattern of a given day with a given $\Delta T_{u-r} \geq 3\,\mathrm{K}$ is a linear combination of the two UHI patterns UHI($(\Delta T_{u-r})_{\max}$) and UHI($(\Delta T_{u-r})_{Thres}$), which are obtained for each WP. The weights for the *k*th WP are calculated using the frequency of strong UHI days N_{strong} for the corresponding WP (Eq. 5.2). The difference between the maximum UHI $(\Delta T_{u-r})_{\max}$ and the threshold UHI $(\Delta T_{u-r})_{Thres}$, which is denoted as R_{strong} (Eq. 5.3) is also calculated per WP.

$$N_{strong}(k) = \sum_{\Delta T_{u-r} \in WP(k)} \begin{cases} 1 \text{ if } \Delta T_{u-r} \geq 3\text{ K} \\ 0 \text{ if } \Delta T_{u-r} < 3\text{ K} \end{cases} \tag{5.2}$$

$$R_{strong}(k) = (\Delta T_{u-r})_{\max}(k) - (\Delta T_{u-r})_{Thres}(k) \tag{5.3}$$

The absolute differences between all strong UHIs and the $(\Delta T_{u-r})_{\max}$ as well as between strong UHI days and $(\Delta T_{u-r})_{Thres}$ normalized by R_{strong} are summed up for each WP. These sums are than divided by N_{strong} to yield the averaged nondimensional differences $Diff_{\max}$ (Eq. 5.4) and $Diff_{Thres}$ (Eq. 5.5).

$$Diff_{\max}(k) = \left(\sum_{\Delta T_{u-r} \geq 3\,K \in WP(k)} \frac{(\Delta T_{u-r} - (\Delta T_{u-r})_{thres}(k))}{R_{strong}(k)} \right) \cdot (N_{strong}(k))^{-1} \tag{5.4}$$

$$Diff_{Thres}(k) = \left(\sum_{\Delta T_{u-r} \geq 3\,K \in WP(k)} \frac{((\Delta T_{u-r})_{\max}(k) - \Delta T_{u-r})}{R_{strong}(k)} \right) \cdot (N_{strong}(k))^{-1} \tag{5.5}$$

These averaged differences represent the weights of both simulations within each WP. The final weights $W_{\max}$ and W_{Thres} are calculated by multiplying Eq. (5.4) and Eq. (5.5) with the corresponding relative frequency of N_{strong}.

$$W_{\max}(k) = Diff_{\max}(k) \cdot \frac{N_{strong}(k)}{\sum_{i=1}^{K} N_{strong}(i)} \tag{5.6}$$

$$W_{Thres}(k) = Diff_{Thres}(k) \cdot \frac{N_{strong}(k)}{\sum_{k=1}^{K} N_{strong}(i)} \tag{5.7}$$

Days with $\Delta T_{u-r} > (\Delta T_{u-r})_{\max}$ are treated as days with a $\Delta T_{u-r} = (\Delta T_{u-r})_{\max}$ since an extrapolation of the pattern is not possible. This case can occur because $(\Delta T_{u-r})_{\max}$ is only determined in the period 2006-2010 and because larger values of ΔT_{u-r} could occur in the future climate projections. Thus, UHI changes from current to future climate might be slightly underestimated.

The statistically recombined UHI pattern is computed by multiplying $W_{\max}$ and W_{Thres} with the corresponding simulated UHI patterns and summing up the resulting patterns. For the current climate (1971-2000), the weights are calculated from the WPs based on the ERA40 data and the statistically modeled UHI values computed with DWD observations from Hamburg-Fuhlsbüttel. To determine changes in the UHI pattern due to climate change, the weights are calculated for the different RCM results, described in Section 5.2.2. The focus of this study is on the changes between the current climate (1971-2000) and the future climate (2036-2065 and 2070-2099). Using the introduced SDD method, the average strong UHI pattern can change due to frequency changes of the WPs as well as due to changes in the distribution of statistically modeled strong UHI values within the corresponding WP.

5.2.2 Regional climate model data

As used by Hoffmann et al. (2011; Chapter 3 of this thesis) and Hoffmann and Schlünzen (2012; Chapter 4 of this thesis) data from the regional climate simulations conducted with CLM (Hollweg et al., 2008) and REMO (Jacob et al., 2008) are used as input for the downscaling. Both RCMs are driven with the SRES A1B projections from ECHAM5-MPIOM (Roeckner et al., 2003, Jungclaus et al., 2006). The REMO simulations are conducted applying a two step nesting. Since the domain with the finest grid is smaller than the domain used for the WPC, the WPs are determined from the coarser simulations (~50 km). The variables for the statistical model are determined from the high-resolution simulations (~10 km). Schoetter et al. (2012) evaluated the CLM and REMO results for the metropolitan area of Hamburg and showed that both RMCs have considerable biases in variables that are used in the statistical model for the present climate. These biases also lead to biases in the statistically modeled UHI (Hoffmann et al., 2011; Chapter 3 of this thesis). Therefore, the RCM data are biases-corrected following Schoetter et al. (2012), by applying a quantile-mapping method similar to Piani et al. (2010). A problem appearing when using the bias-correction for the SDD method is that the local variables, and therefore the statistically modeled UHI, might not be consistent with the WPs after the bias correction. In future studies, this bias-correction should be done for each WP separately. Hoffmann and Schlünzen (2012; Chapter 4 of this thesis) also showed that there are biases in the frequency of the WPs in the RCM results. A bias correction method for the daily atmospheric patterns is, however, not yet available. Only the WP frequencies could be bias-corrected as suggested by Demuzere et al. (2009). This is not applicable for the SDD method as the calculation of the weights (Eq. 5.6 and Eq. 5.7) of the WPs and the statistically modeled UHI depend on each other.

To increase the ensemble size of RCM results, data from regional climate simulations performed with the Conformal Cubic Atmospheric Model (CCAM; McGregor, 2005; McGregor and Dix, 2008) are also used. CCAM is a hydrostatic global model with a non-uniform grid, which is used as a RCM (horizontal resolution ~60 km). A list of parameterizations used in CCAM is given in Table 5.2. In contrast to CLM and REMO, CCAM is driven by the SRES A2 simulations conducted with the GFDLcm2.0 (Delworth et al., 2006). Instead of using lateral atmospheric forcing CCAM is driven by the monthly mean sea surface temperatures (SST) and sea ice concentrations provided by GFDLcm2.0. To reduce the transfer of GCM-deficiencies to the CCAM simulations, the SSTs are preliminary bias-corrected by calculating the climatological monthly means for the respective period and computing the bias against a SST climatology provided by National Oceanic and Atmospheric Administration (NOAA) (Reynolds, 1988) for the same period. The corresponding monthly bias is then subtracted from each month of the SST time series used for forcing CCAM (Katzfey et al., 2009). In addition to the SST forcing, the specified equivalent CO_2, ozone, and direct aerosol effects for the A2 scenario are also used to conduct the simulations.

Table 5.2: *List of parameterization schemes used for the CCAM simulations (Katzfey, 2011 personal communication).*

Parameterization	Reference
Explicit Cloud Scheme	Rotstayn (1997)
Convection	McGregor (2003)
Land Surface	Kowalczyk et al. (1994)
Boundary Layer	McGregor (2003) stability dependent scheme with non-local vertical mixing based on Holtslag and Boville (1993) and enhanced mixing of cloudy boundary layer air based on Smith (1990)
Gravity Wave Drag	Chouinard et al. (1986)
Radiation	Short wave: Lacis and Hansen (1974) Long wave: Schwarzkopf and Fels (1991)

5.3 Mesoscale model setup

The relevant days determined in Section 5.2.1 are simulated with the mesoscale numerical model METRAS using a two-step nesting The simulations are forced with ECMWF analysis fields as well as sea surface temperatures (SST) from NOAA. In the following, the model specification (Section 5.3.1) and the model domain (Section 5.3.2) are described. A description of the forcing data and forcing method is given in Section 5.3.3 and 5.3.4, respectively.

5.3.1 METRAS

The mesoscale transport and fluid model METRAS (Schlünzen, 1990; Lüpkes and Schlünzen, 1996) is a three-dimensional non-hydrostatic mesoscale numerical atmospheric model. It has been previously applied to Germany (Schlünzen, 1992; Renner and Münzenberg, 2003; Schlünzen and Katzfey, 2003; Schüler and Schlünzen, 2006; Schlünzen and Meyer, 2007; Bohnenstengel, 2011, Buschbom et al., 2012), Spain (Augustin et al., 2008), China (Wu and Schlünzen, 1992; Sheng et al., 2000), coastal areas (Niemeier and Schlünzen, 1993), the Arctic (Dierer and Schlünzen, 2005; Hebbinghaus et al., 2007; Lüpkes et al., 2008; Ries et al., 2010), and the urban climate of London (Thompson, 2008; Grawe et al., 2012 submitted) with horizontal resolutions ranging from 1 km to 18 km. A detailed description of METRAS is given in Schlünzen et al. (2012a). The dynamic equations solved in METRAS are based on the anelastic and Boussinesque approximated primitive equations, resulting in prognostic equations for the three wind-components u, v and w, temperature and specific humidity. Microphysical processes are parameterized with the Kessler scheme (Kessler, 1969), resulting in prognostic equations for cloud water and rain water. The radiation parameterization is dependent on the existence of liquid water in the model domain. In cloud free situations the longwave and shortwave radiation balance is computed only at the surface. In the atmosphere a constant cooling rate is assumed (2 K/day at daytime and 3 K/day at nighttime). With clouds in the model domain, radiation fluxes at the surface as well as the atmosphere are determined with a two-stream approximation scheme.

For the calculation of sub-grid scale turbulent fluxes in the surface layer ($z \leq$ 10 m) the surface layer similarity theory is employed. Accordingly, the vertical exchange coefficient for momentum K_{vert} and for scalar quantities (heat and humidity) $K_{vert,S}$ are calculated with:

$$K_{vert} = \kappa u_* z / \Phi_m (z / L) \tag{5.8}$$

$$K_{vert,S} = \kappa u_* z / \Phi_h (z / L) \tag{5.9}$$

Here z is the height above ground, u_* is the friction velocity, κ is the von Karman constant ($\kappa = 0.4$), and Φ_m and Φ_h are the stability functions which depend on the Monin-Obukhov length L. METRAS considers sub-grid scale land-use (surface cover). For different fractions of land-use within a grid cell the flux averaging method is applied. It is implemented using the blending height concept (Claussen, 1991; Hermann, 1994; von Salzen et al., 1996). The different surface cover and land-use classes are described in Section 5.3.2. For the water surface classes, the roughness length is a function of wind speed and in particular of the friction velocity (Charnock, 1955).

The vertical turbulent fluxes above the surface in the stable and neutrally stratified boundary layer are parameterized using a mixing length scheme based on Herbert and Kramm (1985). In this scheme, *z/L* is replaced by the local Richardson number *Ri* in the stability functions. The resulting equations are:

$$K_{vert} = \begin{cases} l_n^2 \left|\frac{\partial v}{\partial z}\right| (1-5Ri)^2 & 0 \le Ri \le 0.15 \\ l_n^2 \left|\frac{\partial v}{\partial z}\right| (1-16Ri)^{1/2} & -2 \le Ri \le 0 \end{cases} \tag{5.10}$$

$$K_{vert,S} = \begin{cases} K_{vert} & 0 \le Ri \le 0.15 \\ K_{vert}(1-16Ri)^{1/4} & -2 \le Ri \le 0 \end{cases} \tag{5.11}$$

The mixing length for the neutral stratification l_n is calculated according to Blackadar (1962):

$$l_n = \frac{\kappa z}{1 + \frac{\kappa z}{0.007 u_* f}} \tag{5.12}$$

Here f denotes the Coriolis parameter. The formulation (5.11) and the limits for *Ri* are chosen to assure the matching of the fluxes at the lowermost model level with the fluxes above. In addition, the upper limit of the so called critical Richardson number is restricted to 0.15 to account for additional diffusion due to sub-grid scale gravity waves. This value was determined in this thesis by conducting sensitivity studies with different *Ri* values ranging from 0.1 to 0.1666 (maximum values to fulfill continuity of fluxes). For $Ri = 0.15$ waves resulting from gravity waves by non-linear wave interaction are damped. They occur in the nighttime near the surface in the temperature field when surface cooling is intense. Tuning the critical *Ri* might not seem physical, however, the correct value for the critical Richardson number is still an ongoing research topic (Zilitinkevich et al., 2007; Grachev et al.; 2012). Another way to account for sub-grid scale gravity waves would be to parameterize them (e.g. Zilitinkevich, 2002; Nappo et al., 2004). This is not done in the present study, because a comprehensive sensitivity study would have to be carried out to test if these parameterizations can be used with the turbulence parameterization employed in METRAS.

For unstable and convective stratification the non-local countergradient scheme is used (Lüpkes and Schlünzen, 1996) allowing mixing of momentum, heat and moisture counter the local gradient.

To calculate the surface temperatures T_S, the force-restore method by Deardorff (1978) is applied. The equation for the surface temperature tendency can be written as:

$$\frac{\partial T_S}{\partial t} = \frac{2\sqrt{\pi}k_S}{\nu_S}\left\{\mu \cdot I_\infty \cos(Z(t)) - \hat{\varepsilon}\sigma \overline{T_S}^4 + c_p \rho_0 u_* \theta_* + l_{21}\rho_0 u_* q_* - \sqrt{\pi}\nu_S \frac{\overline{T}_s - \overline{T}_s(-h_\theta)}{h_\theta}\right\} \tag{5.13}$$

The first two terms on the right-hand side correspond to the shortwave and longwave radiation budget at the surface and are given here for the cloud free case. The shortwave radiation budget depends on the cosine of the zenith angle Z(t), which is multiplied by the solar constant I_∞ = 1370 W/m² and the parameter μ. This parameter depends on the Albedo a_0 and can be estimated for northern Germany by 0.75·(1-a_0) for a cloud free domains. The longwave radiation budget is calculated using the Stefan-Boltzmann law, where σ denotes the Stefan-Boltzmann constant ($5.67 \cdot 10^{-8}$ W/m^{2}K^4). The parameter $\hat{\varepsilon}$ accounts for the emissivity of the surface as well as for the incoming longwave radiation and is set to be 0.22 for a cloud free domain. For cloudy situations both radiation terms are calculated with the radiation parameterization.

Term three in Eq. (5.13) accounts for the temperature change due to the sensible heat flux, which depends on the heat capacity c_p, density of the air ρ_0 and the turbulent heat flux $u_*\theta_*$, where θ_* denotes the scaling temperature.

The fourth term corresponds to the temperature change due to the latent heat flux, which depends on the enthalpy of vaporization l_{21} and the turbulent humidity flux, where q_* denotes the scaling value for specific humidity. The last term on the right hand side reflects the soil energy balance, i.e. heat release or heat storage depending on the soil and surface cover characteristics. They specifically depend on the depth of the daily temperature wave h_θ and thermal conductivity of the soil and surface cover type ν_S. Since each simulation conducted in this study is done for a 3 day period the deep soil temperature $\overline{T}_s(-h_\theta)$ is kept constant at its initial value.

For the specific humidity at the surface $\overline{q}_{1s}^1$ a simple budget equation is applied (Deardorff, 1978):

$$\overline{q}_{1s}^1 = \alpha_q \overline{q}_{1sat}^1(\overline{T}_S) + (1-\alpha_q)\overline{q}_1^1 \tag{5.14}$$

Here α_q is the bulk soil water availability, which depends on the turbulent humidity flux, precipitation, and the saturated soil and surface cover moisture availability W_K as given for each surface cover type.

In the METRAS version applied, no additional urban canopy parameterization is implemented as done by Thompson (2008). Therefore, the influence of buildings on the radiation (e.g. shading and radiative trapping) as well as on the flow field in higher model levels is not considered. Furthermore, the anthropogenic heat release is neglected. Hence, only urban effects due to the different surface characteristics such as heat storage, water availability, evaporation characteristics, and roughness are simulated. A detailed description of the surface characteristics as used in the present study is given in Section 5.2.2.

The equations are numerically solved on an Arakawa-C-grid (Mesinger and Arakawa, 1976), where the wind components (u, v, and w) are shifted by half a grid point compared to the grid points of scalar quantities. For the advection terms in the momentum equation are discretized using centered differences and integrated using the Adam-Bashforth scheme. To avoid nonlinear instabilities of the model equations a 7 point filter is applied to the wind components in the horizontal directions. This method also results in horizontal diffusion of the wind. Depending on the allowed time-step the vertical exchange processes are either solved with the Adam-Bashforth scheme or with the Crank-Nicholson scheme. Temperature and humidity equations are solved using the upstream scheme for the advection terms. The exchange processes are solved forward in time and centered in space in horizontal direction. Depending on the model time-step, the Crank-Nicholson-Scheme is also applied.

5.3.2 Model domains and surface cover

The downscaling simulations are conducted by forcing a 4 km simulation horizontal resolution with ECMWF data and using these results to force a simulation with 1 km horizontal resolution. The boundaries of both domains are shown in Figure 5.2. The outer domain has a dimension of 175 x 156 grid cells (700 km x 624 km) covering northern Germany, and parts of Denmark, the Netherlands, Sweden and Poland. The dimension of the inner domain is 194 x 191 grids cells (194 km x 191 km) and it covers the metropolitan area of Hamburg including parts of the North Sea and Baltic Sea. The vertical grid of both domains is in terrain following coordinates, has a similar vertical spacing and consists of 34 levels.

The lowest atmospheric grid cell is 10 m above ground at sea level and slightly lower above orography due to the terrain following grid. The grid spacing is 20 m up to a height of 90 m above ground. Above that level, the grid spacing increases with a constant stretching factor of 1.15. The top of both domains is at 12511 m.

To construct surface cover and land-use (lower boundary condition for METRAS), land-use data from different sources are used, ranging from ATKIS data to a detailed biotope dataset for the state of Hamburg. They are combined into 10 land-use classes for the 4 km grid including one urban land-use class. The surface parameters for these classes are given in Table 5.3. The dominant land-use class per grid cell is shown in Figure 5.3. For the 1 km simulation a set of 36 surface cover classes is used, hereafter denoted METRAS-36. Flagg et al. (2011) comprehensively investigated urban land-use types, such as "Blockrandbebauung", and determined the fraction of buildings and the surrounding surface cover such as grass or brick. These fractions are assigned to corresponding land use classes. Buildings are divided into two separate building classes, namely high buildings and low buildings. The roughness length of these classes is determined using the bluff body approximation. The parameters for the different surface cover types are given in Table 5.4. Details on the attribution of the parameter values are given in Schlünzen et al. (2012b).

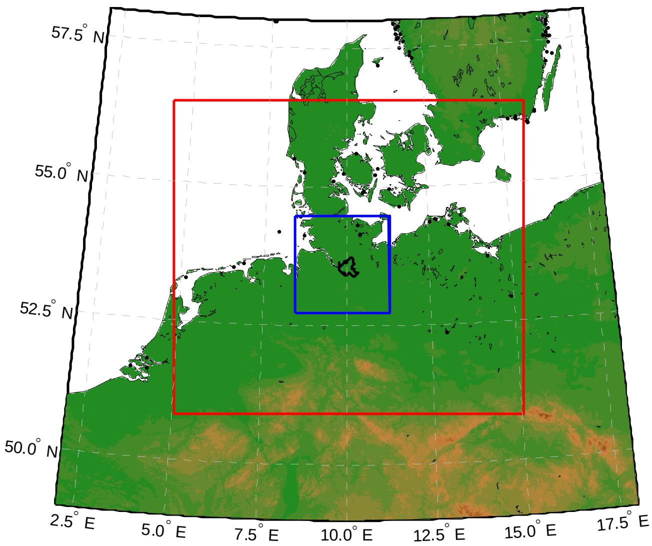

Figure 5.2: *Map indicating the boundaries of the 4 km domain (red) and 1 km domain (blue).*

To determine the influence of the new surface cover classes on the downscaling results, all simulations are conducted twice, once with a 1 km grid that contains 10 land-use classes only, herein denoted as METRAS-10 and once with METRAS-36. Figure 5.4a shows the fraction of buildings and adjacent surfaces, which include the surface cover classes: high buildings, low buildings, asphalt, brick and steel. Here, the sealing gradient of Hamburg is well visible. In addition, it shows that even in downtown Hamburg, the sealed fraction is below 100%. Using only 10 land-use classes the urbanization gradient is not that well visible (Figure 5.4b) because the urban class also includes - besides sealed surfaces - other urban land-uses like play-grounds or backyard gardens. The urban fraction is much larger for Hamburg as well as for other cities than the sealed portion of Figure 5.4a. This might result in a larger UHI magnitude.

Table 5.3: *Surface characteristics for the METRAS-10 land-use types with Albedo α_0, thermal diffusivity k_s, thermal conductivity ν_S, soil water availability (initial values) α_q, saturation value or water content W_K, and roughness length z_0.*

Land-use type	α_0	k_s [m^2/s]	ν_S [W/mK]	α_q	W_K [m]	z_0 [m]
water	0.10	1.5E-07	100.00	0.98	100.000	f(u_*)
mudflats	0.10	7.4E-07	2.20	0.98	0.322	0.0004
sand	0.20	5.7E-07	1.05	0.10	0.026	0.0012
mixed land use	0.20	5.2E-07	1.33	0.20	0.138	0.0400
meadows	0.20	5.2E-07	1.33	0.40	0.015	0.0200
heath	0.15	2.4E-07	0.30	0.10	0.423	0.0500
bushes	0.20	5.2E-07	1.33	0.30	0.081	0.1000
mixed forest	0.15	8.0E-07	2.16	0.30	0.121	0.0050
coniferous forest	0.10	8.0E-07	2.16	0.30	0.161	1.2000
urban area	0.15	14.0E-07	2.93	0.05	0.968	0.7000

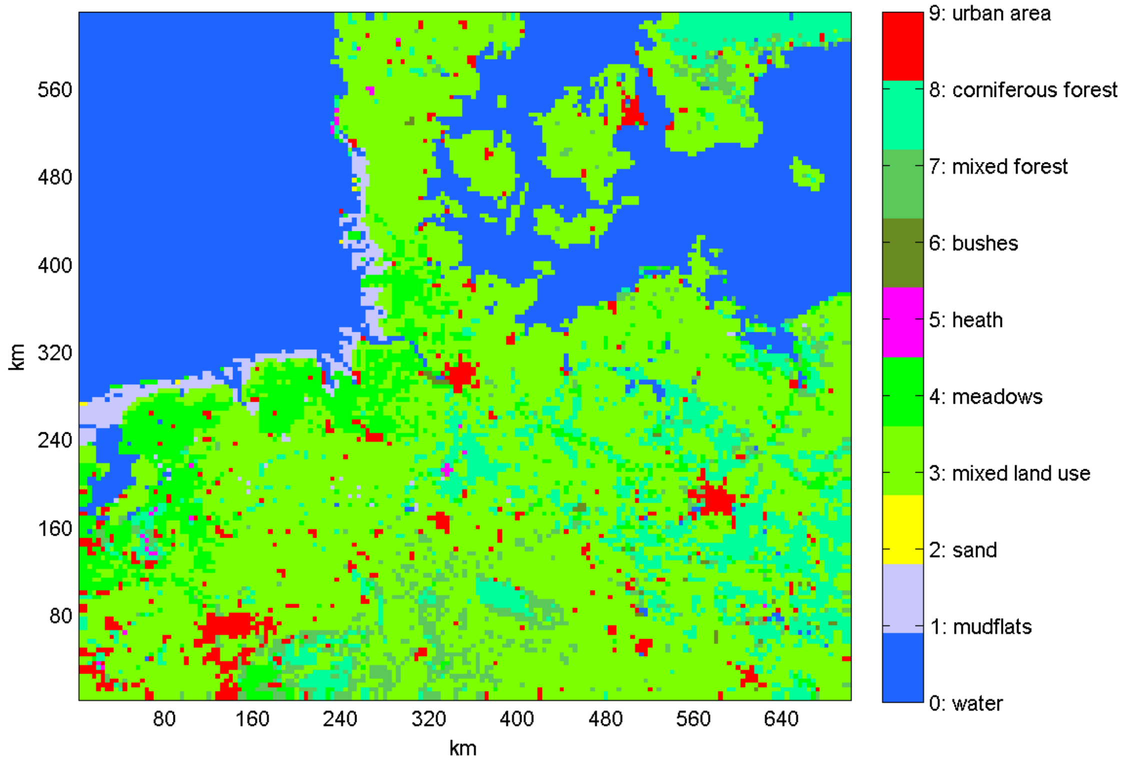

Figure 5.3: *Map of the dominant land-use class of the 4 km domain.*

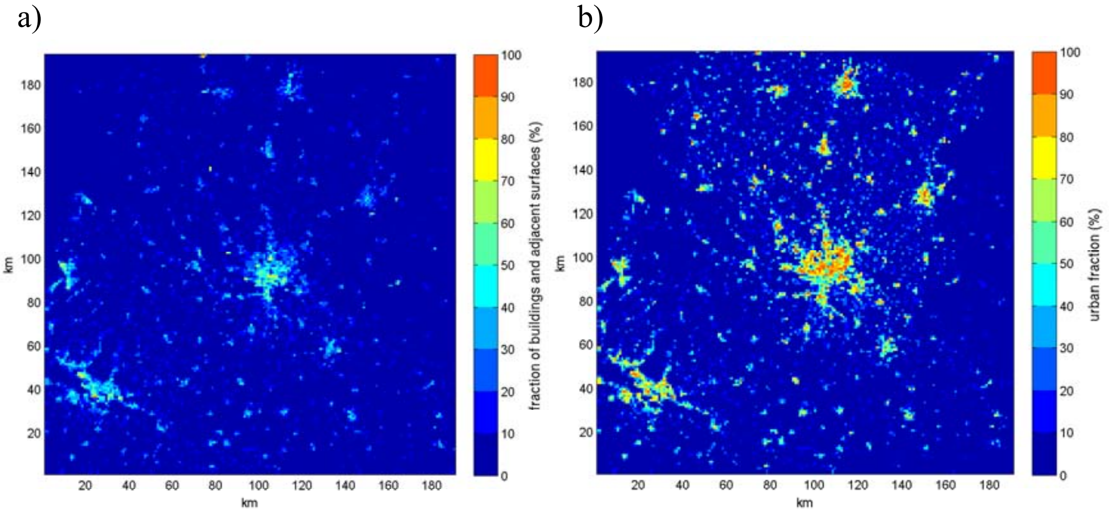

Figure 5.4: *(a) Fraction of buildings plus adjacent sealed surfaces as a sum of surface cover classes: high buildings, low buildings, asphalt, brick, and steel from METRAS-36 data. (b) Fraction of the urban class from METRAS-10.*

Table 5.4: *Surface characteristics for the 36 surface cover types with Albedo α_0, thermal diffusivity k_s, thermal conductivity v_S, soil water availability (initial values) α_q, saturation value for water content W_K, and roughness length z_0.*

Surface cover type	α_0	k_s [m^2/s]	v_S [W/mK]	α_q	W_K [m]	z_0 [m]
water	0.10	1.50E-07	100.00	0.98	100.000	f(u_*)
stationary fresh water	0.10	1.50E-07	100.00	1.00	100.000	f(u_*)
dynamic fresh water	0.10	1.50E-07	100.00	1.00	100.000	f(u_*)
salt water	0.10	1.50E-07	100.00	0.98	100.000	f(u_*)
mudflats	0.10	7.40E-07	2.20	0.98	100.000	0.0002
bare ground	0.17	3.80E-07	1.18	0.30	0.015	0.0012
sand	0.20	5.70E-07	1.05	0.10	0.010	0.0003
gravel	0.12	2.76E-07	0.40	0.10	0.010	0.0050
sand dune with grass	0.20	5.70E-07	1.05	0.15	0.035	0.0100
and dune with sparse vegetation	0.20	5.70E-07	1.05	0.15	0.045	0.0500
asphalt	0.09	2.30E-06	1.35	0.50	0.002	0.0003
brick/pavers	0.30	2.30E-06	0.90	0.02	100.000	0.0006
steel	0.30	4.20E-06	30.00	0.50	0.001	0.0003
wet bushes	0.20	5.20E-07	1.33	0.65	100.000	0.1000
wet bare ground	0.17	7.40E-07	2.20	0.60	100.000	0.0012
short dry grass	0.20	5.20E-07	1.33	0.35	0.050	0.0100
short wet grass	0.20	5.20E-07	1.33	0.55	100.000	0.0100
long dry grass	0.20	5.20E-07	1.33	0.35	0.070	0.0200
long wet grass	0.20	5.20E-07	1.33	0.55	100.000	0.0200
cropland	0.20	5.20E-07	1.33	0.40	0.060	0.0400
irrigated cropland	0.20	5.20E-07	1.33	0.65	100.000	0.0400
cropland with sandy soil	0.20	5.20E-07	1.33	0.35	0.040	0.0400
heath	0.15	5.70E-07	1.05	0.15	0.423	0.0500
heath on sandy soil	0.15	5.70E-07	1.05	0.15	0.100	0.0500
dry bushes	0.20	5.20E-07	1.33	0.15	0.060	0.1000
short bushes	0.20	5.20E-07	1.33	0.35	0.090	0.1000
deciduous forest	0.17	8.00E-07	2.16	0.60	0.120	1.0000
coniferous forest	0.10	8.00E-07	2.16	0.50	0.160	1.0000
wet coniferous forest	0.10	8.00E-07	2.16	0.70	100.000	1.0000
mixed forest	0.15	8.00E-07	2.16	0.45	0.120	1.0000
dry mixed forest	0.15	8.00E-07	2.16	0.50	0.050	1.0000
wet mixed forest	0.15	8.00E-07	2.16	0.50	100.000	1.0000
forest and bushes	0.20	6.50E-07	1.75	0.20	0.100	0.2500
low buildings	0.18	14.0E-07	2.61	0.50	0.002	0.6000
high buildings	0.18	23.0E-07	3.44	0.50	0.002	1.2000
mixed landuse	0.20	5.20E-07	1.33	0.20	0.100	0.10000

5.3.3 Forcing data

To simulate a selected meteorological situation METRAS has to be forced with observational data or model results of coarser resolution. Analysis data provided by the ECMWF (ECMWF, 2009; 2010) are well useable for the atmospheric part of the forcing (Ries et al., 2010). ECMWF-analyses are available every six hours (00 UTC, 06 UTC, 12 UTC, and 18 UTC). The horizontal resolution varies according to the resolution of the actual ECMWF forecast model. From 2006 until January 2010 the resolution is T799L91, which corresponds to a horizontal resolution of ~25 km and 91 vertical levels. The model levels use terrain following pressure coordinates. The resolution increased to T1279L91 (~16 km) starting end of January 2010. Hence, simulations for 2010 have finer forcing data than the rest of the simulations. Forced variables are air temperature, horizontal wind components, and specific humidity. Liquid and ice water content are added to the specific humidity. This allows METRAS to develop its own clouds, which are then consistent with the model physics. Linear interpolation of the forcing data to the METRAS grid is done in two steps. In the first step, vertical interpolation to the METRAS height levels is performed, and horizontal interpolation to the METRAS grid is performed in the second step.

For the forcing of the water temperatures, the optimum interpolation sea surface temperatures (OISST) analysis dataset (Reynolds et al., 2002), provided by NOAA, are used. It consists of weekly averaged SST data with a spatial resolution of 1° (~110 km). The OISST dataset is produced by interpolating ship and buoy measurements as well as satellite observations. In analogy to the atmospheric variables the SSTs are interpolated horizontally to the corresponding METRAS grid points. To account for rivers and lakes, water temperatures are interpolated from ocean temperatures through the continent (Bungert, 2008) and height corrected using the adiabatic laps-rate of 0.065 K/m over land. Since no reliable soil data are available, the deep soil temperatures are set to be equal to the water temperatures.

5.3.4 Forcing method

The same forcing method is applied to both simulations, i.e. the 4 km simulations forced with the ECMWF data and the 1 km simulations forced with the 4 km results. Since METRAS is always initiated with a 1D profile that is homogenously distributed over the whole domain and height corrected within a diastrophy phase using a dynamical initialization, an averaged profile is determined from forcing data. After the initialization phase, in which the orography grows and a higher numerical accuracy is used, information from the coarser data is forced onto the finer grid solution using the nudging technique. For this, a so-called forcing term is added to the prognostic equations for temperature, humidity, *u*- and *v*-velocity a so-called forcing term is added:

$$\Psi_f = \Psi_m + \delta(\Psi_l - \Psi_m) \tag{5.15}$$

with

$$\delta = \nu \Delta t \tag{5.16}$$

Here Ψ_m is the original value of a variable, Ψ_l is the value of the forcing data, Ψ_f is the resulting value after the forcing, and δ is the weighting factor which depends on the time step Δt and the nudging coefficient ν. For the first hour after the initialization $\nu = \nu_0$ is set to 0.001 s^{-1}. This corresponds to a characteristic time of about 17 minutes, implying that the resulting values are equal to the forcing value after 17 minutes. The homogenous forcing lasts for 1 hour of integration time. Thereafter, the forcing decreases within the domain and the nudging coefficient becomes:

$$\nu(i) = \nu_0 (1 - \tanh(\frac{a_f}{N_f - 3} i)) \tag{5.17}$$

In this study a_f and N_f are set be 0.4 and 4 respectively. The nudging coefficient depends on the grid point distance to the lateral and upper boundaries. The decrease in forcing towards the inner of the model domain allows METRAS to develop its own solution within the domain, but still accounts for large-scale changes due to the forcing at the boundaries.

Since the forcing data are not available for every model time step they are linearly interpolated in time. This might cause problems for the forcing with ECMWF-data due to the 6 hour time step in the analysis fields (Bungert, 2008). For instance, rapid changes in the variables due to fronts are not captured. Also the diurnal cycle is generally not well captured by the 6 hourly forcing. To achieve better forcing data, the 1 km simulations are forced with half-hourly model output obtained from the 4 km simulations.

5.4 Evaluation of dynamical simulations

An advantage of the downscaling method introduced in this thesis is that a direct comparison of observations and model results can be carried out. Most of the dynamical and statistical-dynamical downscaling techniques do not allow this, because they are forced with climate projections and not with observations or reanalysis data. In the following, the evaluation methodology as applied to each model result is described (Section 5.3.1). In Section 5.3.2, the evaluation results are presented.

5.4.1 Methodology

There are several ways to evaluate model results. A well-established approach is the comparison of model estimates with surface observations (Cox et al., 1998; Schlünzen and Katzfey, 2003; Ries and Schlünzen, 2009; Haller et al., 2012 in preparation). In this study, SYNOP stations operated by the DWD, the Royal Netherlands Meteorological Institute (KNMI) and the Institute of Meteorology and Water Management (IMGW) are used. SYNOP stations provide hourly values of surface variables such as temperature, dew point, sea level pressure, cloud cover, wind speed, and wind direction. In the framework of this study, only those stations that i) show measurements for at least 95% of the time for the period of 2006-2010 and ii) are at least 80 km away from the model domain boundaries are selected for model evaluation. The first criterion assures the comparability of the evaluation results between the different runs. The second criterion is applied to avoid the influence from the lateral forcing on the evaluation. In total, 72 stations match both criteria. The station locations and WMO numbers are given in Figure 5.5. For the evaluation of the 1 km simulations, only 10 stations match both criteria.

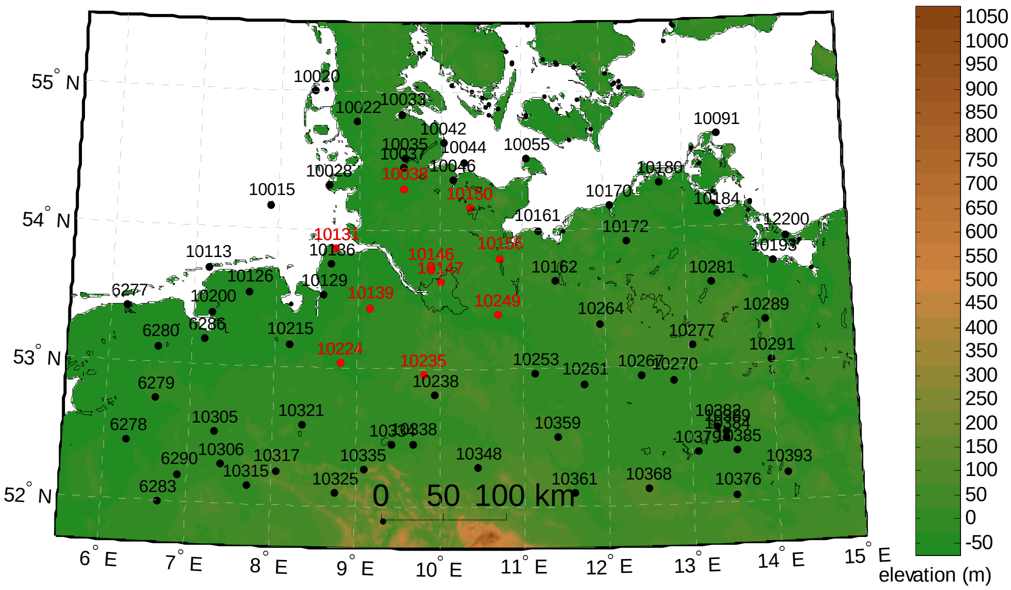

Figure 5.5: Location and WMO number of the SYNOP stations used for the evaluation of the dynamical simulations. Stations used for the evaluation of the 1 km simulations are indicated in red.

The model results are horizontally interpolated to the location of the corresponding station using by bi-linear interpolation. Only the first model level in (10 m above ground) is used because 2 m values cannot be reliably determined for different stabilities due to the use of the flux aggregation approach. The focus of the evaluation presented in this section is on the variables temperature, relative humidity, wind speed, and wind direction. Temperature is chosen because the target parameter UHI is a horizontal temperature difference. Relative humidity and wind speed are chosen because Hoffmann et al. (2011; Chapter 3 of this thesis) demonstrated that both parameters are important for the strength of Hamburg's UHI. Usually, other parameters related to atmospheric moisture content, such as water vapor pressure or dew points are evaluated, because the error in the simulated relative humidity is not only due to problems in the simulation of the humidity processes. However, their distributions seem to be unrelated to the UHI (Hoffmann et al., 2011; Chapter 3 of this thesis). Therefore, it is more important to accurately simulate the relative humidity. This would be different if the evaluation would be done for observations in urban areas, because humidity processes are important for the urban climate. The wind direction is important for advection of temperature and therefore the morphology influences the UHI. Statistical measures are used to quantitatively evaluate the model performance. Following the model evaluation guidelines of COST728 (Schlünzen and Sokhi, 2008), the differences in the means of a variable (*BIAS*; Eq. 5.18), the root mean square error (*RMSE*; Eq. 5.19), the hitrate (*HITR*; Eq. 5.20), and the correlation (*CORR*; Eq. 5.21) are calculated.

$$BIAS = \overline{M} - \overline{O} \tag{5.18}$$

$$RMSE = \sqrt{\frac{1}{N}\sum_{i=1}^{N}(M_i - O_i)^2} \tag{5.19}$$

$$HITR = \frac{1}{N}\sum_{i=1}^{N} n_i \quad with \quad n_i \begin{cases} 1 & \text{if} \quad |M_i - O_i| < D \\ 0 & \text{else} \end{cases} \tag{5.20}$$

$$CORR = \left[\frac{\frac{1}{N}\sum_{i=1}^{N}\left(O_i - \overline{O}\right)\left(M_i - \overline{M}\right)}{\sigma_O \sigma_M}\right] \tag{5.21}$$

$$\sigma_O = \sqrt{\frac{1}{N}\sum_{i=1}^{N}\left(O_i - \overline{O}\right)^2} \tag{5.22}$$

$$\sigma_M = \sqrt{\frac{1}{N}\sum_{i=1}^{N}\left(M_i - \overline{M}\right)^2} \tag{5.23}$$

O_i and M_i denote the observation and the corresponding model result, σ_O (Eq. 5.22) and σ_M (Eq. 5.23) denote the standard deviations of the observations and the model results, $\overline{O}$ and $\overline{M}$ denote the corresponding means, and N is the sample size. The *BIAS* indicates whether a variable is generally overestimated or underestimated and if so, to what extend. The *RMSE* reflects the mean error per model-observation comparison pair. To account for temporal development, such as a diurnal cycle the *CORR* is a frequently used measure. No measurement error is considered in the calculation of *BIAS*, *RMSE* and *CORR*. This deficiency is covered by *HITR* which indicates how often the model results lie within a given predefined uncertainty range to the observed value. The uncertainty range D includes measurement accuracy and the spatial and temporal representativeness of the measurements. The optimal value is 1, which indicates that all model results lie within the uncertainty D of the observation and the minimum value is 0, which indicates that none of the model results is within the uncertainty of the observations. The values for D for temperature, wind speed, and wind direction are taken from Cox et al. (1998) (Table 5.5). It should be stated that these values are not based on the measurement accuracy or representation error, but on the demanded forecast accuracy. However, for temperature and wind speed, they are close to the findings of Lengfeld and Ament (2012) and Lengfeld (2012), who, using a sensor network, investigated the representativeness of 2 m temperatures and wind speed over heterogeneous terrain. For instance, they found that temperature differences between stations (computed every minute) can be 3 K or higher on a distance of about

2 km in a heterogeneous terrain. For relative humidity, the value of *D* is set to ±5% (Table 5.5).

Table 5.5: *Uncertainty range D for different variables. Values for temperature, wind speed, and wind direction are taken from Cox et al. (1998).*

Variable	**Temperature (K)**	**Relative humidity (%)**	**Wind speed (m/s)**	**Wind direction**
Allowed deviations	±2	±5	±1 for ff < 10m s^{-1} ±2.5 for ff > 10m s^{-1}	±30°

The measures for wind direction are calculated differently to the other variables. The mean wind direction is computed by calculating the *u*- and *v*-component of the velocity vector using the wind speed. Thereafter, *u* and *v* are component-wise averaged. The average wind direction is the direction of the resulting vector. The wind direction cannot be measured accurately for low wind speeds. Hence, only wind data for measured wind speeds >1 m/s are used for the evaluation.

To visualize the results, the measures calculated for every station are averaged over all stations. Since the correlation is not additive (Faller, 1981), the arithmetic average does not reflect the true average correlation. Therefore, the Fisher's z transformation, a widely used method (e.g. Krueger and von Storch, 2011; Pennell and Reichler, 2011), is applied to average *CORR*. Following this method, *CORR* is transformed into the normally distributed variable *Z*:

$$Z = \frac{1}{2}\left[\ln(1 + CORR) - \ln(1 - CORR)\right] \tag{5.24}$$

Thereafter, *Z* is averaged arithmetically to yield $\overline{Z}$, which is then transformed back into a correlation:

$$\overline{CORR} = \frac{\left(e^{\overline{Z}} - e^{-\overline{Z}}\right)}{\left(e^{\overline{Z}} + e^{-\overline{Z}}\right)} \tag{5.25}$$

In addition to the strict comparison of observations and model results, a so-called dummy forecast is computed as a benchmark for the skill of the model result. For this the observations of the initial day are used as a forecast for the following days. The model should be better than this simple forecast, which just assumes persistency of the weather. In some cases this could be challenging for the numerical model, such as during anticyclonic conditions with weak large-scale forcing. Then the dependency of the model results on the initial conditions and the boundary conditions at the surface, such as the water and soil temperatures or surface cover data, is very large. For instance, surface temperature gradients could lead to the model developing a local circulation not observed in reality and thus being an artifact of the initially selected soil and water temperatures.

5.4.2 Results

The UHI is investigated for the night from model day 3 to day 4. Therefore, the evaluation results for day 3 will be presented in the following. In addition, the results are divided into the evaluation of the 4 km simulations (Section 5.4.2.1), the comparison between 1 km and 4 km simulations (Section 5.4.2.2), and the comparison between the 1 km simulations with the different land use classes (Section 5.4.2.3).

5.4.2.1 Evaluation of 4 km simulations

Figure 5.6 shows the *BIAS* for the different variables per simulation. Additionally, the mean *BIAS* over all simulations and the mean absolute *BIAS* per simulation are indicated. It is apparent that temperatures are underestimated in all simulations except for WP4M and WP7M which show a positive *BIAS* (Figure 5.6a). On average, temperatures are underestimated by 0.9 K. The averaged absolute *BIAS* for METRAS (1.2 K) is smaller then for the dummy forecast (1.6 K). The *BIAS* for the relative humidity varies between -8% and +10% (Figure 5.6b). On average, the relative humidity is overestimated by about 2%, which is a good result. However, the averaged absolute *BIAS* is 5% and METRAS is only slightly better than the dummy forecast. Interestingly, the simulations showing a large negative *BIAS* in temperature are associated with a large positive *BIAS* in the relative humidity (WP3M, WP3T, WP4T, and WP6T).

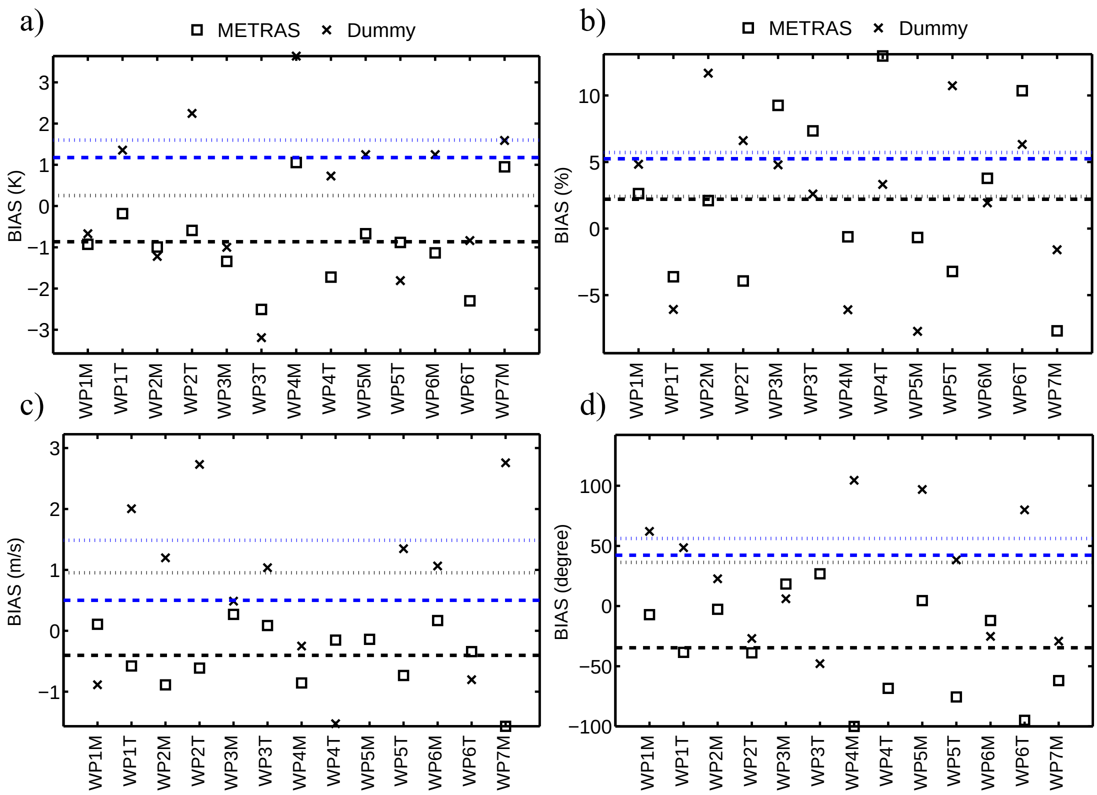

Figure 5.6: *BIAS of the (a) temperature, (b) relative humidity, (c) wind speed, and (d) wind direction for the different simulations for model day 2. Dashed lines indicate the mean (black) and mean absolute BIAS (blue) of the model of all simulations. Dotted lines indicate the mean (black) and mean absolute BIAS (blue) of the dummy forecast.*

The modeled wind speeds are on average slightly underestimated (-0.4 m/s), however, they are underestimated by more than 1 m/s in some simulations (Figure 5.6c). Nevertheless, the average wind speed is well simulated. The averaged *BIAS* of the dummy forecast (1.5 m/s) is three times larger than the modeled one (0.5 m/s). The wind directions are not as well simulated as the wind speed. The values for the *BIAS* range from +30° to -90° and the average *BIAS* is -35° (Figure 5.6d). But there are also simulations with a *BIAS* smaller than ±10°. The average absolute *BIAS* for METRAS is slightly smaller than the absolute *BIAS* of the dummy forecast.

The analysis of the *RMSE* shows that, on average, METRAS performs better than the dummy forecast (Figure 5.7). The averaged *RMSE* for temperature is 2.2 K, which is better than the median of the summarized results from other models (Schlünzen et al., 2012c). The *RMSE* of the relative humidity varies only slightly between the different simulations (Figure 5.7b). The mean *RMSE* is about 12%, which is quite large but again smaller than the value for the dummy forecast. An average *RMSE* of 1.6 m/s for wind speed verifies that this variable is well simulated by METRAS (Figure 5.7c). Similar to the temperatures, METRAS performs better than the median of the analyzed model results shown by Schlünzen et al. (2012c). The

RMSE for the wind directions varies substantially between the simulations (Figure 5.7d). There are two simulations with a *RMSE* around 20° and two simulations with a *RMSE* close to 100°. Nevertheless, the averaged *RMSE* (65°) is again low compared to results other results of other models (median = 72°; Schlünzen et al., 2012c).

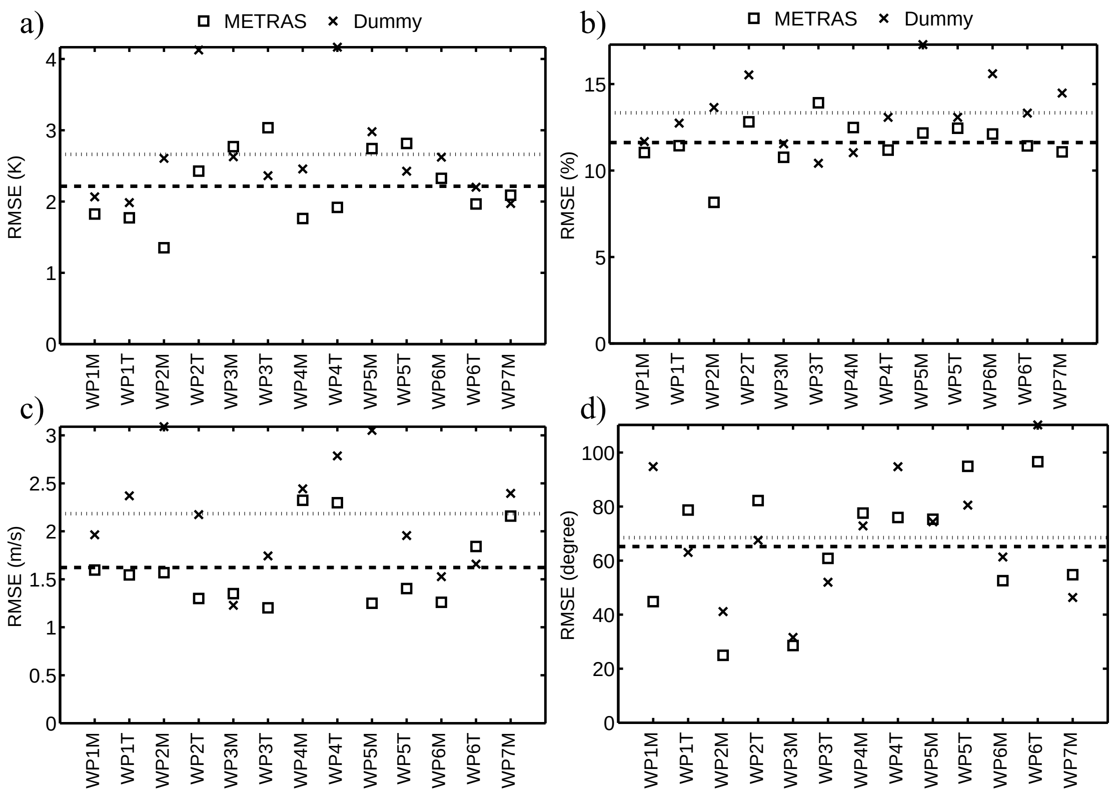

Figure 5.7: *RMSE for (a) temperature, (b) relative humidity, (c) wind speed, and (d) wind direction for the different simulations for model day 2. Dashed lines indicate the average RMSE of all simulations. Dotted lines indicate the average RMSE of the dummy forecast.*

Figure 5.8 shows the result for *HITR*. For temperature, the *HITRs* range from 0.4 to 0.8. On average, *HITR* is about 0.57, which is still an acceptable value. The *HITR* values for relative humidity are lower and do not vary much (Figure 5.8b). The averaged *HITR* for METRAS is 0.32 and therefore slightly lower than for the dummy forecast. This can be partially explained by the *BIAS*, which is in the order of the allowed deviation of 5%, and by the large *RMSE*, which is in the order of twice the uncertainty range *D* (Table 5.5). For wind speed, METRAS performs on average twice as well as the dummy forecast (Figure 5.8c). The mean *HITR* (0.48) is comparable with the results from Schlünzen and Katzfey (2003) for simulations focusing on the Berlin area. Regarding the wind direction, the averaged *HITR* (0.42) is lower compared to those results. However, the *HITR* varies from 0.1 (WP4M) to 0.9 (WP2M).

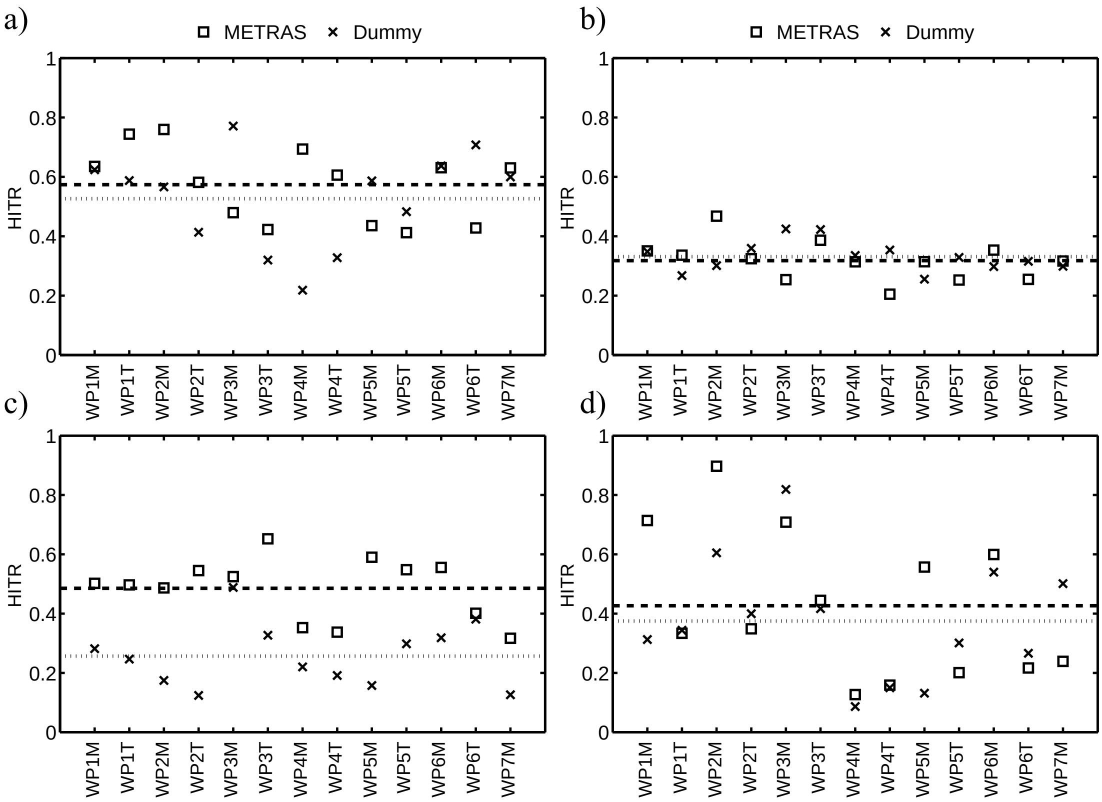

Figure 5.8: *As Figure 5.7 but for HITR.*

The results for *CORR* are shown in Figure 5.9. Temperature and relative humidity show high values of *CORR* (Figures 5.9a,b), a result of the dominant influence of the diurnal cycle of both variables on the calculation of *CORR*. Temporal changes due to fronts are mostly smaller compared to the diurnal cycle and hence do not affect *CORR* substantially. Nevertheless, with an averaged *CORR* for temperature of about 0.92, METRAS performs better than median of the summarized evaluation results from Schlünzen et al. (2012c). The values for wind speed and direction vary between the simulations (Figures 5.9c,d). Even slightly negative values occur and the averaged values for *CORR* are 0.37 and 0.25, respectively. This indicates that temporal changes in the wind vectors are not well captured.

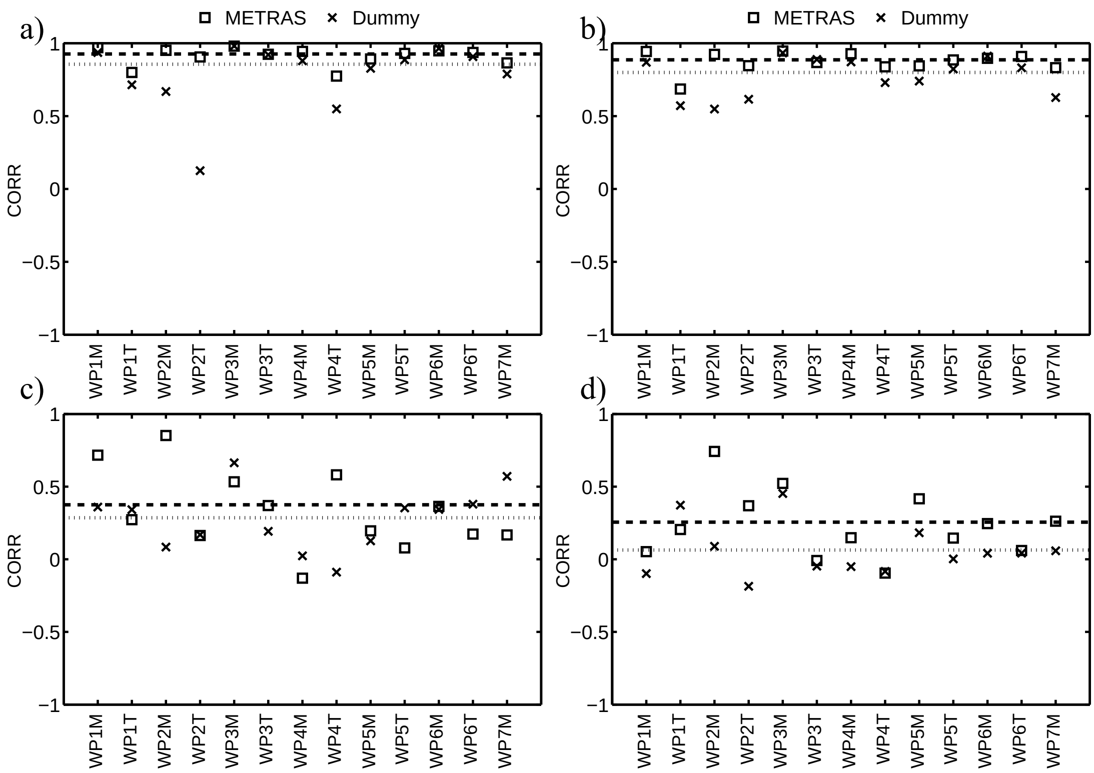

Figure 5.9: *As Figure 5.7 but for CORR.*

In summary, the simulation results for temperature and wind speed are good compared to other model results. For some simulations and some measures they are even better than the best model results summarized by Schlünzen et al. (2012c). The wind direction is difficult to measure accurately because it heavily depends on the surroundings of the measurement site. Therefore, the results for the wind direction are in an acceptable range. If the forcing data were available at higher temporal resolution (now every 6 hours), changes in the flow field due to large-scale phenomena could be better captured, which would especially improve *CORR* for both wind speed and direction. The overestimated relative humidity and the underestimated temperatures indicate problems with the near surface humidity. One possible reason could be the initial soil water availability, which is set to be the same for all simulations and all grid points. This is not realistic because in some parts of the modeled domain this value depends on the preceding dry days. The positive *BIAS* in the relative humidity might also lead to a reduced UHI, because observations indicate that the UHI and relative humidity are inversely correlated (Hoffmann et al., 2011; Chapter 3 of this thesis).

5.4.2.2 Comparison of 1 km and 4 km simulation results

The statistical measures are calculated for 10 stations for both the METRAS 4 km and the METRAS 1 km results (Figure 5.5). The largest differences between both resolutions are found in the simulated temperature and in the wind direction. The results are only marginally different for relative humidity and wind speeds. On average, METRAS 1 km performs slightly better in simulating the wind speed. As an example, *HITR* and *BIAS* are shown in Figures 5.10e,f. The simulation of the wind direction improves in the higher resolution model experiment as well. The *HITR* improves from 0.40 to 0.44 (Figure 5.10g) and the averaged *BIAS* from -30° to -10°. However, the mean absolute BIAS is only slightly reduced. For relative humidity METRAS 4 km shows almost no difference in performance regarding the average *HITR* (Figure 5.10c). The averaged *BIAS* is only 1% for METRAS 4 km, while METRAS 1 km overestimates the relative humidity by almost 7% (Figure 5.10d). Overall, 4 simulations with METRAS 1 km show a *BIAS* of more than 10%. The higher humidity might be a reason for the lower temperatures (Figure 5.10b) and lower *HITR* for temperature (Figure 5.10a) compared to METRAS 4 km. The *HITR* of METRAS 1 km is reduced to the level of the dummy forecast. The high relative humidity could also reduce the UHI, as mentioned in Section 5.4.2.1.

In summary, the higher resolution simulations of METRAS improved the simulation of the near surface flow field, which can be expected due to the better representation of the topography and land-use. The temperature and humidity performance worsens for the 1 km grid compared to the 4 km grid. The differences in temperature and humidity between the two model setups might not only be due to the different resolution, but also to the different surface representation. In addition to the number of classes, the classes also differ in their respective parameters. In particular the initially available soil water is higher in the new surface cover classes (Table 5.4) compared to the old ones (Table 5.3). Therefore, the difference between 1 km simulations with the new surface cover and the old land-use classes will be investigated in Section 5.4.2.3.

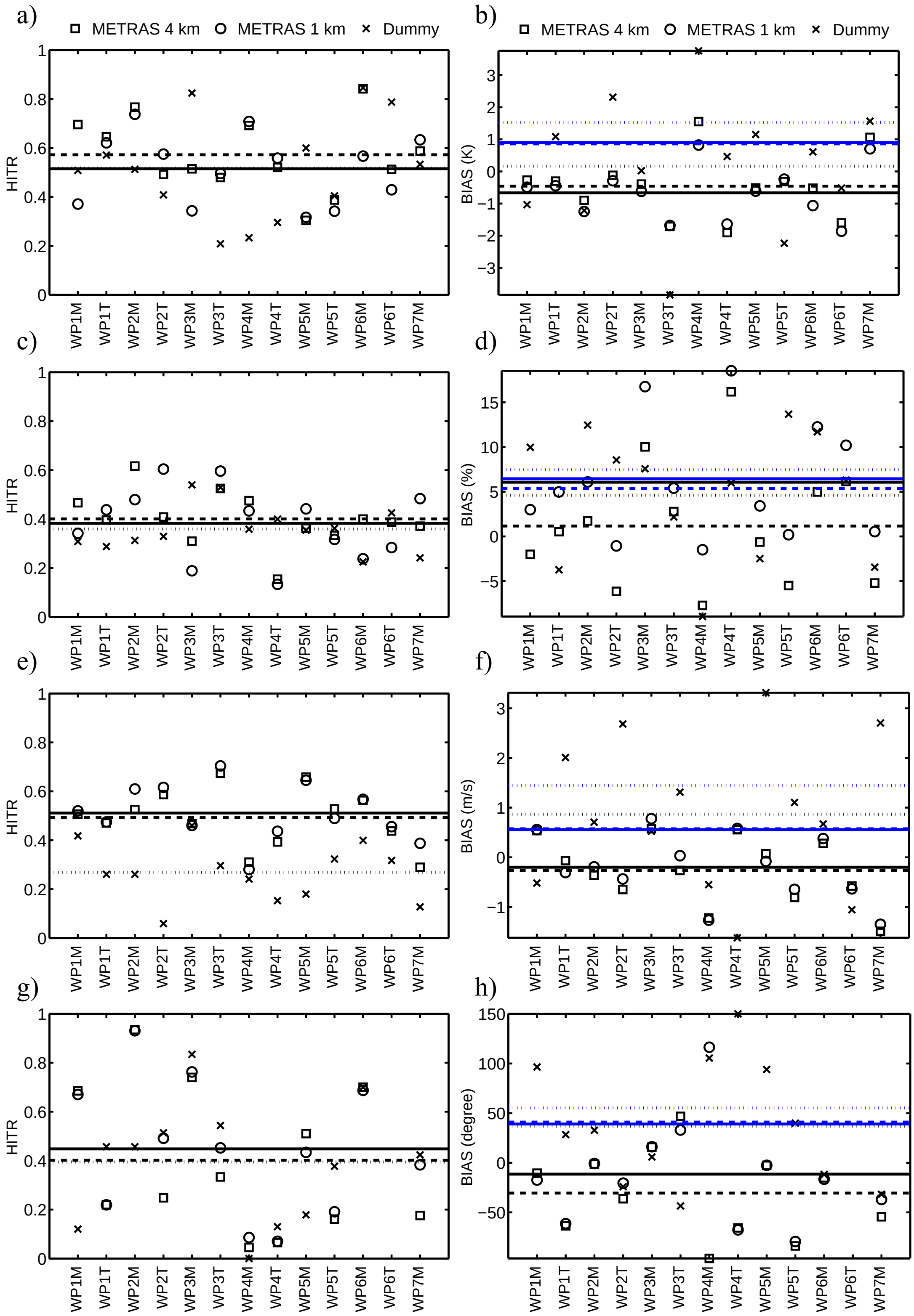

Figure 5.10: *HITR and BIAS of (a,b) temperature, (c,d) relative humidity, (e,f) wind speed, and (g,h) wind direction for METRAS simulations of model day 2. Solid lines indicate the mean (black) of HITR and BIAS, and mean absolute BIAS (blue) of METRAS 1 km simulations. Dashed lines indicate the mean (black) of HITR and BIAS and mean absolute BIAS (blue) of METRAS 4 km simulations. Dotted lines indicate the mean (black) and mean absolute BIAS (blue) of the dummy forecast.*

5.4.2.3 Comparison of 1 km results for old land-use classes and new surface cover classes

The results of both METRAS configurations (36 surface cover versus 10 land-use classes) differ only in temperature and humidity. The differences in wind speed and direction are negligible. Therefore, only results for temperature and relative humidity are presented in the following. In Figure 5.11, *HITR* and *BIAS* for both variables are shown. For temperature the averaged *HITR* increases to 0.58 using METRAS-10 instead of METRAS-36 (Figure 5.11a). This value is slightly larger than the one from METRAS 4 km (Figure 5.10e), which is also the case regarding the *BIAS* (Figure 5.11b). The averaged *BIAS* is reduced from -0.7 K to -0.2 K when using only 10 classes. For relative humidity the results are similar. The *HITR* improves using METRAS-10 instead of METRAS-36 (Figure 5.11d) and the average *BIAS* is reduced to 1% (Figure 5.11d). The *BIAS* is mainly reduced for simulations with large positive *BIAS*. The differences in temperature and humidity between the two model setups might not only be due to the different resolution, but also to the different surface cover representation.

In addition to the comparison using statistical measures, conditional quantile plots are created (Murphy et al., 1989). This plot shows the median and different quantiles (10^{th}, 25^{th}, 75^{th}, and 90^{th}) of the observations depending on the simulated value of a variable. It also includes the corresponding histogram of the simulations. The diagonal line indicates the perfect simulation. The *BIAS* (per interval) of the simulations can be assessed by the deviation of the median and the diagonal line, while the simulation error variability can be assessed by the spread of the quantiles (Ries et al., 2009). Figure 5.12 shows the conditional quantile plots of temperature (bin width = 1 K) and relative humidity (bin width = 5%) for the two METRAS configurations including all simulations for model day 2. It is apparent that the simulated diurnal cycle is weaker than the observed one for both model configurations. Temperatures above (below) 12-13°C are underestimated (overestimated), respectively (Figures 5.12a,b). The underestimation is larger in the METRAS-36 simulations, especially for higher temperatures (Figure 5.12a). The corresponding plot for relative humidity (Figure 5.12c) shows that in these simulations, the relative humidity is overestimated throughout the distribution. This is not the case for the METRAS-10 simulations (Figure 5.12d). Here, the median line is close to the 1:1 line, except for the rare very high and low values. However, it is apparent that error variability is quite large in these simulations.

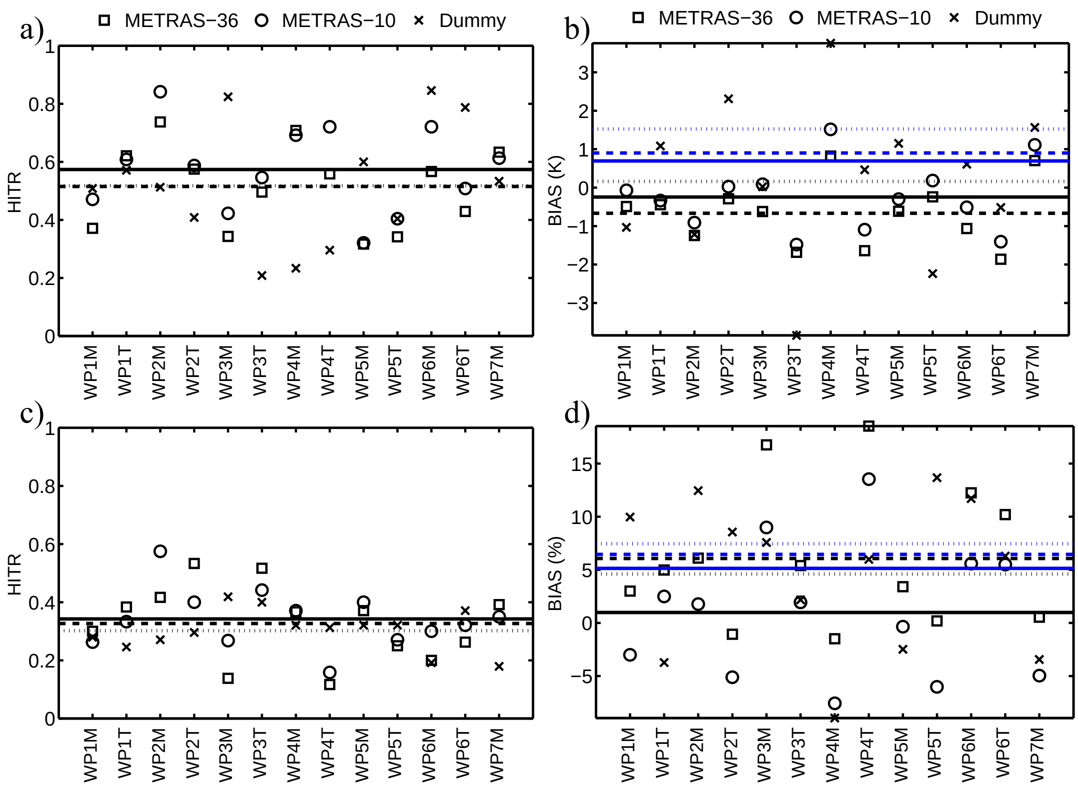

Figure 5.11: *HITR and BIAS of the (a,b) temperature and (c,d) relative humidity for the different simulations for model day 2. Solid lines indicate the mean (black) of HITR and BIAS, and mean absolute BIAS (blue) of METRAS-10 simulations. Dashed lines indicate the mean (black) of HITR and BIAS and mean absolute BIAS (blue) of METRAS-36 simulations. Dotted lines indicate the mean (black) and mean absolute BIAS (blue) of the dummy forecast.*

These results confirm that the small improvements of the 1 km simulations compared to the 4 km simulations (Section 5.4.2.2) are due to the different surface treatment. When using the 10 land-use classes for both resolutions, the increased resolution does improve the simulation of temperature and relative humidity. It should be tested whether a change in the soil water parameters improves the results from the simulation utilizing the 36 surface cover classes. The influence of the new surface cover classes on the spatial patterns of temperature and other variables cannot be sufficiently investigated due to the limited number of observational sites. To account for pattern changes, the downscaled UHI is compared to the UHI data from Bechtel and Schmidt (2011) and Schlünzen et al. (2010) in Section 5.5.1.

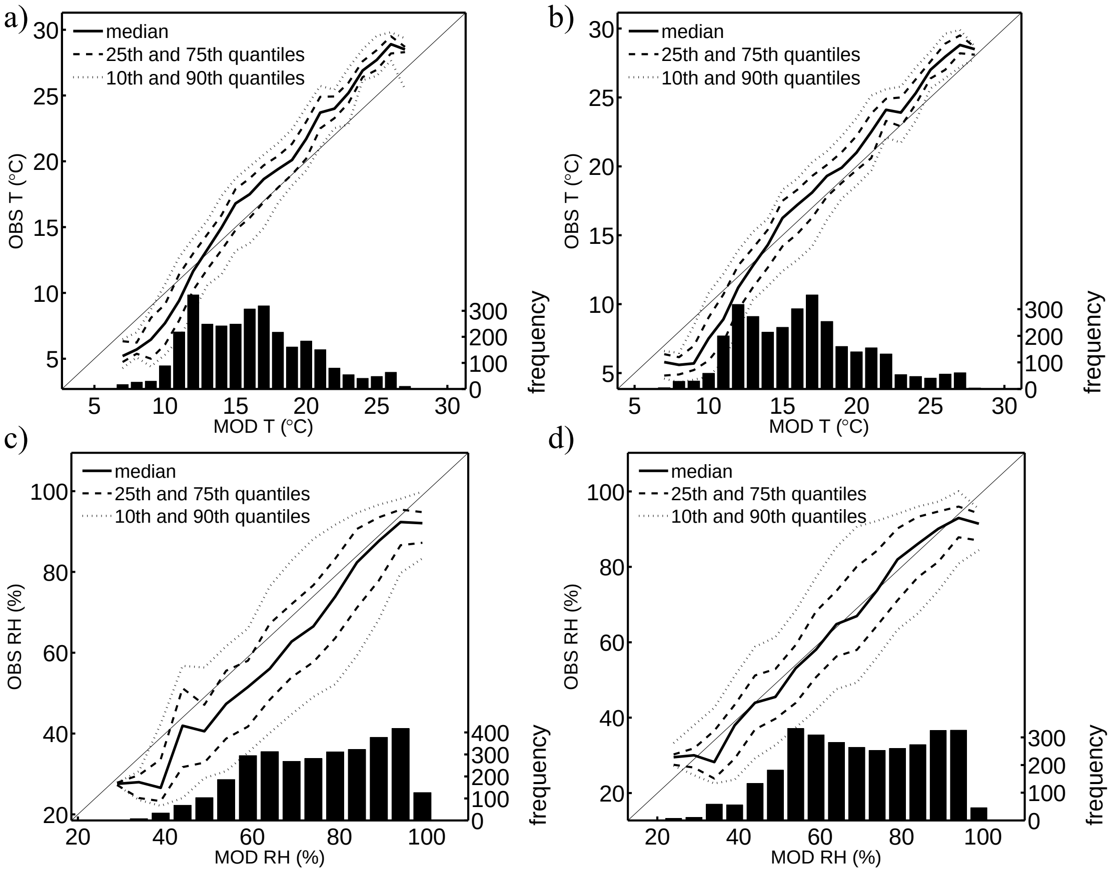

Figure 5.12: *Conditional quantile plots of model result conducted with METRAS-36 ((a) temperature, (c) relative humidity) and with METRAS-10 ((b) temperature, (d) relative humidity).*

5.5 Urban heat island results of statistical-dynamical downscaling

The SDD method is applied to ERA40 (WPs) combined with DWD observations (statistical model) as well as to RCM data from REMO, CLM and CCAM. The METRAS results are investigated with regard to the UHI. The results for the present climate are given in Section 5.5.1. The resulting UHI patterns are than evaluated with observed data (Section 5.5.2). Future changes are investigated in Section 5.5.3.

5.5.1 Urban heat island in the present climate

To statistically recombine the results of the dynamical simulations, the UHI needs to be calculated for each simulation separately. Generally, there are two methods to determine the UHI from one simulation. The first method is to conduct two simulations, one with the actual surface cover and one without the urban surfaces, and subtract both simulation results from each other (e.g. Hjemfelt, 1982; Hafner and

Kidder, 1999; Zhou and Shepherd, 2009; Grawe et al., 2012 submitted). This method would double the computational effort and additional problems arise, such as the composition of the non-urban surface cover. Hence, it was not applied in the present study. The second method involves subtracting temperatures at rural grid points from the whole temperature field (e.g. Flagg, 2010). Since this method does not require additional simulations and is straight forward to compute, it is used in context of this study.

The 10 m temperature values from single grid points closest to the two DWD stations Grambek and Ahrensburg are averaged to obtain a representative rural temperature value. To compare the numerically simulated UHI values with the statistically modeled UHI (Section 5.2) and to investigate the temporal variability of the UHI intensity, the 10 m temperature closet to the DWD station Hamburg-St. Pauli is used to represent the urban temperature as in Hoffmann et al. (2011; Chapter 3 of this thesis). The time series of the simulated urban-rural temperature differences ΔT_{u-r} using METRAS-36 is shown in Figure 5.13. It is apparent that the magnitude of differences is much smaller than the corresponding statistically modeled values as shown in Table 5.1. This inconsistency can be explained partially by the different definition used to calculate ΔT_{u-r}. The statistical model is based on differences in the minimum temperature (Section 5.2), while temperature differences ΔT_{u-r} from the numerical simulations are calculated at a fixed time. Additionally, the statistical model explains only 50% of the UHI variance. Therefore, in reality the UHI can be smaller than statistically modeled one in some cases. However, this cannot explain that all simulations show smaller UHI. Another reason is that the numerically simulated temperatures are average temperatures over an area of 1x1 km^2. Also the use of 10 m temperatures instead of the 2 m temperatures can lead to smaller UHI intensities. Schlünzen (2012) showed that the urban-rural temperature differences in model results are larger when using the 2 m values instead of 10 m values. Flagg (2010), who conducted simulations for Detroit using the Weather Research and Forecast Model (WRF), presents similar findings. As shown in Section 5.2, the relative humidity is overestimated in most of the simulations. This could also lead to a reduction of the UHI because both variables are inversely related. Additionally, the lack of a canopy layer parameterization also reduces the urban effect. METRAS simulations conducted for London using the BEP (Martilli et al., 2002) showed an increase of about 1 K within urban areas compared to simulations without BEP (Grawe et al., 2012 submitted). In addition, the effect of anthropogenic heat release is disregarded. Grawe et al. (2011) showed that for Hamburg, the nocturnal urban temperatures increase by up to 1 K when incorporating anthropogenic heat release. These effects might not superimpose linearly but including them would increase the UHI intensity. Hence, the

UHI would be closer to the statistically modeled UHI values if both parameterizations were included.

Nevertheless, the ΔT_{u-r} time series show a typical diurnal cycle of the temperature differences (Oke, 1987) on day 3 and day 4. The average of all simulations shows positive differences from noon to the early morning (around sunrise) with a maximum between 8 p.m. and 12 a.m. LST. Negative values occur between 7 a.m. and 12 p.m. LST. After sunrise, rural areas heat up at higher rates than the urban areas. This so-called urban cool island (UCI) is mainly due to the high thermal conductivity and diffusivity of urban surfaces. The heat is transported faster into the ground, which leads to a reduced warming of the air in the morning. The UCI effect was found for Hamburg by Schlünzen et al. (2010). They showed that the maximum temperatures within the city are slightly lower compared to Grambek, especially in summer. Later during the day this effect becomes less important and disappears after sunset.

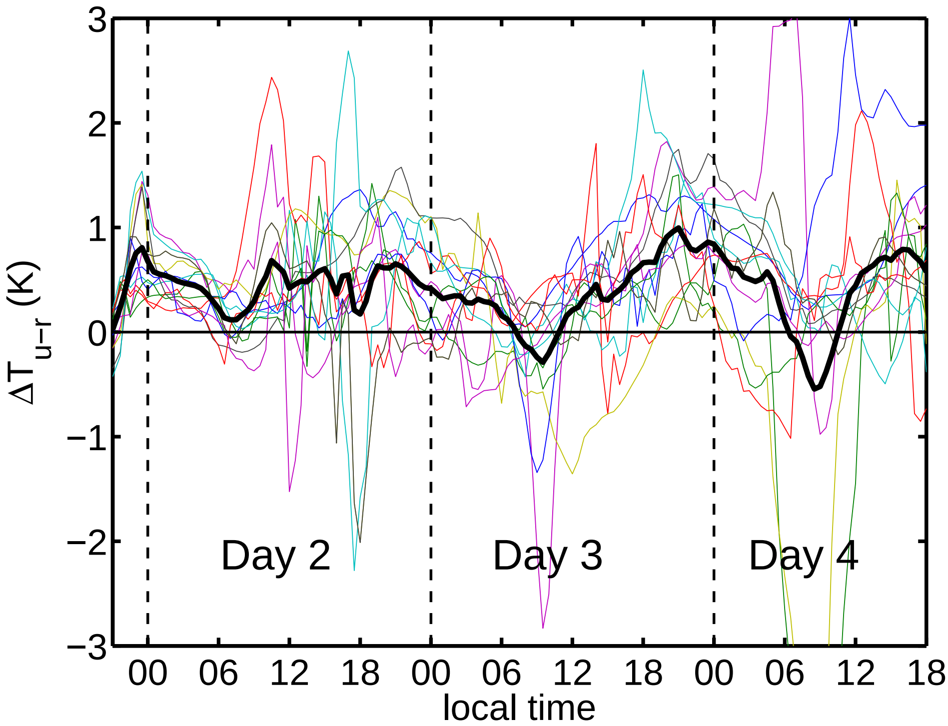

Figure 5.13: *Simulated time series of the urban-rural temperature difference* ΔT_{u-r} *from all 13 simulations (Table 5.1) conducted with METRAS-36. Black solid line indicates the unweighted average of all simulations.*

Investigation of the individual time series reveals substantial temporal variability of the differences. The large positive and negative values at day 4 are artifacts due to clouds. Due to their random nature, clouds are also a general problem when comparing or combining results from different simulations. Using data from only one model output time step to compare simulations could result in large spatial differences not due to urban effects, but due to the presence of small clouds. Therefore, the nocturnal UHI intensity is defined in two ways: average temperature difference between 8 p.m. and 12 a.m., and maximum temperature differences between 6 p.m. and 6 a.m. the next day. The later is frequently used in observational studies (e.g. Morris et al. 2001; Kim and Baik, 2002; 2004). The average UHI is then determined at those times, when the average time series in Figure 5.13 shows a maximum. Both definitions are also applied to results from METRAS-10 simulations. The resulting UHI intensities are presented in Table 5.6. As it is also visible in Figure 5.13, the averaged simulated UHI magnitude is much lower than the statistically modeled one. On average, the differences between the different METRAS versions are small and not significant at the 95%-significance level. Nevertheless, UHI values differ by up to 0.5 K for some simulations. When investigating the differences between the simulations, the UHI values for the maximum UHI day are much lower than the UHI for the threshold day for WP2. To a smaller extent, this is also the case for the WP5 simulations conducted with METRAS-36. As mentioned in Section 5.2; the statistical model explains only 50% of the UHI variance and has an *RMSE* of 1.2 K. Hence, the maximum UHI day might have a lower UHI than the threshold day if the difference between the statistically modeled UHI intensity is small. This is the case for both WPs. However, the effect on the statistically recombined UHI pattern is small because the combined weights of WP2 and WP5 are only 6%.

The definition of the UHI that use the maximum nocturnal temperature difference is not applicable for the calculation of the simulated UHI patterns. The time of the maximum is different for the individual grid points and the individual simulations. Hence, for every simulation the temporally averaged (8 p.m.-12 a.m. LST) rural temperatures are subtracted from the temperature field to yield the UHI pattern. To compute the averaged strong UHI pattern (Section 5.2), the frequency of the ERA40 WPs and the observations from Hamburg-Fuhlsbüttel in the period 1971-2000 are used to calculate the weights for the different simulations according to Eq. (5.3) and Eq. (5.4). Thereafter, the individual UHI patterns are multiplied with their corresponding weights (Section 5.2). On average, 24.9 strong UHI days (statistically modeled UHI $\geq$ 3 K) occurred in the summer season based on the statistically modeled UHI for period 1971-2000. The resulting averaged strong UHI pattern determined from METRAS-36 results is presented in Figure 5.14a. The maximum UHI intensity, with up to 1.2 K, is found in the harbor and in downtown Hamburg. The result is understandable because the large fraction of sealed surfaces in this area. The river Elbe also contributed to the UHI pattern due to weak nocturnal cooling of the water body. This effect is responsible for the increased nocturnal temperatures in the western part of the city, i.e. where the river is relatively wide. A detailed examination of the pattern reveals that structures such as the two airports within Hamburg namely Fuhlsbüttel (north of the Alster lake) and Finkenwerder (western part of Hamburg), can be indentified. Both areas show higher temperatures than their surroundings. In the southeastern part of the city, where the surface cover is rural, higher temperatures are simulated as well. This may be due to the low elevation in this area, which can affect the temperature.

Table 5.6: *Numerically and statistically modeled UHI intensities (Section 5.2) in Kelvin for the different simulations. For the numerically modeled values the temporally averaged urban-rural temperature difference (8 p.m.-12 a.m. LST) and the maximum urban-rural temperature difference between 6 p.m. and 6 a.m. LST (max) are given.*

Simulation name	METRAS-36		METRAS-10		Statistical model
	averaged	max	averaged	max	
WP1M	1.22	1.31	1.39	1.47	4.6
WP1T	0.30	1.03	0.35	0.96	3.0
WP2M	0.46	0.75	0.53	0.84	3.3
WP2T	1.18	1.46	1.62	1.89	3.0
WP3M	1.48	2.96	1.59	1.94	5.7
WP3T	0.26	0.34	0.63	0.69	3.0
WP4M	1.57	1.75	1.55	1.86	4.0
WP4T	0.93	1.23	0.91	1.09	3.0
WP5M	0.79	1.50	0.89	1.28	4.1
WP5T	0.84	1.50	0.54	0.89	3.0
WP6M	1.44	2.50	1.89	2.72	5.2
WP6T	0.76	0.83	1.18	1.38	3.1
WP7M	0.51	1.34	0.54	0.83	3.2
mean	0.90	1.42	1.04	1.43	3.71

To test this hypothesis the temperature fields are height corrected. First, the mean temperature gradient between first (~10 m above ground) and ninth (~185 m above ground) vertical level over an area of 61x61 km^2 is computed for each output time. The mid-point of this area is set to Hamburg-St. Pauli. Since METRAS uses a terrain following coordinate system, only grid points with an elevation lower than 5 m are used. Furthermore, water fraction of the grid point should be less than 40%, which avoids overweighting of water surfaces. Due to the distinguished thermal characteristics between water and other land surfaces, the temperature gradients are different especially after sunset and sunrise. The obtained mean gradients are then used to correct the 10 m temperatures according to the elevation. Applying the height correction reduces the magnitude of the UHI (Figure 5.14b). As previously assumed, the UHI values in southeastern part of the city are reduced. Only a small area with higher UHI values is left. This area corresponds with Geest hillside, which receives more shortwave radiation throughout the day than the surrounding area due to the slope of the terrain. As a result the nocturnal temperatures increased as well.

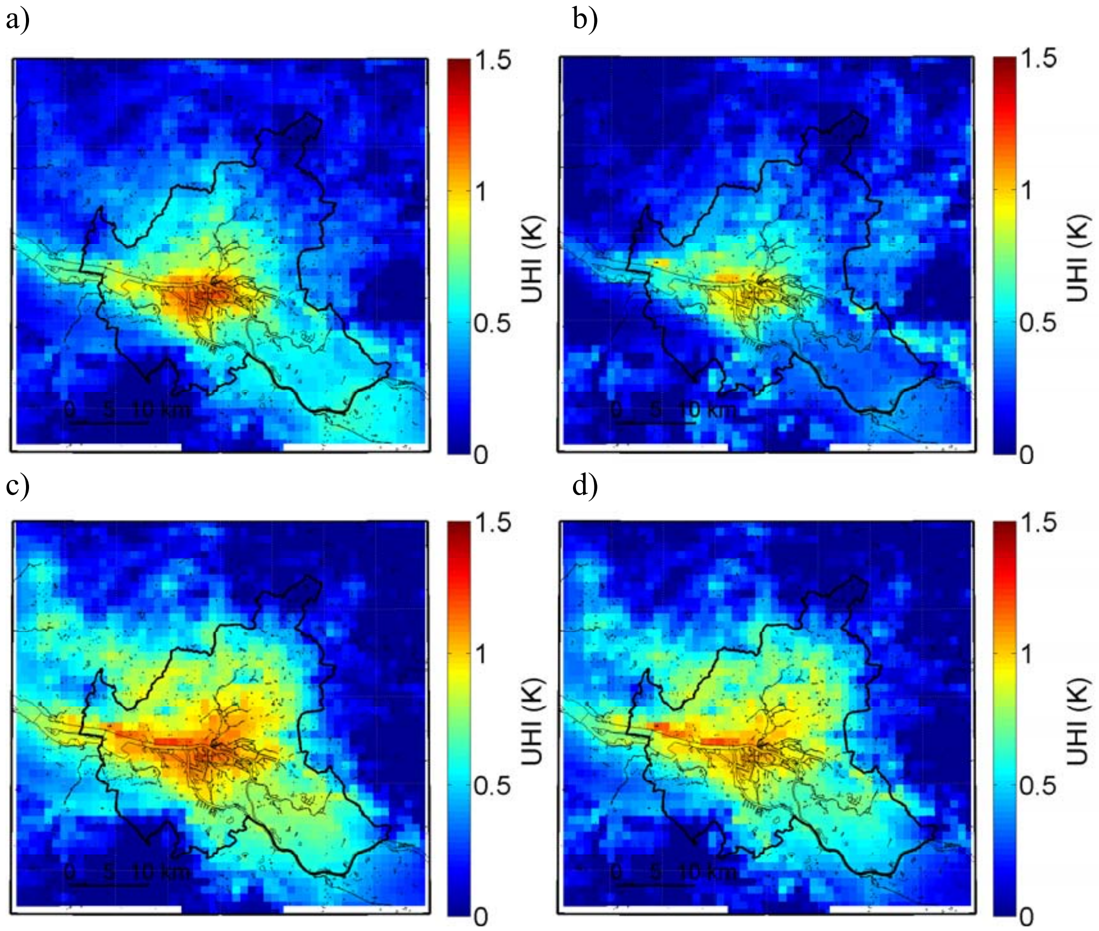

Figure 5.14: *Statistical recombined UHI pattern using data for the period 1971-2000 for summer: METRAS-36 simulations (a) without height correction and (b) with height correction. METRAS-10 simulations (c) without height correction and (d) with height correction.*

To investigate the impact of the surface representation, the UHI pattern is computed for METRAS-10 simulations as well. Figures 5.14c,d show the corresponding patterns without and with height correction. The area of increased temperatures is larger compared to the METRAS-36 results. This is mainly due to the simpler treatment of urban surfaces. METRAS-10 simulations are conducted with only one urban class. In this class, the fraction of surfaces such as backyards or street trees located within urban areas is only indirectly considered by choosing the surface characteristics. Thus, the fraction of these surfaces does not vary within the city, as it is the case for the METRAS-36 simulations. Therefore, also suburban areas develop a considerable UHI. This is evident in the northwestern and northeastern parts of the city. Applying the height correction to the results reduces the intensity of the UHI. The decrease of the UHI in the southeastern parts is not as strong as in the METRAS-36 simulations, and the impact of the Geest hillside is hardly visible.

5.5.2 Evaluation of the UHI pattern

Only few meteorological observations are available to evaluate Hamburg's UHI pattern. However, as done by Bechtel and Schmidt (2011) for the temperature proxy data, the observed temperature differences between the rural station Grambek and five stations in and around Hamburg are correlated with the simulated UHI pattern. For the comparison as derived by Schlünzen et al. (2010) the annually averaged UHI and the summer-averaged UHI is used. Additionally, the UHI pattern constructed by Bechtel and Schmidt (2011), which used floristic mapping data, is compared with the numerically simulated UHI patterns. The so-called Ellenberg indicator values for temperature (EIT) are used as proxies for the temperature distribution within Hamburg. As described by Bechtel and Schmidt (2011) a linear regression with the UHI values given by Schlünzen et al. (2010) as predictor and the EIT as the predictand is computed to receive Ellenberg based UHI values (UHIE). Therefore, both UHI datasets are not fully independent. The UHIE dataset covers the area of the city of Hamburg on a 1x1 km^2 grid, without water bodies, because plant data do not exist for water-covered areas. To compute the *CORR*, the UHI pattern simulated by METRAS is linearly interpolated onto the grid of the UHIE dataset.

Table 5.7 shows the *CORR* values for the results of METRAS-36 and METRAS-10 simulations with and without the height correction described in Section 5.5.1. The METRAS-36 UHIs show higher *CORRs* than the METRAS-10 UHIs. As mentioned in Section 5.5.1, this is most probably due to the spatial distribution of the urban surfaces and the more accurate reflection of urban surfaces. All *CORRs* are significant (at $\alpha = 0.1$) in the METRAS-36 results. The highest *CORR* with 0.8 is obtained for the comparison between the uncorrected METRAS-36 results and the averaged temperature differences in the summer season. The *CORR* values are smaller for the height corrected pattern compared to the corresponding non-corrected patterns. When comparing with the UHIE pattern the uncorrected METRAS-36 pattern performs best and the METRAS-10 patterns show both weaker *CORRs* compared to their corresponding METRAS-36 patterns. Due to the large number of data points available for UHIE, all *CORR* values are significant (at $\alpha = 0.05$).

Table 5.7: *CORR values determined for the comparison of different observational data with the numerically simulated mean strong UHI patterns with and without height correction produced with METRAS-10 and METRAS-36. Statistically significant results are indicated with (*) for α = 0.1 and with (**) for α = 0.05.*

Comparison data	**METRAS-36**		**METRAS-10**	
	without height correction	**with height correction**	**without height correction**	**with height correction**
Schlünzen et al. (2010)	0.76*	0.74*	0.65	0.64
Schlünzen et al. (2010) JJA	0.80*	0.75*	0.68	0.65
Bechtel and Schmidt (2011)	0.74**	0.72**	0.70**	0.69**

The comparison with observed data can be used to identify the simulation that shows the best agreement with the observation. For the comparison with the observed UHI (Schlünzen et al., 2010), no significant *CORR* can be found. Therefore, Table 5.8 lists only the *CORR* for the different simulations using uncorrected METRAS-36 results in comparison with the UHIE dataset. All correlations are lower than the statistically recombined UHI pattern. This shows that more than one simulation has to be conducted to obtain the UHI pattern of Hamburg. The highest *CORR* (0.7) can be found for WP4M. This corresponds to the *CORR* calculated for the statistically recombined METRAS-10 results. The results again show that the use of the 36 surface cover classes improves the pattern of the simulated UHI. In addition, the WP4M simulation could be used for sensitivity studies regarding adaption measures, if only the UHI pattern is of interest. The lowest value for the *CORR* is found for WP4 as well (0.37). Hence, it cannot be concluded that WP4 generally produces a typical UHI pattern. The other *CORR* values range from 0.47 to 0.63.

Table 5.8: *CORR values determined for the comparison between the UHIE pattern derived by Bechtel and Schmidt (2011) and the UHI patterns for the different METRAS-36 simulations without height correction. All values are statistically significant (at α = 0.05).*

Simulation name	CORR
WP1M	0.63
WP1T	0.49
WP2M	0.51
WP2T	0.61
WP3M	0.60
WP3T	0.51
WP4M	0.70
WP4T	0.36
WP5M	0.47
WP5T	0.48
WP6M	0.60
WP6T	0.61
WP7M	0.48

5.5.3 Urban heat island in the future climate

Future changes in the statistical-dynamically downscaled UHI pattern (Section 5.5.1) are determined calculating the statistical weights (Eq. 5.6 and Eq. 5.7) for each RCM (Section 5.5.2) for different periods. For present climate the period 1971-2000 is chosen. For the future climate the two periods 2036-2065 and 2070-2099 are used. CCAM results are only available for the periods 1971-2000 and 2070-2099. The two realizations of REMO and CLM projections are combined as done in Chapter 4. This accounts to some extent for the natural climate variability. Afterwards, the difference between the present UHI pattern and the future UHI pattern is calculated. Since the METRAS-36 simulations without height correction showed the best spatial agreement with measurements, these simulations are used for the calculations. Besides changes in the UHI pattern, the number of strong UHI days N_{strong} (Eq. 5.2) might change as well. Hence, the annual N_{strong} is calculated for present and future periods (Table 5.9). The statistical significance of these changes is determined using bootstrap re-sampling ($N = 10000$). The applied method assumes that the morphology of Hamburg does not change in a future climate.

Table 5.9: *Annual number of strong UHI days N_{strong} ($\Delta T_{u-r} \geq 3$ K) in summer (JJA) for different RCM results and different periods. The two realizations of REMO and CLM are combined. Results are shown for non-corrected and bias corrected projections of REMO and CLM. Significant changes are indicated by (**) for $\alpha = 0.05$.*

period	REMO		CLM		CCAM
	without bias-correction	with bias-correction	without bias-correction	with bias-correction	
1971-2000	16.3	22.2	10.2	24.6	47.7
2036-2065	16.9	22.8	11.4	26.8	-
2070-2099	17.3	26.8	15.4**	32.0**	55.1

For the RCM data without bias correction, the changes in the mean strong UHI pattern for the future period 2036-2065 are presented in Figure 5.15. For both REMO and CLM the changes are marginal (Figures 5.15a,b). They show slight increases within the city. These changes are, however, below 0.05 K. Even though the pattern does not change, N_{strong} slightly increases for both models (Table 5.9). These changes are not significant. N_{strong} is underestimated by REMO and CLM for the present climate without-bias correction (ERA40 = 24.9 days). This is mostly due to biases in the variables used in the statistical model (Schoetter et al., 2012), which reduce the statistically modeled UHI. Hence, it is questionable if the statistical model, which is determined from observations, can be directly applied to uncorrected RCM results. For that reason, the bias-corrected data are used to investigate UHI changes. Figures 5.15c,d show changes in the UHI pattern for the bias-corrected RCM data. REMO shows nearly no changes at all, while the CLM pattern increases almost constantly over large parts of the city as well as over the surrounding rural areas. After the bias-correction REMO still underestimates N_{strong} by 2.7 days for the present climate while the CLM result is very close to the value derived from the combination of ERA40 based WPs and observation based statistical model (Table 5.9). For REMO the absolute signal remains constant with +0.7 days for mid of the 21st century. The signal for CLM increases to +2.2 days. Nevertheless, both change signals are not significant.

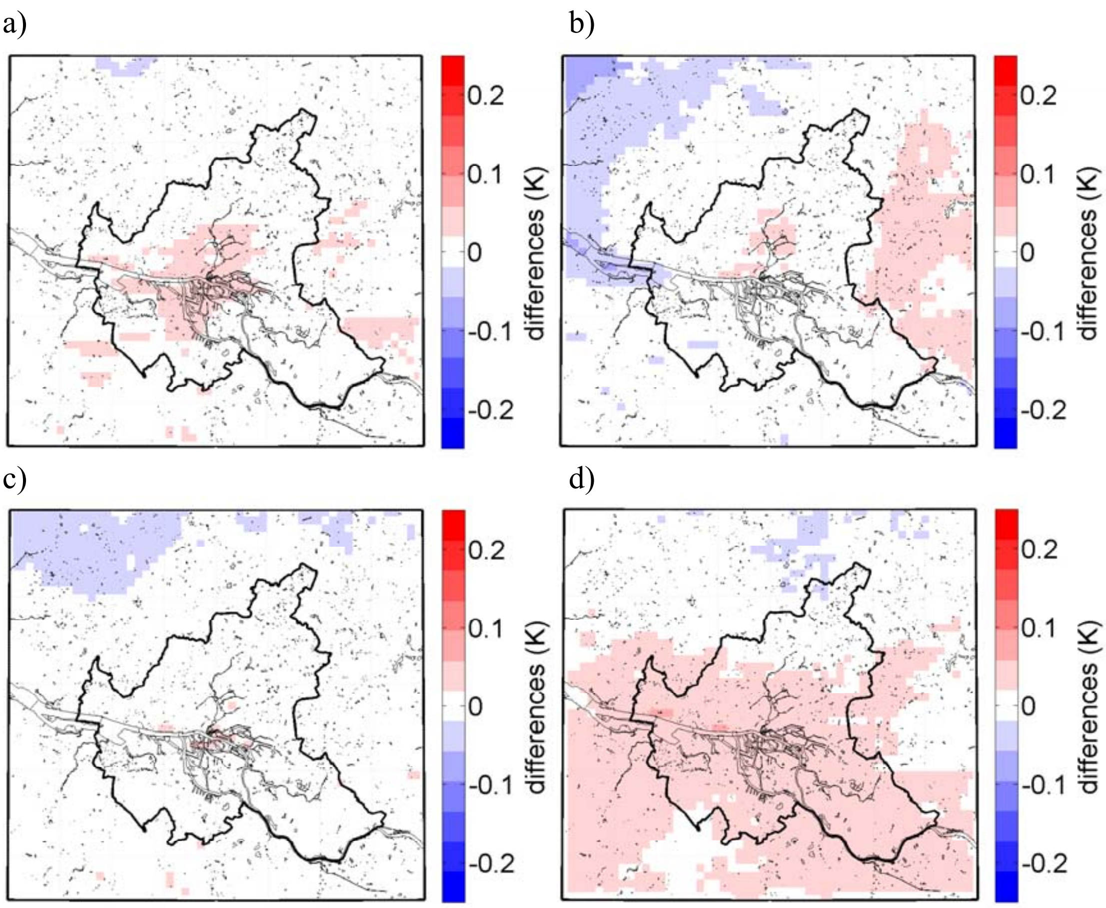

Figure 5.15: *Differences in the statistically-dynamically downscaled UHI pattern in summer (JJA) between the future period 2036-2065 and the present climate using uncorrected (a) REMO and (b) CLM and bias corrected (c) REMO and (d) CLM data .*

At the end of the century (2070-2099), the changes for the uncorrected REMO and CLM results are smaller than for the earlier period (Figures 5.16a,b). However, the number of strong days increases about +1 day for the REMO results and up to +5.2 days for the CLM results. The latter increase is statistically significant and confirms the findings from Hoffmann et al. (2011; Chapter 3 of this thesis), who found an increase in the statistically modeled UHI for UHI > 4 K based on CLM results. CCAM results result in large changes in the UHI pattern (Figure 5.16e). In the western parts of Hamburg the UHI increases up to 0.13 K, which is about 10% of the maximum UHI intensity (~1.2 K) determined in Section 5.5.1. The area of the largest increases occurs over the river Elbe. This is due to the large influence of the water temperatures on the temperature pattern for some situations, which become more relevant in a future climate (e.g. WP4M). The increases in the surroundings of Hamburg indicate that the changes can partially be attributed to non-urban related features of some simulations, for example an east-west temperature gradient over the whole domain. In contrast to REMO and CLM, CCAM overestimates N_{strong} (Table 5.9), which is due to a large negative bias in the relative humidity for the present climate. Bias corrected data are not available for CCAM.

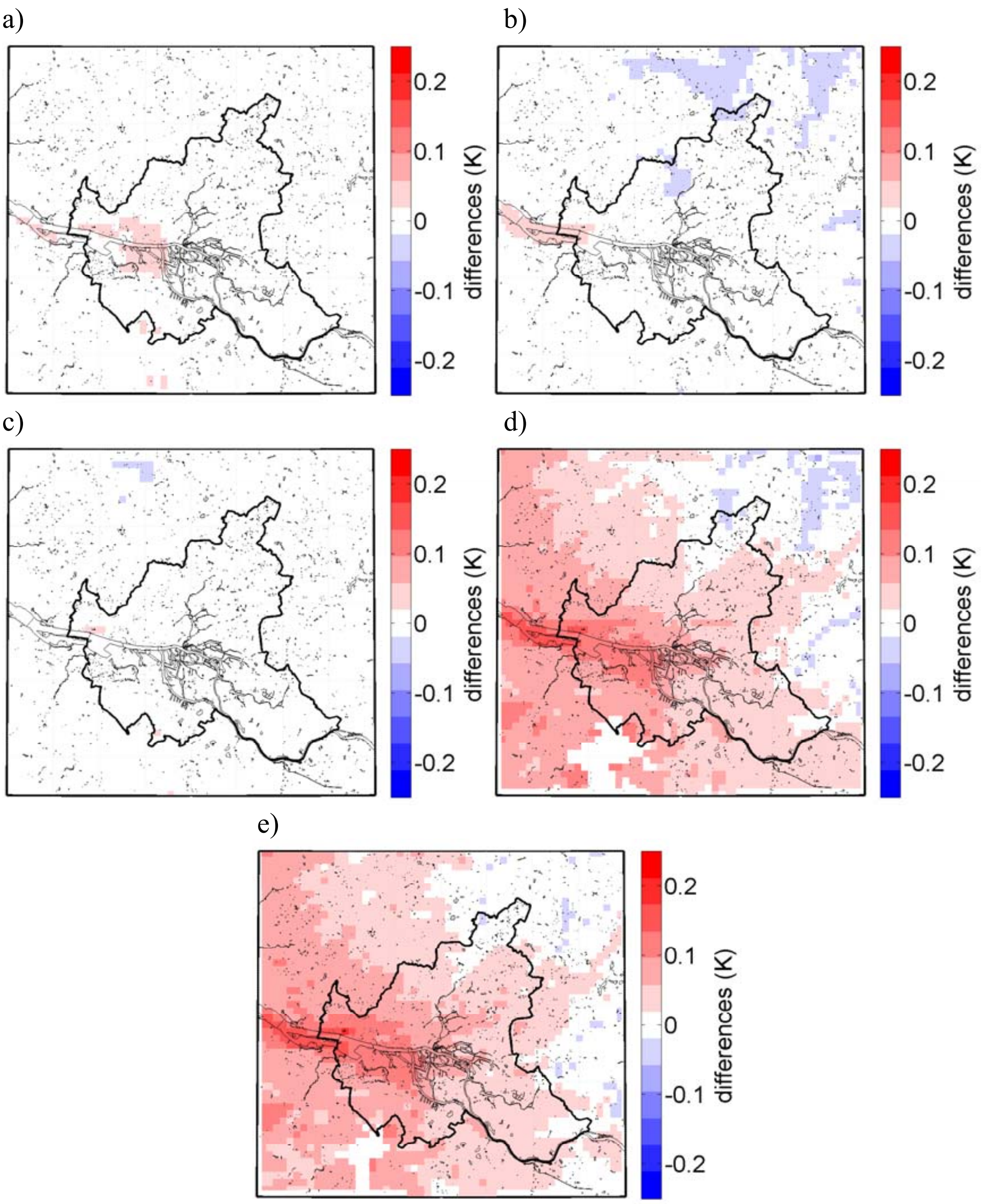

Figure 5.16: Differences in the statistically-dynamically downscaled UHI pattern in summer (JJA) between the future period 2070-2099 and the present climate using uncorrected (a) REMO and (b) CLM, bias corrected (c) REMO and (d) CLM data, and uncorrected (e) CCAM results.

Using the bias-corrected data, the changes are smaller for REMO (Figure 5.16c). For CLM pattern changes are similar to the CCAM pattern (Figure 5.6e). This is mainly due to the increased weighting of the WP4M simulation, which is similar for CLM and CCAM. Hoffmann and Schlünzen (2012; Chapter 4 of this thesis) showed that the frequency of WP4 increases especially at the end of the century for CLM results. Additionally, the weight for the WP4T simulation does not increase, which means that the statistically modeled UHI increases within WP4. For the uncorrected CLM results this is not the case. The bias correction also changes the signal of N_{strong} from +5.2 days to +7.2 days. The latter value corresponds to the change determined CCAM results. The REMO signal increased from +1 day to +4.6 days, which is still not statistically significant.

5.6 Conclusions

A statistical-dynamical downscaling method is developed and applied to downscale Hamburg's UHI. It combines a WPC with a statistical UHI model to determine relevant weather situations, which are simulated with the mesoscale numerical model METRAS forced with ECMWF data. The final horizontal resolution of 1 km is achieved with a two-step nesting with an intermediate simulation on a 4 km grid. The 1 km simulations are conducted twice with a simple land-use classification and with much more detailed surface cover classes that account for the heterogeneity of surfaces within the city. The final UHI pattern is computed by a statistical recombination of the simulation results. Since this downscaling method involves simulations of real weather situations these results can be evaluated with observed data directly.

Both the 4 km and the 1 km simulations are evaluated against DWD observations. Due to the poor coverage of measurements within the city a direct evaluation of the urban effects is not possible. For both resolutions the temperatures are underestimated while the relative humidity is overestimated. An influence of such biases on the UHI is possible and was derived with a statistical model, but should also be investigated in model sensitivity studies. Compared to evaluation studies summarized by Schlünzen et al. (2012c) simulations conducted in the present study are on average within the range of evaluation studies performed by other models. The variation between the evaluation results of the individual simulations are, however, high, such that some simulations show better results than the best evaluation results summarized by Schlünzen et al. (2012c). In general, the near ground temperatures are underestimated, while the relative humidity is overestimated. Furthermore, the finer resolution improves the flow field. The biases in temperature and relative humidity indicate problems with the surface water budget. The comparison between the 1 km simulations using 10 land-use classes and the new 36 surface cover classes shows that the biases are larger using the new 36 surface cover classes, likely due to the even larger values of initial soil water content in the new classes. This problem can partially be solved by choosing the initial soil water content according to preceding dry days, as described in Schlünzen (2012 in preparation).

The investigation of the simulated UHI, which is computed by subtracting the averaged temperatures of two rural grid points from each temperature value, shows that the intensity is lower than expected from the statistically modeled UHI. This is partially due to the different UHI definitions used for the statistical model (minimum temperature differences between single stations) and for the SDD (average night time temperature differences obtained from a 1x1 km^2 grid). Also, the simple representation of urban surfaces in the applied METRAS version seems a reasonable explanation for the low UHI intensity. Processes in the urban canopy layer and, more importantly, anthropogenic heat release are not parameterized. Thompson (2008) implemented BEP in METRAS to simulate the urban climate of London, which lead to an increase in the UHI of about 1 K (Grawe et al., 2012 submitted). The inclusion of anthropogenic heat in METRAS by Grawe et al. (2011) for Hamburg increased the UHI intensity by up to 1 K for one case study as well. In future studies both parameterizations could be included, because information about buildings within Hamburg became recently available (Schoetter et al., 2012 submitted).

The analysis of the statistically recombined UHI pattern shows that the maximum UHI intensity (~1.2 K) is located in the inner parts of the city, including harbor areas. The UHI pattern is largely affected by water surfaces. Hence, water temperatures seem to be crucial when simulating the local climate for Hamburg. At the moment river temperatures are set using interpolated SST data. In further studies measured river temperature data from the Wassergütemessnetz (WGMN) could be used (Fock, 2012 in preparation). The SDD method also assumes that the difference between water temperatures and air temperatures remains unchanged in the future climate. To verify this, a river model should be coupled with transient RCM projections.

The evaluation of the statistically recombined mean strong UHI (statistically modeled UHI ≥ 3 K) pattern for the present climate shows that it is well represented using the SDD technique. In particular the uncorrected METRAS results with 36 surface cover classes show good correlations with the observational datasets. However, the employed observational datasets have some deficiencies. The observed temperature differences taken from Schlünzen et al. (2010) are only available for five stations over one decade. The UHI pattern based on plant species data is probably only a measure for the climatolgically averaged temperature and not for the nocturnal UHI. Observations conducted in the HUSCO (Hamburg Urban Soil and Climate

Observatory) project (Sandoval et al., 2010) could be used for model validation in future studies. At the moment, only a few months of measurements are available. In the future, also mobile measurements, conducted on buses of Hamburg's public transport network will be available (Bechtel et al., 2012) and might help to determine the spatial distribution of the UHI.

The future UHI is computed by applying the SDD method to regional climate projections from different RCMs. Thereby it is assumed that the morphology of the city does not change in a future climate. Since this will not be the case, a projection of the future surface cover should be considered. Daneke (2012) developed a model for land-use changes of Hamburg. With the projected land-use converted to the METRAS surface cover classes, the UHI changes can be determined with consideration of morphological changes.

The UHI changes are determined for two 30-year periods. For the period 2036-2065 the changes in the UHI pattern as well as changes in the number of strong UHI days do not differ significantly using the REMO and CLM projections. However, both models show biases in the statistically modeled UHI due to biases in the model variables. These biases are partially eliminated by bias correction described by Schoetter et al. (2012). This bias correction is applied for all values within each month. However, it is not clear if the model biases are similar for different WPs. If this is not the case biases may be corrected for each WP separately.

The change in the UHI pattern is only slightly influenced by the bias correction. However, for strong UHI days the signal increased by +1 day for CLM. The changes in the signal can be expected since threshold based variables are sensitive to a change in the overall statistical distribution. For 2070-2099, CCAM projections for the A2 scenario were additionally available. For CCAM the pattern of the UHI changes. CCAM shows an increase in the western parts of Hamburg by up to 0.13 K. This corresponds to some 10% of the simulated maximum UHI intensity (1.2 K). The bias-corrected CLM results show similar changes, all other changes are small. The results also indicate that the pattern of the changes is affected by non-urban effects of individual simulations such as large-scale temperature gradients, probably due to the small number of simulations (13). The increase in the UHI intensity in CLM and CCAM is caused by an increase of UHI values within WP4 (large meridional pressure gradient and advection of dry air masses) and an increase in the frequency of WP4. The number of strong UHI days in CLM and CCAM increases significantly by up to 7.2 days per year. The increase of 3.6 days for REMO is not significant. Nevertheless, together with the findings of Hoffmann et al. (2011; Chapter 3 of this thesis), who show that the UHI days > 4 K increase significantly (by using a statistical UHI model in combination with the first realization of CLM), the results point to an occurrence of more strong UHI days in summer in the end of the 21st century.

6 Conclusions and Outlook

In this study different downscaling methods are applied to quantify Hamburg's urban heat island (UHI) in present and future climate. The observed UHI is defined here as the difference of minimum temperatures between one downtown and two rural stations. As mentioned by Stewart (2011), UHI definitions based on minima lack the synchrony of the measurements. This might lead to false estimations of the UHI, because temperature differences could be due to the different times at which they are measured. However, no long-term measurements with a higher temporal resolution (e.g. hourly) are available within the city. Therefore, the used definition is the best estimate of the UHI.

Based on tests with different meteorological variables a simple linear statistical model for the UHI has been constructed using DWD observations of relative humidity, cloud cover, and wind speed. The performance of the model is comparable with statistical models derived for other cities (e.g. Kim and Baik, 2004; Wilby, 2008). Since the model is based on a multiple linear regression, a linear relationship between the predictand and predictor is assumed. To account for non-linear effects, artificial neural networks could be used to construct a UHI model as done by Mihalakakou et al. (2002) for Athen's UHI.

Future changes in the UHI are analyzed by applying the statistical UHI model to regional climate projections of the A1B scenario simulated with the regional climate models (RCMs) REMO and CLM. Results for the reference period 1971-2000 reveal bias of the RCM data. In particular for CLM results the statistically modeled UHI is largely underestimated. An evaluation study by Schoetter et al. (2012) confirmed these findings. Cloud cover and relative humidity are overestimated by CLM, which leads to lower modeled UHI values. REMO only shows larger biases for relative humidity. With bias corrected RCM results derived with a quantile-mapping method described in Schoetter et al. (2012), more realistic values for the statistically modeled UHI are achieved. Hoffmann et al. (2010) show that the bias correction only slightly affects the climate change signal based on the statistical model. Following REMO only two months (April and December) show significant changes in the UHI, while the UHI remains unchanged for the rest of the year in both mid of the 21st century and end of the 21st century. CLM results show decreases except for the summer months July and August, where the UHI significantly increases (0.1-0.4 K) for both future periods.

The statistical downscaling does not give any information regarding spatial changes in the UHI. Therefore, an SDD method has been developed for Hamburg's UHI. The method is based on a combination of a weather pattern classification (WPC), a statistical model of the UHI and high-resolution (1 km) numerical simulations conducted with the mesoscale numerical model METRAS. Investigations realized within COST733 showed that no best WPC method exists (e.g. Huth, 2010; Beck and Philipp, 2010; Cahynová and Huth, 2010) and that the WPC should be constructed with respect to the target variable (Huth et al., 2008). Hence, a WPC focused on Hamburg's UHI has been constructed. This is done by testing different *k*-means based cluster algorithm, different classification domains and variables using ERA40 reanalysis data. The problem to determine the optimal cluster number is addressed by applying different statistical measures. Nevertheless, in some cases the cluster number still has to be set subjectively, e.g. if different measures give different optimal values. To avoid seasonality of the resulting WPs the WPC is constructed for each season separately. The final WPC is constructed by clustering the 700 hPa ERA40 fields of four different variables simultaneously (geopotential height, relative humidity, relative vorticity, and thickness). These WPs are than determined in the A1B projections of REMO and CLM for summer. The frequency of the anticyclonic WP, which is associated with high UHI values, does not change in the future climate whereas the frequencies of two other WPs change significantly. The changes in the frequency of WPs are similar for both models at the end of the century. This might be due to the forcing GCM, which is the same for both RCMs. To verify the similarity in changes of the WPs, additional projections from different RCMs and different RCM-GCM simulations should be used. Such data are available from the ENSEMBLES project (van der Linden and Mitchell, 2009). In the present study the number of WPs is kept constant throughout the climate projection. However, new WPs might occur in the future (Belleflamme et al., 2011) or rare WPs might become more important (Kreienkamp et al., 2010). This could be investigated by clustering the RCM results for the present climate and the future climate separately or by clustering the whole time series of the climate projections.

The resulting 7 WPs for summer explain about 18.6% of the UHI variance, which is too small to identify relevant days for the UHI. Hence, a combination of WPC and statistical model is used to determine the relevant days for a strong UHI (statistically modeled UHI ≥ 3 K) that are simulated with METRAS. The simulations conducted in a two step nesting are forced by ECMWF analysis data. Since the high resolution data are only available from 2006 onwards, the relevant days are selected for summer in the period 2006-2010. For the SDD method it would be optimal, if the days would be selected from the period 1985-1999, since the statistical model as well as the simulations can be directly compared with observations from the downtown DWD station St. Pauli and the rural DWD station Grambek. However, to reach the resolution of 1 km using the ERA40 reanalysis as forcing additional nesting steps with a coarser scale model would have to be carried out, which would lead to considerable additional computing effort.

Using analysis data instead of RCM data as forcing allows evaluating how well METRAS simulated the individual situations. The evaluation of both 4 km and 1 km simulations show that METRAS performs well compared to other evaluations studies summarized by Schlünzen et al. (2012c). The positive bias in relative humidity and the negative bias in temperature are probably due to the too high initial soil water content given for the surface cover classes. The results could be improved by choosing the soil water content according to the number of preceding days without precipitation.

The mean strong summer UHI pattern has been computed by statically recombining the simulation results. The intensity of the resulting UHI is underestimated by 2-3 K compared to the statistically modeled UHI intensities. This is due to the different definitions of the numerically modeled UHI (average night time temperature differences) and the statistically modeled UHI (minimum temperature differences), the resolution of the model results (temperature values represent the temperature of a 1x1 km^2 grid), and due to the relative simple representation of urban surfaces. An urban canopy parameterization and anthropogenic heat are not included in the present simulations. Based on findings by Grawe et al. (2011) and Grawe et al. (2012 submitted) these differences are probably in the order of 1-2 K. Therefore, the implementation of anthropogenic heat and an urban canopy parameterization are more important than improving the SDD method. A large comparison study conducted by Grimmond et al. (2011) showed, however, that no single best parameterization exists and that either the net fluxes are well simulated or just of part of the energy balance (e.g. short wave radiation). Hence, it has to be carefully tested if the results with an urban parameterization are right for the right physical reasons.

In contrast to the UHI intensity, the UHI pattern is quite well represented using the SDD method. Significant correlations are found for the comparison of the UHI pattern, determined with the newly developed 36 surface cover classes: they correlate well with temperature observations within the city (Schlünzen et al., 2010) and with UHI proxies based on floristic mapping (Bechtel and Schmidt, 2011). However, both comparison datasets have their limitations. For an optimal evaluation a larger number of meteorological measurements within the city are needed. Within the next years such dataset will become available for Hamburg. For example, in the HUSCO project within the cluster of excellence CliSAP additional measurements in the urban areas are conducted (Sandoval et al., 2010). Furthermore, mobile measurements conducted on buses of Hamburg’s public transport network are currently carried out within CliSAP (Bechtel et al., 2012). The investigation of the UHI patterns of the single simulations reveals that some simulations are also quite good correlated with the observations (correlation coefficients of up to 0.7). However, the correlation coefficient for the statistically recombined pattern is still larger (0.74). This indicates that more than just one simulation should be conducted to obtain a representative UHI pattern.

An important outcome of the current study is that the simulated UHI pattern is also impacted by non-urban effects. Large water bodies such as the river Elbe or the Alster lake cool only slowly at night and affect their surroundings. Hence, the influence of water bodies should be further analyzed. Also the elevation differences within the city and the Geest hillside seem to have an effect on the nocturnal temperatures.

Results for the future UHI are conducted by applying the SDD method to regional climate projections from three RCMs. The climate signals are depending on the RCM used. REMO (A1B scenario) results indicate only a slight non-significant increase, whereas CLM (A1B scenario) results indicate larger increase for both mean UHI pattern and strong UHI days. For the end of the century, the mean strong UHI pattern increases up to 0.13 K (some 10% of the simulated maximum UHI intensity) in the western parts of Hamburg and the number of strong UHI (≥ 3K) days increases by 7.2 days. The regional climate projections from CCAM for the A2 scenario, which are forced by a different GCM, agree with the results from CLM (A1B scenario) for the end of the century.

For all applied downscaling methods it is assumed that the relationship between the UHI and the predictors (local variables and WPs) will not change in a future climate. This might not be valid, because it would assume that Hamburg itself will not change over the considered time span, which is unlikely. Daneke et al. (2011) shows that between 1960 and 2005 the urbanized area increased and, therefore, also the potential for the UHI. Changes in the city structure could be considered by simulating the relevant days with future projection of Hamburg’s surface cover produced by Daneke (2012 in preparation). If anthropogenic heat will be included in the simulations scenarios for the future energy consumption have to be developed as well.

From the results of both downscaling methods it can be concluded that the UHI remains unchanged in the future or even increases for the summer months in the A1B scenario, if Hamburg does not change. These findings are in agreement with studies conducted for the UHI of London (Wilby, 2003; 2008, increase) or New Jersey (Rosenzweig et al., 2005, unchanged) UHI. In addition, Früh et al. (2011a,b) show that Frankfurt am Main itself does not have an influence on the climate change signal for summer days ($T_{max} \geq 25$°C) as well as beergarden days (T at 8 pm ≥ 20 K). For Hamburg these results imply that in addition to the temperature increase of about 2-3 K (Daschkeit, 2011) projected for Northern Germany at the end of the century also the UHI effect has to be considered. It will not be reduced in a future climate but be at least as intense as today when focusing on the summer season. Thus, the number of tropical nights ($T_{min} \geq 20$°C) could increase due to the presence of the UHI, which should be investigated further. On the other hand, the persistence of the UHI in a future climate opens opportunities for climate change adaptation. By reducing the UHI of Hamburg, climate changes can at least in the currently very warm parts of the city of Hamburg be partially mitigated.

The present study only focused on the Hamburg's UHI. Yet, the conducted simulations could be analyzed with respect to the urban impact on the humidity as well. The meteorological conditions favorable for the UHI are similar to the conditions favorable for the so-called urban moisture excess (UME) (e.g. Kuttler et al., 2007). With regard to climate adaptation it is also helpful to analyze biometeorological indices such as the perceived temperature (PT; Jendritzky et al., 2000; Staiger et al., 2011), the physiological equivalent temperature (PET; Höppe, 1999) or the newly developed universal thermal climate index (UTCI; Kampmann and Bröde, 2009; Blazejcyk et al., 2011; Kampmann et al., 2011). Currently, 250 m simulations with METRAS, downscaled from the 1 km simulations conducted in this study, are offline-coupled with building energy parameterization (BEP) and analyzed with respect to PT by Schoetter et al. (2012 submitted).

The downscaling methods for the UHI developed in this study can also be applied to other cities, if there are observations available within the urban areas. Otherwise, a statistical UHI model cannot be constructed. The meteorological variables used for a statistical model might differ for cities in different climates. Consequently, the necessary variables need to be identified before constructing a statistical model. Also the variables used to classify the WPs may be different, especially in the tropics, where the wind patterns are more important than the pressure or geopotential height patterns. To conduct numerical simulations for other cities high-resolution land-use or surface cover data should be available.

Using the general concept of the developed SDD method, downscaling methods for other variables such as wind or precipitation. Both a new WPC and a new measure for the strength of the variables would have to be determined. For wind speed local wind observations could be used to subdivide the WPs according to the strength of the wind (Najac et al., 2011). For precipitation convective indices such as convective available potential energy (CAPE) or moisture measures such as precipitable water (PW) could be used. Martens (2012) used the WPC, constructed in this study, to simulate the climatological spring for Northern Germany for the period 1982-2011. He simulated only the situations which are closest to the cluster center of each WP. The comparison with DWD observations shows a good agreement for the selected days, but little agreement with the climatological frequency distribution. The number of simulations was too low to capture the frequency distribution of the climate variables. Najac et al. (2011) also showed that the number of simulations is important for the results of a SDD method. Hence, if the whole distribution of the target variable is of interest the number of situation should be larger than in the present study.

Danksagung

Hiermit möchte ich mich herzlich bei meiner Betreuerin Frau Prof. K. Heinke Schlünzen für die großartige Unterstützung bedanken. Im Verlaufe meiner Diplom- und Doktorarbeit hat sie in mir die Lust am wissenschaftlichen Arbeiten geweckt. Sie hat es mir auch ermöglicht meine Ergebnisse auf verschiedenen Tagungen zu präsentieren. Des Weitern möchte ich mich für die interessanten Diskussionen und für die Anmerkungen zu der vorliegenden Arbeit bedanken. Weiterer Dank gilt meinem zweiten Betreuer Prof. Felix Ament. Seine Anmerkungen haben mir geholfen meine Methodik kritisch zu hinterfragen und sie dadurch zu verbessern. Bei Oliver Krüger möchte ich mich für die tolle Zusammenarbeit und für die vielen hilfreichen Kommentare zu meiner Arbeit bedanken. Dr. Jack Katzfey möchte ich für die interessanten Diskussionen über Downscalingmethoden sowie das Bereitstellen der CCAM Daten bedanken. Für die Bereitstellung der REMO Daten bedanke ich mich bei Thomas Raub. Michael Haller möchte ich danken für Durchführung einiger METRAS-Simulation, welche in dieser Arbeit verwendet wurden. Für die Bereitstellung der UHIE Daten möchte ich mich bei Benjamin Bechtel bedanken. Ich möchte mich auch bei den aktuellen und ehemaligen Mitgliedern der MeMi-Gruppe bedanken. Besonderer Dank gilt dabei Robert Schoetter, Peter Kirschner, Marita Linde, David Flagg, Malte Uphoff und Michael Martens. Für die hilfreichen Kommentare zu meiner Arbeit möchte ich mich des Weiteren bei Karsten Peters, David Grawe, Nadine Schneider und Katharina Lengfeld bedanken. Den Mädels der Arbeitsgruppe „Synthese von Beobachtungen und Modellen“ danke ich für die aufmunternden Teepausen.

Ein riesen Dank gilt meiner Freundin Anja. Sie hat mich immer unterstützt, vor allem in schwierigen Phasen meiner Doktorarbeit.

Zuletzt noch ein großes Dankeschön an meine Eltern Sylvia und Harry sowie an meine Familie. Sie haben mich auf meinen bisherigen Lebensweg in jeder Hinsicht unterstützt und mir Kraft gegeben mein Studium sowie meine Doktorarbeit durchzuziehen.

Die vorliegende Arbeit wurde im Rahmen des KLIMZUG-NORD Projekts (Födernummer 01LR0805D), welches vom Bundesministerium für Bildung und Forschung (BMBF) gefördert wird, durchgeführt. Die verwendeten REMO-Simulationen wurden im Auftrag des Umwelt Bundesamts (UBA), der Bundesanstalt für Gewässerkunde (BFG) sowie KLIMZUG-NORD durchgeführt. Die REMO und CLM Daten wurden teilweise von der CERA-Datenbank heruntergeladen. Die verwendeten Messdaten wurden freundlicherweise vom Deutschen Wetterdienst (DWD) zur Verfügung gestellt.

METRAS verwendete als Eingabegrößen digitale Geländemodelle, ATKIS-Daten, für Hamburg zudem die Digitale Stadtgrundkarte (DSGK) sowie 3D-Stadtmodelldaten (LoD 2). Die Daten wurden von der Freien und Hansestadt Hamburg, Landesbetrieb für Geoinformation und Vermessung (Nr. 102156), dem Landesamt für Geoinformation und Landentwicklung Niedersachsen (LGN), dem Landesvermessungsamt Schleswig Holstein, dem Am für Geoinformation, Vermessung- und Katasterwesen Mecklenburg-Vorpommern beschafft. Ein Dank an die Universität Hamburg und das Excellenz Cluster CliSAP, die die Beschaffung der Daten mit erheblichen Mitteln finanziell unterstützt haben.

List of relevant Symbols

a	-	parameter of the (multiple) linear regression
a_f	-	parameter used to calculate the nudging coefficient
b	-	parameter of the (multiple) linear regression
$BIAS$	-	average deviation of model results and measurements
c	-	parameter of the multiple linear regression
CC	-	cloud cover
C_i	-	ith cluster
CO	-	cooling rate
$CORR$	-	correlation
cov	-	covariance
c_p	-	heat capacity
d	-	parameter of the multiple linear regression
D	-	uncertainty range
$Diff_{\max}$	-	average difference between $(\Delta T_{u-r})_{\max}$ and ΔT_{u-r}
$Diff_{Thres}$	-	average difference between $(\Delta T_{u-r})_{Thres}$ and ΔT_{u-r}
ECV	-	explained cluster variance
ED	-	Euclidian distance
ED_{new}	-	Euclidian distance to the new cluster
ED_{old}	-	Euclidian distance to the old cluster
f	-	Coriolis parameter
$f(WP)_c$	-	weather pattern frequency in current climate
$f(WP)_f$	-	weather pattern frequency in future climate
FF	-	wind speed
GP	-	geopotential height
h_θ	-	depth of the daily temperature wave
$HITR$	-	hitrate
I_∞	-	solar constant
k	-	cluster number/ weather pattern number
k_s	-	thermal diffusivity
K	-	maximum number of clusters
K_{vert}	-	vertical exchange coefficient for momentum
$K_{vert,S}$	-	vertical exchange coefficient for scalar quantities
l_{21}	-	enthalpy of vaporization
l_n	-	mixing length for neutral stratification
L	-	Monin-Obukhov length
$\overline{M}$	-	model mean

Max_{Corr}	-	maximum of correlation between the cluster centers
M_i	-	ith model result
Min_{SED}	-	maximum of the squared Euclidian distance between the cluster centers
N	-	sample size and number of resampling steps
N_f	-	parameter used to calculate the nudging coefficient
N_{strong}	-	number of strong UHI days (statistically modeled UHI ≥ 3 K)
$\overline{O}$	-	observation mean
O_i	-	ith observation
P	-	acceptance probability
$\overline{q}_1^1$	-	specific humidity
$\overline{q}_{1s}^1$	-	specific humidity at the surface
$\overline{q}_{1sat}^1$	-	saturated value of specific humidity
q_*	-	scaling value for specific humidity
R^2	-	explained variance
RH	-	relative humidity
Ri	-	Richardson number
$RMSE$	-	root mean square error
SED	-	squared Euclidian distance
T	-	temperature
TH	-	relative thickness between 1000 hPa and 700 hPa
$T_{\min}$	-	daily minimum temperature
T_S	-	surface temperature
$\overline{T}_s(-h_0)$	-	deep soil temperature
TSS	-	total sum of squares
u	-	velocity in east-west direction
u_*	-	friction velocity
v	-	velocity in north-south direction
var	-	variance
VO	-	relative Vorticity
w	-	vertical wind component
W_K	-	saturated soil moisture availability
$W_{\max}$	-	weightings for the maximum urban heat island day
WSS	-	within-cluster sum of squares
W_{Thres}	-	weightings for the threshold urban heat island day
$\boldsymbol{x}$	-	data object
X	-	meteorological variable
$\boldsymbol{z}$	-	cluster centroid

z	-	height
Z	-	Fisher z transformed correlation
$\overline{Z}$	-	average Fisher z transformed correlation
$Z(t)$	-	zenith angle
z_0	-	roughness length
α	-	significance level
α_0	-	Albedo
α_q	-	bulk soil water availability
δ	-	weighting factor
Δt	-	model time step
ΔT_{u-r}	-	urban-rural temperature differences
$(\Delta T_{u-r})_{WP}$	-	average ΔT_{u-r} per WP
$(\Delta T_{u-r})_{\max}$	-	maximum ΔT_{u-r}
$(\Delta T_{u-r})_{Thres}$	-	threshold ΔT_{u-r}
ΔWP	-	change of weather pattern frequency
ε	-	modeled unexplained variance
$\hat{\varepsilon}$	-	correction factor for radiative flux at the surfaces
θ_*	-	scaling value for temperature
κ	-	von Karman constant
μ	-	parameter in the shortwave radiation budget
v	-	nudging factor
v_0	-	initial nudging factor
v_S	-	thermal conductivity
σ	-	Stefan-Boltzmann constant
σ_M	-	standard deviation of model results
σ_O	-	standard deviation of observations
Φ_h	-	stability function for scalar quantities
Φ_m	-	stability function for momentum
Ψ_f	-	model variable after forcing
Ψ_l	-	variable of forcing data
Ψ_m	-	model variable
ρ_0	-	density of the air

List of Abbreviations

A1B	-	SRES emission scenario
A2	-	SRES emission scenario
AH	-	Ahrensburg-Wulsdorf (DWD station)
AR(1)	-	first order autoregressive process
ATKIS	-	Official Topographic-Cartographic Information System
BEP	-	building energy parameterization
CAPE	-	convective available potential energy
CC	-	cluster center
CCAM	-	Conformal Cubic Atmospheric Model
CliSAP	-	Integrated Climate System Analysis and Prediction
CLM	-	Climate Local Model
DWD	-	Deutscher Wetterdienst (German Meteorological Service)
ECHAM4	-	4^{th} generation European Centre/Hamburg Model
ECHAM5	-	5^{th} generation European Centre/Hamburg Model
ECMWF	-	European Centre for Medium-Range Weather Forecasts
EIT	-	Ellenberg indicator values for temperature
EM	-	Europa-Modell
ERA40	-	40-year ECMWF re-analysis
ERA-INT	-	ERA-Interim re-analysis
FU	-	Hamburg-Fuhlsbüttel (DWD station)
GCM	-	global climate model
GFDLcm2.0	-	Geophysical Fluid Dynamics Laboratory coupled model 2.0
GLS	-	generalized least squares
GR	-	Grambek (DWD station)
HadSST	-	Met Office Hadley Centre's sea ice and sea surface temperature dataset
HH	-	Hansestadt Hamburg (Hanseatic City of Hamburg)
HUSCO	-	Hamburg Urban Soil and Climate Observatory
IMGW	-	Institute of Meteorology and Water Management
KNMI	-	Royal Netherlands Meteorological Institute
LAM	-	local area model
LM	-	Lokal-Modell
LST	-	local sun time
METRAS 1km	-	METRAS with 1 km horizontal resolution
METRAS 4km	-	METRAS with 4 km horizontal resolution
METRAS	-	Mesocale Transport and Fluid Model
METRAS-10	-	METRAS using 10 land-use classes
METRAS-36	-	METRAS using 36 surface cover classes
MPI	-	Max-Planck-Institute for Meteorology
MPIOM	-	Max-Planck-Institute Ocean Model

NE	-	Hamburg-Neuwiedenthal (DWD station)
NOAA	-	National Oceanic and Atmospheric Administration
OISST	-	Optimum Interpolation Sea Surface Temperature Analysis
OLS	-	ordinary least squares
PET	-	physiological equivalent temperature
PT	-	perceived temperature
PW	-	precipitable water
RCM	-	regional climate model
REMO	-	Regional Model
SANDRA	-	simulated annealing and diversified randomization
SDD	-	statistical-dynamical downscaling
SP	-	Hamburg-St. Pauli (DWD station)
SRES	-	Special Report on Emissions Scenarios
SST	-	sea surface temperature
STAR	-	statistical analogue resampling scheme
SYNOP	-	meteorological station with hourly measurements
TEB	-	town energy budget
UHI	-	urban heat island
UHIE	-	Ellenberg based urban heat island values
UME	-	urban moisture excess
UTC	-	universal time coordinated
UTCI	-	universal thermal climate index
WA	-	Hamburg-Wandsbek (DWD station)
WETTREG	-	Wetterlagen-basierte Regionalisierungsmethode
WGMN	-	Hamburger Wassergütemessnetz
WMO	-	World Meteorological Organization
WP	-	weather pattern
WPC	-	weather pattern classification
WRF	-	Weather Research and Forecast Model

References

Alonso MS, Fidalgo MR, Labajo JL. 2007. The urban heat island in Salamanca (Spain) and its relationship to meteorological parameters. *Clim. Res.* **34**: 39–46.

Arnfield J. 2003. Two decades of urban climate research: A review of turbulence, exchanges of energy and water, and the urban heat island. *Int. J. Climatol.* **23**: 1–26.

Atkinson BW. 2003. Numerical modelling of urban heat-island intensity. *Bound.-Layer Meteorol.* **109**: 285–310.

Augustin W, Heuveline V, Meschkat G, Schlünzen KH, Schroeder G. 2008. Open MP parallelization of the METRAS meteorology model: Application to the America's Cup. *Springer Berlin Heidelberg*, High Performance Computing in Science and Engineering, Springer-Verlag, Berlin, Germany: 547–559.

Barstad I, Sorteberg A, Flatøy F, Déqué M. 2009. Precipitation, temperature and wind in Norway: dynamical downscaling of ERA40. *Clim. Dyn.* **33**: 769–776. DOI 10.1007/s00382-008-0476-5

Bechtel B, Daneke C. 2011. Classification of local climate zones based on multiple earth observation data. IEEE J*ournal of Selected Topics in Applied Earth Observations and Remote Sensing* accepted

Bechtel B, Langkamp T, Böhner J, Daneke C, Oßenbrügge J, Schempp S. 2012. Classification and modelling of urban micro-climates using multisensoral und multitemporal remote sensing data. *Procedings of the XXII Congress of the International Society for Photogrammetry and Remote Sensing, Melbourne, Australia*.

Bechtel B, Schmidt KJ. 2011. Floristic mapping data as a new proxy for the mean urban heat island. *Climate Research* **49**: 45–58. doi: 10.3354/cr01009.

Beck C, Philipp A. 2010. Evaluation and comparison of circulation type classifications for the European domain. *Phys. Chem. Earth* **35**: 374–387.

Beck C. 2011. Monthly mean PM10 concentrations in Augsburg (Germany) and their relation to large-scale atmospheric circulation types. *Geophysical Research Abstracts* **13**: EGU2011-12920.

Bejaran RA, Camilloni IA. 2003. Objective method for classifying air masses: an application to the analysis of Buenos Aires' (Argentina) urban heat island intensity. *Theor. Appl. Climatol.* **74**: 93–103.

Belleflamme A, Fettweis X, Erpicum M. 2011. Evaluation of the present and future general circulation over western Europe simulated by the IPCC AR5/CMIP5 GCMs with the help of a circulation type classification. *Geophysical Research Abstracts* **13**: EGU2011-7352.

Beranová R, Huth R. 2005. Long-term changes in the heat island of Prague under different synoptic conditions. *Theor. Appl. Climatol.* **82**: 113–118

Bissolli P, Grieser J, Dotzek N, Welsch M. 2007. Tornadoes in Germany 1950–2003 and their relation to particular weather conditions. *Glob. Planet. Change* **57**: 124–138.

Blackadar AK. 1962. The vertical distribution of wind and turbulent exchange in a neutral atmosphere. *J. Geophys. Res.* **67**: 3095–3102.

Blazejcyk K, Epstein Y, Jendritzky G, Staiger H, Tinz B. 2011. Comparison of UTCI to selected thermal indices. *Int. J. Biometeorol.*: DOI 10.1007/s00484-011-0453-2.

Boé J, Terray L, Habets F, Martin E. 2006. A simple statistical-dynamical downscaling scheme based on weather types and conditional resampling, *J. Geophys. Res.* **111**: D23106. doi:10.1029/2005JD006889.

Boé J, Terray L. 2008. A weather-type approach to analyzing winter precipitation in France: Twentieth-century trends and the role of anthropogenic forcing. *J. Climate* **21**: 3118–3133.

Böhm U, Kücken M, Ahrens W, Block A, Hauffe D, Keuler k, Rockel B. Will A. 2006. CLM - the climate version of LM: brief description and long-term applications. *COSMO Newslett.* **6**: 225–235.

Bohnenstengel SI., Evans S, Clark PA, Belcher S. 2011. Simulations of the London urban heat island. *Q.J.R. Meteorol. Soc.* **137**: 1625–1640. doi: 10.1002/qj.855

Bohnenstengel SI. 2011. *Can a simple locality index be used to improve mesoscale model forecasts?* Department Geowissenschaften, Universität Hamburg. Ph.D. thesis.

Buschbom J, Gimmerthal S, Kirschner P, Michalczyk IM, Sebbenn, Schueler S, Schlünzen KH, Degen B. 2012. Spatial composition of pollen-mediated gene flow in sessile oak. *Archive of Forest Science* **83**: 12–18.

Bungert U. 2008. *Einfluss der Nestung auf die Ergebnisse meteorologischer Modelle*. Ph.D. thesis, Dept. Geowissenschaften, Universität Hamburg: 134 pp.

Cahynová M, Huth R. 2010. Circulation vs. climatic changes over the Czech Republic: A comprehensive study based on the COST733 database of atmospheric circulation classifications. *Phys. Chem. Earth* **35**: 422–428.

Cassou C, Minvielle M, Terray L, Périgaud C. 2011. A statistical-dynamical scheme for reconstructingocean forcing in the Atlantic. Part I: weather regimes as predictors for ocean surface variables. *Clim. Dyn*. **36**: 19–39. doi:10.1007/s00382-010-0781-7.

Charnock H. 1955. Wind stress on a water surface. *Quart. J. Roy. Meteor. Soc.* **81**: 639–640.

Chouinard C, Beland M, McFarlane N. 1986. A simple gravity wave drag parametrization for use in medium-range weather forecast models. *Atmos. Ocean*. **24**: 91–110.

Christiansen B. 2007. Atmospheric circulation regimes: Can cluster analysis provide the number? *J. Climate* **20**: 2229–2250.

Claussen M. 1991. Estimation of arealy-averaged surface fluxes. *Bound.-Layer Metorol.* **54**: 387–410.

Cochrane D, Orcutt GH. 1949. Application of least squares regression to relationships containing autocorrelated error terms. *J. Am. Stat. Assoc.* **44**: 32–61.

Côté J, Gravel S, Méthot A, Patoine A, Roch M, Staniforth A. 1998. The Operational CMC–MRB Global Environmental Multiscale (GEM) Model. Part I: Design Considerations and Formulation. *Mon. Wea. Rev.* **126**: 1373–1395.

Courtier P, Geleyn J-F. 1988. A global numerical weather prediction model with variable resolution: Application to the shallow-water equations. *Quart. J. Roy. Meteor. Soc.* **114:** 1321–1346.

Cox R, Bauer BL, Smith T. 1998. A mesoscale model intercomparison. *Bull. Amer. Meteor. Soc.* **79**: 265–283, doi: http://dx.doi.org/10.1175/1520-0450(1981)020<0203:AACC>2.0.CO;2.

Curry CL, van der Kamp D, Monahan AH. 2011. Statistical downscaling of historical monthly mean winds over a coastal region of complex terrain. I. Predicting wind speed. *Climate Dynamics* 38: 1281-1299, DOI: 10.1007/s00382-011-1173-3.

D'onofrio A, Boulanger J-P, Segura E. 2010. CHAC: A weather pattern classification system for regional climate downscaling of daily precipitation. *Climatic Change* **98**: 405–427. doi:10.1007/s10584-009-9738-4.

Daneke C. 2012. *Landnutzungsmodellierung im Kontext der Stadtklimaforschung am Fallbeispiel Hamburg.* Ph.D. thesis *in preparation*

Daneke C, Bechtel B, Böhner J, Langkamp T, Oßenbrügge J. 2011. Conceptual approach to measure the potential of urban heat islands from landuse datasets and landuse projections. *Lecture Notes in Computer Science, Springer accepted*

Davies HC. 1976. A lateral boundary formulation for multi-level prediction models. *Q. J. R. Meteorol. Soc.* **102**: 405–418.

Daschkeit A. 2011. in von Storch H, Claussen M (Hrsg.). *Klimabericht für die Metropolregion Hamburg*: 61–90. DOI 10.1007/978-3-642-16035-6, Springer 2011.

Deardorff JW. 1978. Efficient prediction of ground surface temperature and moisture, with inclusion of a layer of vegetation. *J. Geophys. Res.-Atmos.* **83**: 1889–1903.

Dee DP, Uppala SM, Simmons AJ, Berrisford P, Poli P, Kobayashi S, Andrae U, Balmaseda MA, Balsamo G, Bauer P, Bechtold P, Beljaars ACM, van de Berg L, Bidlot J, Bormann N, Delsol C, Dragani R, Fuentes M, Geer AJ, Haimberger L, Healy SB, Hersbach H, Hólm EV, Isaksen L, Kållberg P, Köhler M, Matricardi M, McNally AP, Monge-Sanz BM, Morcrette J-J, Park B-K, Peubey C, de Rosnay P, Tavolato C, Thépaut J-N, Vitart F. 2011. The ERA-Interim reanalysis: configuration and performance of the data assimilation system. *Q.J.R. Meteorol. Soc.* **137**: 553–597. doi: 10.1002/qj.828.

Delworth TL, Broccoli AJ, Rosati A, Stouffer RJ, Balaji V, Beesley JA, Cooke WF, Dixon KW, Dunne J, Dunne KA, Durachta JW, Findell KL, Ginoux P, Gnanadesikan A, Gordon CT, Griffies SM, Gudgel R, Harrison MJ, Held IM, Hemler RS, Horowitz LW, Klein SA, Knutson TR, Kushner PJ, Langenhorst AR, Lee H-C, Lin S-J, Lu J, Malyshev SL, Milly PCD, Ramaswamy V, Russell J, Schwarzkopf MD, Shevliakova E, Sirutis JJ, Spelman MJ, Stern WF, Winton M, Wittenberg AT, Wyman B, Zeng F, Zhang R. 2006. GFDL's CM2 global coupled climate models. Part I: formulation and simulation characteristics. Journal of Climate **19**: 643–674. DOI: 10.1175/JCLI3629.1.

Demuzere M, Kassomenos P, Philipp A. 2010. The COST733 circulation type classification software: an example for surface ozone concentrations in Central Europe. *Theor. Appl. Climatol.* **105**: 143–166, DOI: 10.1007/s00704-010-0378-4.

Demuzere M, van Lipzig NPM. 2010. A new method to estimate air-quality levels using a synoptic regression approach: Part I: present-day O3 and PM10 analysis. *Atmos. Environ.* **44**: 1341–1355.

Demuzere M, Werner M, van Lipzig NPM, Roeckner E. 2009. An analysis of present and future ECHAM5 pressure fields using a classification of circulation patterns. *Int. J. Climatol.* **29**: 1796–1810.

Dickinson RE, Errico RM, Giorgi F, Bates GT. 1989. A regional climate model for western United States. *Clim. Change* **15**: 383–422.

Dierer S, Schlünzen KH. 2005. Influence parameters for a polar mesocyclone development. *Meteorol. Zeitschr.* **14**: 781–792.

ECMWF. 2009. PART II: DATA ASSIMILATION. *IFS DOCUMENTATION – Cy33r1 Operational implementation 3 June 2008*: 160 pp.

ECMWF. 2010. PART II: DATA ASSIMILATION. *IFS DOCUMENTATION – Cy36r1 Operational implementation 26 January 2010*: 168 pp.

Efron T, Tibshirani R. 1993. An introduction to the bootstrap. Chapman and Hall: 436 pp.

Enke W, Spekat A. 1997. Downscaling climate model outputs into local and regional weather elements by classification and regression. *Climate Res.* **8**: 195–207.

Faller AJ. 1981. An average correlation coefficient. *J. Appl. Meteor.* **20**: 203–205.

Fereday DR, Knight JR, Scaife AA, Folland CK. 2008. Cluster analysis of North Atlantic–European circulation types and links with tropical Pacific sea surface Temperatures. *J. Climate* **21**: 3687–3703.

Flagg DD. 2010. *Mesoscale modeling of the urban boundary layer in a coastal environment.* Ph.D. thesis, York University, Toronto, Ontario: 250 pp.

Flagg DD, Schoetter R, Linde M, Kirschner P, Grawe D, Schlünzen KH. 2011. Development of surface cover classes for the M-SYS models from land-use land-cover datasets. CLiSAP D4 Workshop, University of Hamburg, Hamburg, Germany. 17 November 2011.

Fock BH. 2012. *RANS versus LES models for investigation of the urban climate*. Ph.D. thesis *in preparation*

Frey-Buness F, Heimann D, Sauses R. 1995. A statistical-dynamical downscaling procedure for global climate simulations. *Theoretical and Applied Climatology* **50**: 117–131.

Früh B, Becker P, Deutschländer T, Hessel J-D, Kossmann M, Mieskes I, Namyslo J, Roos M, Sievers U, Steigerwald T, Turau H, Wienert U .2011a: Estimation of Climate-Change Impacts on the Urban Heat Load Using an Urban Climate Model and Regional Climate Projections. *J. Appl. Meteor. Climatol.* **50**: 167–184.

Früh B, Koßmann M, Roos M. 2011b. Frankfurt am Main im Klimawandel - Eine Untersuchung zur städtischen Wärmebelastung. *Berichte des Deutschen Wetterdienstes* **237**: 68 pp.

Fuentes U, Heimann D. 2000. An improved statistical-dynamical downscaling scheme and its application to the Alpine precipitation climatology. *Theor. Appl. Climatol.* **65**: 119–135.

Gedzelman SD, Austin S, Cermak R, Stefano N, Partridge S, Quesenberry S, Robinson DA. 2003. Mesoscale aspects of the urban heat island around New York City. *Theoretical and Applied Climatology* **75**: 29–42.

Gerstengarbe F, Werner PC. 1997. A method to estimate the statistical confidence of cluster separation. *Theor. Appl. Climatol.* **57:** 103–110.

Giorgi F. 1990. Simulation of regional climate using a limited-area model nested in a general circulation model. *J. Climate* **3**: 941–963.

Giorgi F, Coppola E, Solmon F, Mariotti L, Sylla MB, Bi X, Elguindi N, Diro GT, Nair V, Giuliani G, Turuncoglu UU, Cozzini S, Güttler I, O'Brien TA, Tawfik AB, Shalaby A, Zakey AS, Steiner AL, Stordal F, Sloan LC, Brankovic C. 2012. RegCM4: model description and preliminary tests over multiple CORDEX domains. *Clim. Res.* **52**: 7–29.

Goyal MK, Burn DH, Oiha CSP. 2011. Evaluation of machine learning tools as a statistical downscaling tool: temperatures projections for multi-stations for Thames River Basin, Canada. *Theor. Appl. Climatol.*: DOI 10.1007/s00704-011-0546-1.

Grachev AA, Andreas EL, Fairall CW, Guest PS, Persson POG. 2012. The critical Richardson number and limits of applicability of local similarity theory in the Stable Boundary Layer. submitted to *Bound.-Layer Meteorol.*

Grawe D, Thompson HL, Salmond J, Cai X-M, Schlünzen KH. 2010. Coupling of mesoscale meteorological model METRAS with an improved urban parameterisation. *Proceedings of the Fifth International Symposium on Computational Wind Engineering.* Chapel Hill, USA. http://www.cwe2010.org/abstracts.html

Grawe D, Thompson HL, Salmond JA, Cai XM, Schlünzen KH. 2012. Modelling the impact of urbanisation on the regional climate of the Greater London Area. submitted to *Int. J. Climatol.*

Grawe D, Bungert U, Schlünzen KH. 2011. Modelling the urban heat island of Hamburg considering anthropogenic heat release. 11th EMS Annual Meeting, 12.-16.09.2011, Berlin, Germany.

Grimmond CSB, Blackett M, Best MJ, Baik J-J, Belcher SE, Beringer J, Bohnenstengel SI, Calmet I, Chen F, Coutts A, Dandou A, Fortuniak K, Gouvea ML, Hamdi R, Hendry M, Kanda M, Kawai T, Kawamoto Y, Kondo H, Krayenhoff ES, Lee S-H, Loridan T, Martilli A, Masson V, Miao S, Oleson K, Ooka R, Pigeon G, Porson A, Ryu Y-H, Salamanca F, Steeneveld G, Tombrou M, Voogt JA, Young DT, Zhang N. 2011. Initial results from Phase 2 of the international urban energy balance model comparison. *Int. J. Climatol.* **31**: 244–272. doi: 10.1002/joc.2227

Guentchev GS, Winkler JA. 2010. A two-tier atmospheric circulation classification scheme for the European–North Atlantic region. *Phys. Chem. Earth* **35**: 341–351. doi: 10.1016/j.pce.2009.12.011.

Hafner J, Kidder SQ. 1999. Urban heat island modeling in conjunction with satellite-derived surface/soil parameters. *J. Appl. Meteor.* **38**: 448–465.

Haller M, Schlünzen KH, Finardi S, Grawe D, Hoffmann P, Pandis S, Prank M, Reinhardt V, Ross O, Silibello C, Siour G, Sofiev M, Sokhi R, Theloke J, Uphoff M. 2012. Evaluation of air quality model results for different concentration measures. *in preparation*

Hebbinghaus H, Dierer S, Schlünzen KH. 2007. Sensitivity studies on vortex development over a polynya. *Theoretical and Applied Climatology* **88**: 1–16. doi: 10.1007/s00704-006-0233-9.

Herbert F, Kramm G. 1985. Trockene Deposition reaktionsträger Substanzen, beschrieben mit einem diagnostischen Modell der bodennahen Luftschicht. Published in: Beder KH, Löbel G (Eds): *Atmosphärische Spurenstoffe und ihr physikalisch-chemisches Verhalten.* Springer Verlag, Berlin: 264 pp.

Herrmann K. 1994. Zum Gültigkeitsbereich des Konzepts der Blendhöhe in einem mesoskaligen Modell - Ein Beitrag zur Parametrisierung bodennaher Flüsse. *Diplomarbeit, Fachbereich Physik, Universität Hamburg*.

Hjemfelt MR. 1982. Numerical simulation of the effects of St. Louis on mesoscale boundary layer airflow and vertical motion: Simulations of urban vs. non-urban effects. *J. Appl. Meteor.* **21**: 1239–1257.

Hoffmann P, Krueger O, Schlünzen KH, Schoetter R. 2010. Statistical downscaling of the urban heat island of Hamburg using a statistical model and regional climate model results. Abstract GC51A-0744 presented at 2010 Fall Meeting, AGU, 13.-17.12.2010, San Francisco, Calif.

Hoffmann P, Krueger O, Schlünzen KH. 2011. A statistical model for the urban heat island and its application to a climate change scenario. *Int. J. Climatol.* doi: 10.1002/joc.2348.

Hoffmann P, Schlünzen KH, Rosenhagen G. 2009. Observational study of the urban heat island and the urban impact on precipitation. *Seventh International Conference on Urban Climate (ICUC-7)*, Yokohama, Japan. http://www.ide.titech.ac.jp/~icuc7/extended_abstracts/pdf/383147-1-090515172626-002.pdf

Hoffmann P, Schlünzen KH. 2012. Weather patterns and their relation to the urban heat island in present and future climate. *Journal of Applied Meteorology and Climatology in review*

Hoffmann P. 2009. *Modifikation von Starkniederschlägen durch urbane Gebiete*. Diploma thesis, Meteorologisches Institut Department Geowissenschaften Universität Hamburg: 111 pp.

Hollweg H-D, Böhm U, Fast I, Hennemuth B, Keuler K, Keup-Thiel E, Lautenschlager M, Legutke S, Radtke K, Rockel B, Schubert M, Will A, Woldt M, Wunram C. 2008. *Ensemble simulations over Europe with the regional climate model CLM forced with IPCC AR4 global scenarios. M & D Technical Report 3*: 154 pp.

Holtslag AAM, Boville BA. 1993. Local versus non-local boundary layer diffusion in a global climate model. *J. Climate* **6:** 1825–1842.

Höppe P. 1999. The physiological equivalent temperature—a universal index for the biometeorological assessment of the thermal environment. *Int. J. Biometeor.* **43**: 71–75.

Huebener H, Kerschgens M. 2007a. Downscaling of current and future rainfall climatologies for southern Morocco. Part I: Downscaling method and current climatology. *Int. J. Climatol.* **27**: 1763–1774.

Huebener H, Kerschgens M. 2007b. Downscaling of current and future rainfall climatologies for southern Morocco. Part II: Climate change signals. *Int. J. Climatol.* **27**: 1065–1073.

Hupfer P, Kuttler W. 2006. *Witterung und Klima: Eine Einführung in die Meteorologie und Klimatologie.* B.G. Teubner Verlag / GWV Fachverlag GmbH, Wiesbaden: 554 pp.

Huth R. 1996. An intercomparison of computer-assisted circulation classification methods. *Int. J. Climatol*. **16**: 893–922.

Huth R. 2002. Statistical downscaling of daily temperature in Central Europe. *Journal of Climate* **15**: 1731–1742.

Huth R, Beck C, Philipp A, Demuzere M, Ustrnul Z, Cahynova M, Kysely J, Tveito OE 2008. Classifications of atmospheric circulation patterns, recent advances and applications. *Trends and Directions in Climate Research: Ann. N.Y. Acad. Sci.* **1146**: 105–152.

Huth R. 2010. Synoptic-climatological applicability of circulation classifications from the COST733 collection: First results. *Phys. Chem. Earth* **35**: 388–394.

IPCC 2007. *Climate Change 2007: The Physical Science Basis*. Contribution of Working Group I to the Fourth Assessment Report of the Intergovernmental Panel on Climate Change. Solomon S, Qin D, Manning M, Chen Z, Marquis M, Averyt KB, Tignor M, Miller HL (eds.) Cambridge University Press: Cambridge, UK and New York, USA: 996 pp.

Jacob D, Göttel H, Kotlarski S, Lorenz P, Sieck K. 2008. *Klimaauswirkungen und Anpassung in Deutschland Phase 1: Erstellung regionaler Klimaszenarien für Deutschland, Abschlussbericht zum UFOPLAN-Vorhaben 204 41 13*: 154 pp.

Jacob D, Podzun R. 1997. Sensitivity studies with the regional climate model REMO. *Meteorology and Atmospheric Physics* **63**: 119–129.

Jacob D, Van den Hurk BJJM, Andrae U, Elgered G, Fortelius C, Graham LP, Jackson SD, Karstens U, Koepken C, Lindau R, Podzun R, Rockel B, Rubel F, Sass BH, Smith R, Yang X. 2001. A comprehensive model intercomparison study investigating the water budget during the PIDCAP period. *Meteorol. and Atmos. Phys.* **77**: 19–43.

Jacob D. 2001. A note to the simulation of the annual and inter-annual variability of the water budget over the Baltic Sea drainage basin. *Meteorol. Atmos. Phys.* **77**: 61–73.

Jacobeit J. 2010. Classifications in climate research. *Phys. Chem. Earth* **35**: 411–421.

Jaeger EB, Anders I, Luethi D, Rockel B, Schaer C, Seneviratne SI. 2008. Analysis of ERA40-Driven CLM simulations for Europe. *Meteorologische Zeitschrift* **17**: 349–367.

Jendritzky G, Staiger H, Bucher K, Grätz A, Laschewski G. 2000. The perceived temperature. The method of the Deutscher Wetterdienst for the Assessment of Cold Stress and Heat Load for the Human Body. Internet Workshop on Windchill, 03.-07. April 2000, hosted by the Meteorological Service of Canada.

Jungclaus JH, Botzet M, Haak H, Keenlyside N, Latif M, Marotzke J, Mikolajewicz U, Roeckner E. 2006. Ocean circulation and tropical variability in the model ECHAM5/MPI-OM. *J. Climate* **19**: 3952–3972.

Kampmann B, Bröde P. 2009. Physiological responses to temperature and humidity compared with predictions of PHS and WBGT. In: Castellani JW, Endrusick TL (eds) *Environmental ergonomics XIII*. University of Wollongong, Wollongong: 54–58.

Kampmann B, Broede P, Fiala D. 2011. Physiological responses to temperature and humidity compared to the assessment by UTCI, WGBT and PHS. *Int. J. Biometeorol.*: DOI 10.1007/s00484-011-0410-0.

Kašpar M, Müller M. 2010. Variants of synoptic-scale patterns inducing heavy rains in the Czech Republic. *Phys. Chem. Earth* **35**: 477–483. doi: 10.1016/j.pce.2009.11.004.

Kassomenos PA, Katsoulis BD 2006. Mesoscale and macroscale aspects of the morning urban heat island around Athens, Greece. *Meteor. Atmos. Phys.* **94**: 209–218. doi:10.1007/s00703-006-0191-x.

Kastner-Klein P, Rotach MW. 2004. Mean flow and turbulence characteristics in an urban roughness sublayer. *Bound.-Layer Meteorology* **111**: 55–84.

Katzfey JJ, McGregor JL, Nguyen KC, Thatcher M. 2009. Dynamical downscaling techniques: Impacts on regional climate change signals. In: Anderssen RS, Braddock RD and Newham LTH (eds.) *MODSIM09 Int. Congress on Modelling and Simulation*: 2377-2383. URL: www.mssanz.org.au/modsim09/I13/katzfey_I13.pdf

Katzfey JJ. 2011. personal communications

Kawai T, Kanda M. 2010. Urban energy balance obtained from the comprehensive outdoor scale model experiment. Part I: Basic features of the surface energy balance. *J. Appl. Meteor. Climatol.* **49**: 1341-1359. doi: 10.1175/2010JAMC1992.1

Kessler E. 1969. *On the distribution and continuity of water substance in atmospheric circulation. Meteor. Monogr.* **32**, Amer. Meteor. Soc., Boston: 81 pp.

Kim Y-H, Baik J-J. 2002. Maximum urban heat island intensity in Seoul. *J. Appl. Meteorol.* **41**: 651–659.

Kim Y-H, Baik J-J. 2004. Daily maximum urban heat island intensity in large cities of Korea. *Theor. Appl. Climatol.* **79**: 151–164. doi: 10.1007/s00704-004-0070-7.

Knote C, Heinemann G, Rockel B. 2011. Changes in weather extremes: assessment of return values using high resolution climate simulations at convection-resolving scale. *Meteorol. Zeitschrift* **19**: 11–23. doi:10.1127/0941-2948/2010/0424.

Kostopoulou E, Jones PD. 2007. Comprehensive analysis of the climate variability in the eastern Mediterranean. Part I: Map-pattern classification. *Int. J. Climatol.* **27**: 1189–1214.

Kowalczyk E, Garratt JR, Krummel PB. 1994. Implementation of a soil-canopy scheme into the CSIRO GCM - regional aspects of the model response. *CSIRO Div. Atmospheric Research Tech Paper No. 32*: 59 pp.

Kreienkamp F, Baumgart S, Spekat A, Enke W. 2011. Climate signals on the regional scale derived with a statistical method: Relevance of the driving model's Resolution. *Atmosphere* **2**: 129–145. doi:10.3390/atmos2020129.

Kreienkamp F, Spekat A, Enke W. 2010. TransWeather Patterns—an extended outlook for the future climate. *EMS Annual Meeting Abstracts* **7**: 2010–453.

Krueger O, von Storch H. 2011. Evaluation of an air pressure–based proxy for storm activity. *J. Climate* **24**: 2612–2619, doi: http://dx.doi.org/10.1175/2011JCLI3913.1.

Kuttler W, Weber S, Schonnefeld J, Hesselschwerdt A. 2007. Urban/rural atmospheric water vapour pressure differences and urban moisture excess in Krefeld, Germany. *Int. J. Climatol.* **27**: 2005–2015.

Kyselý J, Huth R, Kim J. 2010. Evaluating heat-related mortality in Korea by objective classifications of 'air masses'. *Int. J. Climatol.* **30**: 1484–1501. doi: 10.1002/joc.1994

Kyselý J, Huth R. 2006. Changes in atmospheric circulation over Europe detected by objective and subjective methods. *Theor. Appl. Climatol.* **85**: 19–36.

Lacis A, Hansen J. 1974. A parameterization of the absorption of solar radiation in the Earth's atmosphere. *J. Atmos. Sci*. **31**: 118–133.

Lengfeld K, Ament F. 2012. Observing local-scale variability of near-surface temperature and humidity using a wireless sensor network. *J. Appl. Meteor. Climatol.* **51**: 30–41, doi: http://dx.doi.org/10.1175/JAMC-D-11-025.1.

Lengfeld K. 2012. *Assessing near surface variability with a wireless sensor network on the small scale*. Ph.D. thesis, Department Geowissenschaften, Universität Hamburg: 131 pp.

Liu W, You H, Dou J. 2009. Urban-rural humidity and temperature differences in the Beijing area. *Theoretical and Applied Climatology* **96**: 201–207.

Lupikasza E. 2010. Relationships between occurrence of high precipitation and atmospheric circulation in Poland using different classifications of circulation types. *Phys. Chem. Earth* **35**: 448–455.

Lüpkes C, Schlünzen KH. 1996. Modelling the Arctic convective boundary-layer with different turbulence parameterizations. *Bound.-Layer Meteorol.* **79**: 107–130.

Lüpkes C, Vihma T, Birnbaum G, Wacker U. 2008. Influence of leads in sea ice on the temperature of the atmospheric boundary layer during polar night. *Geophysical Research Letters* **35**: L03805.

Majewski D. 1991. The Europa-Modell of the Deutscher Wetterdienst. *Vol. 2 of ECMWF seminar on numerical methods in atmospheric models*. 147–191.

Maraun D, Wetterhall F, Ireson AM, Chandler RE, Kendon EJ, Widmann M, Brienen S, Rust HW, Sauter T, Themessl M, Venema VKC, Chun KP, Goodess CM, Jones RG, Onof C, Vrac M, Thiele-Eich I. 2010. Precipitation downscaling under climate change: recent developments to bridge the gap between dynamical models and the end user. *Reviews of Geophysics* **48**: 34 pp. DOI: 10.1029/2009RG000314.

Martens M. 2012. *Untersuchung des Klimas der Norddeutschen Tiefebene mittels Datenanalyse und Downscalings*. Diploma thesis, Meteorologisches Institut Department Geowissenschaften Universität Hamburg

Martilli A, Clappier A, Rotach MW. 2002. An urban surface exchange parameterisation for mesoscale models. *Bound.-Layer Meteorol.* **104**: 261–304.

Masson V. 2000.A physically-based scheme for the urban energy budget in atmospheric models. *Bound.-Layer Meteorol.* **94**: 357–397.

Mayer H, Matzarakis A, Iziomon MG. 2003: Spatio-temporal variability of moisture conditions within the Urban Canopy Layer. *Theor. Appl. Climatol.* **76**: 165–179

McGregor JL, Dix MR. 2008. An updated description of the Conformal-Cubic Atmospheric Model. *High Resolution Simulation of the Atmosphere and Ocean*, eds. K. Hamilton and W. Ohfuchi, Springer: 51–76.

McGregor JL. 2003. A new convection scheme using a simple closure. In: "Current issues in the parameterization of convection", *BMRC Research Report 9*3: 33–36.

McGregor JL. 2005. C-CAM: Geometric aspects and dynamical formulation. *CSIRO Atmospheric Research Tech. Paper No. 70*: 43 pp. [electronic publication]

Mesinger F, Arakawa A. 1976. *Numerical methods used in atmospheric models.* Garp Publications Series No. 17, Volume I: 64 pp.

Mihalakakou G, Flocas HA, Santamouris M, Helmis CG. 2002. Application of neural networks to the simulation of the heat island over Athens, Greece, using synoptic types as a predictor. *J. Appl. Meteor.* **41**: 519–527. doi: http://dx.doi.org/10.1175/1520-0450(2002)041<0519:AONNTT>2.0.CO;2

Moreno-Garcia MC. 1994. Intensity and form of the urban heat island in Barcelona. *Int. J. Climatol.* **14**: 705–710.

Morris CJG, Simmonds I. 2000. Associations between varying magnitudes of the urban heat island and the synoptic climatology in Melbourne, Australia. *Int. J. Climatol.* **20**: 1931–1954.

Morris CJG, Simmonds I, Plummer N. 2001. Quantification of the influences of wind and cloud on the nocturnal urban heat island of a large city. *J. Appl. Met.* **40**: 169–182.

Murphy AH, Brown BG, ChenY-S. 1989. Diagnostic verification of temperature forecasts. *Wea. Forecasting* **4:** 485–501.

Muthers S, Matzarakis A, Koch E. 2010. Climate change and mortality in Vienna-A human biometeorological analysis based on regional climate modeling. *Int. J. Environ. Res. Public Health* **7**: 2965-2977.

Najac J, Lac C, Terray L. 2011. Impact of climate change on surface winds in France using a statistical-dynamical downscaling method with mesoscale modelling. *Int. J. Climatol.* **31**: 415–430. doi: 10.1002/joc.2075

Nakicenovic N, Alcamo J, Davis G, de Vries B, Fenhann J, Gaffin S, Gregory K, Grubler A, Jung TY, Kram T, La Rovere EL, Michaelis L, Mori S, Morita T, Pepper W, Pitcher H, Price L, Riahi K, Roehrl A, Rogner H-H, Sankovski A, Schlesinger M, Shukla P, Smith S, Swart R, van Rooijen S, Victor N, Dadi Z. 2000. *Special Report on Emissions Scenarios* Cambridge, 599 pp.

Nappo CJ, Chun H-Y, Lee H-J. 2004. A parametrization of wave stress in the planetary boundary layer for use in mesoscale models. *Atm. Env*. **38**, 2665–2675.

Niemeier U, Schlünzen KH. 1993. Modelling steep terrain influences on flow patterns at the Isle of Helgoland. *Beitr. Phys. Atmosph.* 66: 45–62.

Oke TR. 1973. City size and the urban heat island. *Atm. Environ.* **7**: 769–779.

Oke TR. 1987. *Boundary layer climates*. 2nd Edition. Routledge, Taylor and Francis Group, Cambridge, 435 pp.

Orlowsky B, Gerstengarbe FW, Werner PC. 2008. A resampling scheme for regional climate simulations and its performance compared to a dynamical RCM. *Theoretical and Applied Climatology* **92**: 209–223.

Pennell C, Reichler T. 2011. On the effective number of climate models. *J. Climate* **24**: 2358–2367.

Philipp A, Bartholy J, Beck C, Erpicum M, Esteban P, Fettweis X, Huth R, James P, Jourdain S, Kreienkamp F, Krennert T, Lykoudis S, Michalides SC, Pianko-Kluczynska K, Post P, Álvarez DR, Schiemann R, Spekat A, Tymvios FS. 2010. Cost733cat – A database of weather and circulation type classification. *Phys. Chem. Earth* **35**: 360–373.

Philipp A, Jacobait J. Fereday DR, Jones PD, Moberg A, Wanner H. 2007. Long-termvariability of daily North Atlantic–European pressure patterns since 1850 classified by simulated annealing clustering. *J. Clim.* **20**: 4065–4095.

Piani C, Haerter JO, Coppola E. 2010. Statistical bias correction for daily precipitation in regional climate models over Europe. *Theor. Appl. Climatol.* **99**: 187–192.

Pinto JG, Neuhaus CP, Leckebusch GC, Reyers M, Kerschgens M. 2010. Estimation of wind storm impacts over West Germany under future climate conditions using a statistical-dynamical downscaling approach. *Tellus A* **62**: 188–201. doi: 10.1111/j.1600-0870.2009.00424.x

Ray S, Turi RH. 2000. Determination of the number of clusters in K-means clustering and application in colour image segmentation. *Proceedings of the 4th International Conference on Advances in Pattern Recognition and Digital Technique, New Delhi, Narosa*: 137–143

Reidat R. 1971. Temperatur, Niederschlag, Staub. *Deutscher Planungsatlas. Band VIII. Hamburg, Lieferung 7.* Gebrüder Jänecke, Hannover

Renner E, Münzenberg A. 2003. Impact of biogenic terpene emissions from Brassica napus on tropospheric ozone over Saxony (Germany) – Numerical investigation. *Environmental Science and Pollution Research* **10**: 147–153. DOI: 10.1065/espr2003.05.154.

Reusch DB. 2010. Nonlinear climatology and paleoclimatology: capturing patterns of variability and change with self-organizing maps. *Phys. Chem. Earth* **35:** 329–340.

Reynolds RW, Rayner NA, Smith TM, Stokes DC, Wang W. 2002. An improved in situ and satellite SST analysis for climate. *J. Climate* **15**: 1609–1625.

Reynolds RW. 1988. A real-time global sea surface temperature analysis. *J. Climate* **1**: 75–86.

Ries H, Schlünzen K, Brümmer B, Claussen M, Müller G. 2010. Impact of surface parameter uncertainties on the development of a trough in the Fram Strait region. *Tellus* **62A**: 377–392. doi:10.3402/tellusa.v62i4.15704.

Ries H, Schlünzen KH. 2009. Evaluation of a mesoscale model with different surface parameterizations and vertical resolutions for the bay of Valencia. *Monthly Weather Review* **137**: 2646–2661, DOI: 10.1175%2F2009MWR2836.1.

Roeckner E, Arpe K, Bengtsson L. Christoph M, Claussen M, Dümenil L, Esch M, Giorgetta M, Schlese U, Schulzweida U. 1996. *The atmospheric general circulation model ECHAM 4: Model description and simulations of the present day climate. Report 218*. Max-Planck-Institute for Meteorology, Hamburg: 90 pp.

Roeckner E, Bäuml G, Bonaventura L, Brokopf R, Esch M, Giorgetta M, Hagemann S, Kirchner I, Kornblueh L, Manzini E, Rhodin A, Schlese U, Schulzweida, U, Tompkins A. 2003. *The atmospheric general circulation model ECHAM 5. PART I: Model description*. Max-Planck-Institute for Meteorology, Hamburg: 127 pp.

Rosenzweig C, Solecki WD, Parshall L, Chopping M, Pope G, Goldberg R. 2005. Characterizing the urban heat island in current and future climates in New Jersey. *Environmental Hazards* **6**: 51–62.

Rotstayn LD. 1997. A physically based scheme for the treatment of stratiform clouds and precipitation in large-scale models. I: Description and evaluation of the microphysical processes. *Q. J. R. Meteorol. Soc.* **123**: 1227–1282.

Rummukainen M. 2010. State-of-the-art with regional climate models. *WIREs Clim. Change* **1**: 82–96. doi: 10.1002/wcc.8

Sakakibara Y, Matsui E. 2005. Relation between heat island intensity and city size indices/urban canopy characteristics in Settlements of Nagano Basin, Japan. *Geographical Review of Japan* **78**: 812–824.

Salameh T, Drobinski P, Vrac M, Naveau P. 2009. Statistical downscaling of near-surface wind over complex terrain in southern France. *Meteorol. Atmos. Phys.* **103**: 243–256.

Sandoval S, Ament F, Eschenbach A. 2010. Hamburg Urban Soil Climate Observatory (HUSCO): A concept to assess the impact of moisture and energy fluxes of urban soils on local climate. *Geophysical Research Abstracts*, Vol. 12, EGU2010-4265, EGU General Assembly 2010.

Sauter T, Venema V. 2011. Natural three-dimensional predictor domains for statistical precipitation downscaling. *J. Climate* **24**: 6132–6145. doi: http://dx.doi.org/10.1175/2011JCLI4155.1

Schlünzen KH, Bungert U, Flagg DD, Fock BH, Gierisch A, Grawe D, Kirschner P, Lüpkes C, Reinhardt V, Ries H, Schoetter R, Spensberger C, Uphoff M. 2012b. Technical documentation of the Multiscale Model System M-SYS (METRAS, MITRAS, MECTM, MICTM, MESIM). *MEMI Technical Report 3*: 138 pp.

Schlünzen KH, Conradi C, Haller M. 2012c. Ergebnisbandbreiten mesoskaliger atmosphärischer Modelle. in A. Raabe (Hrsg.). 2012: *METTOOLSVIII – Tagungsbeiträge 20.03.2012 – 22.03.2012. Wissenschaftliche Mitteilungen aus dem Institut für Meteorologie der Universität Leipzig* **49**, Selbstverlag: 1. ISBN 978-3-9811114-9-1

Schlünzen KH, Flagg DD, Fock BH, Gierisch A, Lüpkes C, Reinhardt V, Spensberger C. 2012a. Scientific documentation of the Multiscale Model System M-SYS (METRAS, MITRAS, MECTM, MICTM, MESIM). *MEMI Technical Report 4*: 138 pp.

Schlünzen KH, Grawe D, Bohnenstengel SI, Schlüter I, Koppmann R. 2011. Joint modelling of obstacle induced and mesoscale changes – current limits and challenges. *J Wind Eng. Ind. Aerodynamics* **99**: 217–255. doi:10.1016/j.jweia.2011.01.009.

Schlünzen KH, Hoffmann P, Rosenhagen G, Riecke W. 2010. Long-term changes and regional differences in temperature and precipitation in the metropolitan area of Hamburg. *Int. J. Climatol.* **30**: 1121–1136. doi: 10.1002/joc.1968.

Schlünzen KH, Katzfey JJ. 2003. Relevance of sub-grid-scale land-use effects for mesoscale models. *Tellus* **55A**: 232–246.

Schlünzen KH, Meyer EMI. 2007. Impacts of meteorological situations and chemical reactions on daily dry deposition of nitrogen into the Southern North Sea. *Atmospheric Environment* **41**: 289–302.

Schlünzen KH. 1990. On the inland penetration of sea breeze fronts. *Beitr. Phys. Atmosph.* **63**: 243–256.

Schlünzen KH. 1992. Modellierung des Strömungsfeldes über Norddeutschland für den 23.Mai 1989. *Ann. Meteor. NF* **27**: 308–309.

Schlünzen KH. 2012. Detail of information needed to simulate urban climate. *MEMI Technical Report 5* in preparation.

Schlünzen KH, Sokhi RS. 2008. Overview of tools and methods for meteorological and air pollution mesocale model evaluation and user training. *GAW Report No. 181*, WMO/TD-No. 1457: 116 pp.

Schoetter R, Hoffmann P, Rechid D, Schlünzen KH. 2012. Evaluation and bias correction of regional climate model results using model evaluation measures. *J. Appl. Meteor. Climatol.* accepted.

Schoetter R, Grawe D, Hoffmann P, Krischner P, Grätz A, Schlünzen KH. 2012. Can local adaptation measures compensate for regional climate change with respect to perceived temperature? submitted to *Meteorol. Z.*

Schueler S, Schlünzen KH. 2006. Modeling of oak pollen dispersal on the landscape level with a mesoscale atmospheric model. *Environ Model Assess* **11**: 179–194. doi: 10.1007/s10666-006-9044-8.

Schwarzkopf MD, Fels SB. 1991. The simplified exchange method revisited: An accurate, rapid method for computation of infrared cooling rates and fluxes. *J. Geophys. Res.* **96**: 9075–9096.

Semmler T, Jacob D, Schlünzen KH, Podzun R. 2005. The water and ernergy budget of the Arctic atmosphere. *J. Climate* **18**: 2515–2530.

Shen J, Chang SI, Lee ES, Deng Y, Brown SJ. 2005. Determination of cluster number in clustering microarray data. *Appl. Math. Comput.* **169**: 1172–1185.

Sheng L, Schlünzen KH, Wu Z. 2000. Three-dimensional numerical simulation of the mesoscale wind structure over Shandong peninsula. *Acta Meteorol. Sinica* **1**: 9–107.

Shepherd JM. 2005. A review of current investigations of urban-induced rainfall and recommendations for the future. *Earth Interactions* **9**: [Online available http://EarthInteractions.org]

Sheridan SC, Lee CC. 2010. Synoptic climatology and the general circulation model. *Prog. Phys. Geog.* **34**: 101–109.

Smith R. 1990. A scheme for predicting layer clouds and their water content in a general circulation model. *Q. J. R. Meteorol. Soc.* **116**: 435–460.

Spekat A, Enke W, Kreienkamp F. 2007. Neuentwicklung von regional hoch aufgelösten Wetterlagen für Deutschland und Bereitstellung regionaler Klimaszenarios auf der Basis von globalen Klimasimulationen mit dem Regionalisierungsmodell WETTREG auf der Basis von globalen Klimasimulationen mit ECHAM5/MPIOM T63L31 2010 bis 2100 für die Szenarios B1, A1B und A2. Forschungsprojekt im Auftrag des Umweltbundesamtes, FuEVorhaben Förderkennzeichen 204 41 138.

Spekat A, Kreienkamp F, Enke W. 2010. An impact-oriented classification method for atmospheric patterns. *Physics and Chemistry of the Earth* **35:** 352–359.

Staiger H, Laschewski G, Grätz A. 2011. The Perceived Temperature – A versatile index for the assessment of the human thermal environment. Scientific Basics. *Int. J. Biometeorol., Part A*: doi:10.1007/S00484-011-0409-6.

Steeneveld GJ, Koopmans S, Heusinkveld BG, van Hove LWA, Holtslag AAM. 2011. Quantifying urban heat island effects and human comfort for cities of variable size and urban morphology in the Netherlands, *J. Geophys. Res.* **116**: D20129, doi:10.1029/2011JD015988.

Stephenson, DB, Hannachi A, O'Neill A. 2004. On the existence of multiple climate regimes. *Q. J. R. Meteorol. Soc.* **130**: 583–605.

Steppeler J, Doms G, Schättler U, Bitzer HW, Gassmann A, Damrath U, Gregoric G. 2003. Meso-gamma scale forecasts using the nonhydrostatic model LM. *Meteorol. Atmos. Phys.* **82**: 75–96.

Stewart I. 2011. A systematic review and scientific critique of methodology in modern urban heat island literature. *Int. J. Climatol.* **31**: 200–217.

Thatcher M, McGregor JL. 2009. Using a scale-selective filter for dynamical downscaling with the conformal cubic atmospheric model. *Mon. Wea. Rev.* **137**: 1742–1752.

Thompson HL. 2008. Modelling the impact of urbanisation on the region of the Greater London Area. PhD thesis, School of Geography, The University of Birmingham, Birmingham, UK: 263 pp.

Tumanov S, Stan-Sion A, Lupu A, Soci C, Oprea C. 1999. Influences of the city of Bucharest on weather and climate parameters. *Atmospheric Environment* **33**: 4173–4183.

Uppala SM, Kallberg PW, Simmons AJ, Andrae U, Bechtold VD, Fiorino M, Gibson JK, Haseler J, Hernandez A, Kelly GA, Li X, Onogi K, Saarinen S, Sokka N, Allan RP, Andersson E, Arpe K, Balmaseda MA, Beljaars ACM, Van De Berg L, Bidlot J, Bormann N, Caires S, Chevallier F, Dethof A, Dragosavac M, Fisher M, Fuentes M, Hagemann S, Holm E, Hoskins BJ, Isaksen L, Janssen PAEM, Jenne R, McNally AP, Mahfouf JF, Morcrette JJ, Rayner NA, Saunders RW, Simon P, Sterl A, Trenberth KE, Untch A, Vasiljevic D, Viterbo P, Woollen J. 2005. The ERA 40 re-analysis. *Quarterly Journal of the Royal Meteorological Society* **131**: 2961–3012.

van der Kamp D, Curry CL, Monahan AH. 2011. Statistical downscaling of historical monthly mean winds over a coastal region of complex terrain. II. Predicting wind components. *Climate Dynamics* **38**: 1301-1311. DOI: 10.1007/s00382-011-1175-1.

van der Linden P, Mitchell JFB (Hrsg.). 2009. *ENSEMBLES Climate change and its impacts at seasonal, decadal and centennial timescales, Summary of research and results from the ENSEMBLES project.* Met Office Hadley Centre, FitzRoy Road, Exeter EX1 3PB, UK

von Salzen K, Claussen M, Schlünzen KH. 1996. Application of the concept of blending height to the calculation of surface fluxes in a mesoscale model. *Meteorol. Zeitschrift, N.F.* **5**: 60–66.

von Storch H, Langenberg H, Feser F. 2000. A spectral nudging technique for dynamical downscaling purposes. *Mon. Wea. Rev.* **128**: 3664–3673.

Waldron KM, Paegle J, Horel JD. 1996. Sensitivity of a spectrally filtered and nudged limited area model to outer model options. *Mon. Wea. Rev.* **124**: 529–547.

Walter A, Keuler K, Jacob D, Knoche R, Block A, Kotlarski S, Müller-Westermeier G, Rechid D, Ahrens W. 2006. A high resolution reference data set of German wind velocity 1951-2001 and comparison with regional climate model results. *Meteorologische Zeitschrift* **15**: 585–596.

Wilby RL, Dawson CW, Barrow EM. 2002. SDM-a decision support tool for the assessment of regional climate impacts. *Environmental Modelling & Software* **17**: 147–159.

Wilby RL. 2003. Past and projected trends in London's urban heat island. *Weather* **58**: 251–260.

Wilby RL. 2008. Constructing climate change scenarios of urban heat island intensity and air quality. *Environment and Planning B: Planning and Design* **35**: 902–919.

Wilby RL, Jones PD, Lister DH. 2011. Decadal variations in the nocturnal heat island of London. *Weather* **66**:DOI: 10.1002/wea.679.

Wilby RL, Troni J, Biot Y, Tedd L, Hewitson BC, Smith DG, Sutton RT. 2009. A review of climate risk information for adaptation and development planning. *Int. J. Climatol.* **29**: 1193–1215.

Wilby RL, Wigley TML.1997. Downscaling general circulation model output: a review of methods and limitations. *Progr. Phys. Geogr.* **21**: 530–548

Wilks D. 1999. Interannual variability and extrem-value characterisitcs of several stochastic daily precipitation models. *Water. Resour. Res.* **34**: 2995–3008.

Wu J-B, Chow K-C, Fung JCH, Lau AKH,Yao T. 2011. Urban heat island effects of the Pearl River Delta city clusters—their interactions and seasonal variation. *Theor. Appl. Climatol.* **103**: 489–499

Wu Z, Schlünzen KH. 1992. Numerical study on the local wind structures forced by the complex terrain of Qingdao area. *Acta Meteorol. Sinica* **6**: 355–366.

Yow DM. 2007. Urban heat islands: Observations, impacts, and adaptation. *Geography Compass* **1/6:** 1227–1251.

Zhou Y, Shepherd JM. 2009. Atlanta's urban heat island under extreme heat conditions and potential mitigation strategies. *Nat. Hazards* **52**: 639–668.

Zilitinkevich SS, Elperin T, Kleeorin N, Rogachevskii I. 2007. Energyand flux-budget (EFB) turbulence closure model for stably stratified flows. Part I: Steady-state, homogeneous regimes. *Bound.-Layer Meteorol.* **125**: 167–191.

Zilitinkevich SS. 2002. Third-order transport due to internal waves and non-local turbulence in the stably stratified surface layer. *Q. J. R. Meteorol. Soc.* **128**: 913–925.